On Nighttime Turbulent Exchange within and above a Sloped Vineyard

by

Kelsey Everard

B.S., University of Virginia, 2015

A THESIS SUBMITTED IN PARTIAL FULFILLMENT OF
THE REQUIREMENTS FOR THE DEGREE OF

MASTER OF SCIENCE
in
THE FACULTY OF GRADUATE AND POSTDOCTORAL STUDIES
(Geography)

THE UNIVERSITY OF BRITISH COLUMBIA
(Vancouver)

August 2017

Abstract

High frequency three-dimensional wind and distributed temperature measurements were taken over a $\sim 7^{\circ}$ vineyard slope in the Southern Okanagan Valley, British Columbia, Canada, during three weeks in July 2016. Approximately 17% of the nighttime is characterised by drainage flow along the local slope. Drainage conditions are characterised by inverted temperatures beginning around $z/h_c = 0.39$, where z is the height above ground level (AGL) and h_c is the canopy height ($\sim$ 2.3 m AGL), and near-surface lapses. A jet maximum is observed around $z/h_c = 1.65$, while a weak inflection point is observed near the canopy top, suggesting influence from both drainage layer and canopy layer dynamics on the turbulent field. The greatest observed fluxes in both the stream-wise momentum flux and the sensible heat flux are near the top of the canopy, consistent with the location of the inflection point. Calculated two-point length scales from distributed temperature measurements reveal that turbulent structures are smallest near the canopy top. Conditional sampling of the 3-D ultrasonic wind components and acoustic temperature indicate that a large fraction of canopy layer transport is driven by canopy-top turbulence, with sweeps dominating over ejections, particularly at $z/h_c = 0.65$. Results presented here are important both for nighttime vineyard management techniques and for further understanding on particle dispersion.

Lay Summary

In the following work, the exchange of heat and momentum within a vineyard environment during the nighttime is investigated. It is shown that two regimes dictate the turbulent dynamics of the system, both the nighttime drainage regime and the canopy layer regime. This work furthers current understanding on the interface and communication between the surface and the atmosphere, and is integral to the continued efforts to improve the representation of near-surface processes in current and future climate and weather models.

Preface

Field site set-up was conducted by myself, Dr. Andreas Christen (hereafter referred to as AC), Dr. Andy Black, and Paul Skaloud (hereafter referred to as PS). Soil moisture measurements were made and recorded by PS during the campaign. Scripting of the logger programs was completed in part by my supervisor, AC. All data processing was scripted and completed by myself. Part of the introduction section of this thesis was completed as part of a required course for all first year graduate students in the Department of Geography (GEOB 500). Sonic inter-comparison data was acquired from Liss et al. (2009).

Table of Contents

List of Tables

List of Figures

Symbol	Units	Description
$\overline{a}$		Five-minute mean of a
$\langle a \rangle$		Ensemble average of a in time (i.e., average of multiple five-minute averaged a)
$\{a\}$		Ensemble average of a in space
a'		Deviation of instantaneous a from $\overline{a}$
a		Dummy variable for definitions
b		Dummy variable for definitions
dz	m	change in height above ground level
h_b	m	Height of the bottom of the canopy crown-space
h_c	m	Height of the canopy
h_i	m	Height of velocity inflection point
H		Quadrant analysis hole size
k	W m^{-1} K^{-1}	Soil thermal conductivity
L_c	m	Obukhov length at the canopy top, h_c
MAE		Mean Absolute Error
N^2	s^{-2}	Brunt Väisälä frequency
Q^*	W m^{-2}	Net Radiation
R_i		Gradient Richardson number
R_f		Flux Richardson number
Sk_a	units of a	Skewness in a
T	$^\circ$ C	Air temperature (acoustic and/or fine-wire)
T_s	$^\circ$ C	Soil temperature
TKE	m^2 s^{-2}	Turbulent kinetic energy
u	m s^{-1}	Stream-wise wind velocity
u_c	m s^{-1}	Stream-wise wind velocity at h_c
uc	m s^{-1}	Convection velocity
U_a	units of a	Measurement uncertainty
v	m s^{-1}	Cross-stream wind velocity
w	m s^{-1}	Slope-normal wind velocity

WD	$^\circ$	Wind direction
x	m	Along-slope distance
y	m	Cross-slope distance
z	m	Height above ground level
α	$^\circ$	Slope angle
δ	$^\circ$	Difference between above-canopy wind vector and orientation of vineyard rows
Θ	K	Potential (air) temperature

Acronym	**Units**	**Description**
AGL	m	Above Ground Level
AM25T		Campbell Scientific Multiplexer
BOV		Burrowing Owl Vineyards
CSAT-3D		Campbell Scientific 3D sonic anemometer
CSL		Canopy sub-layer
DS		Drainage wind cluster
IRT		Infrared temperature sensor
LST		Local Standard Time
RSL		Roughness sub-layer
TC		Thermocouple (fine wire, unless otherwise stated)
VOF		Valley flow or otherwise cluster
VWC	%	Volumetric (soil) Water Content

Acknowledgements

I would like to acknowledge first and foremost, my advisor Dr. Andreas Christen, who was supportive and enthusiastic of my research during the program, and without whom my research would not have been possible. Management at the Burrowing Owl Estate Winery, who granted us free access to the study site and accommodation during the campaign. Dr. Andy Black, who lent a Campbell Scientific CSAT-3D sonic anemometer to us during the campaign. Dr. Holly Oldyroyd and Dr. Marco Giometto, who have continually acted as mentors to me. Dr. Dan Moore, who has provided aid with data analysis in R. Dr. Rob Stoll who has provided invaluable information on observed canopy sub-layer dynamics in other vineyards. Dr. Andy Sturman who found the best slope for the field measurements, and was an invaluable help in initial set-up. My committee members, Dr. Ian McKendry and Dr. Phil Austin, who took the time to edit and respond to my thesis draft. Paul Skaloud, the superior undergraduate field assistant, without whom my campaign would have been near impossible. Jose Aparicio, who kindly helped me navigate ArcMap. Zoran Nesic, who was of vital help during instrumentation tests. Finally, my parents, who were a constant emotional support throughout the process.

This research was funded by several grants and awards. Selected equipment was supported by the Canada Foundation for Innovation (Grant 33600, Christen) and NSERC RTI (Christen). Financial support through scholarships and training were provided by UBC Faculty of Graduate and Postdoctoral Studies and UBC Geography. Funding for undergraduate field assistance was provided via a Work Learn International Undergraduate Research Award. Funding for the purchase of thermocouple materials and travel expenses was provided in part by UBC Faculty of Arts via a Graduate Student Research Award.

This work is dedicated to my dad, who sparked my interest in buoyancy and encouraged me to pursue science; and to my mom, who challenged my knowledge by asking incredibly in depth questions about my research and its relevance.

1 Introduction

For decades, researchers have sought to characterise the turbulent transfer of momentum and scalars within and above canopies. The presence of vegetation influences both the mechanical and thermal aspects of the flow, including the behaviour of drag near the surface (e.g. Garrett, 1983; Gross, 1987; Yi et al., 2005; Oldroyd et al., 2014) and radiative cooling, heat storage, and sensible heat transfer (e.g. Froelich and Schmid, 2006; Froelich et al., 2011). While a substantial amount of work has elucidated the mean and turbulent nature of flow within and above dense, homogeneous canopies over flat terrain and under near-neutral stability (e.g. Finnigan, 2000; Finnigan et al., 2009), understanding is far from complete for the more complex cases typical of the Earth's surface. For agricultural crops, knowledge on the turbulent field reveals the potential for particle dispersion (e.g. Bailey et al., 2014; Miller et al., 2015), which can include spread of disease, insecticides, and pesticides. In a vineyard, the impact of the canopy on particle dispersion becomes further complicated by the canopy organisation (Miller et al., 2015).

For the present case, a complex situation arises as a row-oriented vineyard canopy interacts with a nighttime drainage flow. The following introduction includes a section on the canopy sub-layer (CSL), a section on drainage flow, and a final section discussing the objectives of the thesis.

1.1 Canopy Layer Dynamics

The roughness sub-layer, normally defined as the layer between the ground surface and at least twice the height of the canopy (e.g. Finnigan, 2000; Katul et al., 2013), is the layer in which the presence of the canopy influences the mean and turbulent nature of the flow. The RSL contains the canopy sub-layer (CSL), which is defined as the layer between the ground surface and the height of the canopy, and is the region where the environment is dictated by the micro-scale properties of the various surfaces present within the domain (e.g. Oke et al., 2017). Canopy height is usually defined as either the physical height AGL of the canopy, h_c (e.g. Thomas and Foken, 2007*a*; Katul et al., 2013), or as the height of the velocity inflection point, h_i (e.g. Raupach et al., 1996), which is near h_c. Extensive work has allowed for the description of the mean and turbulent nature of flow at near-neutral stability within the CSL for a variety of homogeneous canopies (*i.e.*, more-or-less horizontally homogeneous at the canopy height), such as a tall forest canopy (e.g. Cava et al., 2006; Launiainen et al., 2007) or an agricultural crop, like corn or wheat (e.g. Paw U et al., 1992). While our understanding of the 'simple' CSL dynamics are strong, our understanding of more complex CSL situations is far from complete. Even when more complex situations are considered, the canopies investigated are typically tall forest canopies (e.g. Launiainen et al., 2007), due to current efforts to address carbon balance

closure issues at long-term flux measurement sites (e.g. Aubinet et al., 2003; Heinesch et al., 2007; Belcher et al., 2008). In the following sub-section, typical CSL dynamics under near neutral stability are summarised, recent advances in CSL studies are discussed, and the various observational and analysis techniques employed in CSL studies are briefly reviewed.

1.1.1 Canopy Turbulence in Near Neutral Conditions

It is well known that under near-neutral stability, for fairly horizontally homogeneous canopies, the canopy-top dynamics behave similarly to the plane-mixing layer dynamics, whereby the hydrodynamic instability induced by an inflection in the velocity profile generates large turbulent structures near the canopy top (Raupach et al., 1996; Finnigan, 2000; Finnigan et al., 2009; Bailey and Stoll, 2016). While the turbulent field is known to be three dimensional, the coherent structures generated via the shear instability have been shown to be quasi two-dimensional (Bailey and Stoll, 2016). These structures scale well with canopy height (e.g. Finnigan, 2000) and are responsible for a large fraction of the total turbulent flux within the canopy (e.g. Thomas and Foken, 2007*a*). The predominance of larger, non-locally generated coherent structures controlling the flux within the canopy then invalidates the applicability of simple flux-gradient transport theory (K-theory, see Stull (1988) for details) (Cellier and Brunet, 1992; Raupach et al., 1996; Katul et al., 2013), necessitating either canopy-relevant corrections to K-theory (Cellier and Brunet, 1992) and/or higher-order closure (e.g. Wilson and Shaw, 1977). The speed at which the structures propagate through the flow is thought to be determined by the mean wind speed at the height of the core of the structure (Bailey and Stoll, 2016). For an in depth consideration of the behaviour of coherent structures within homogeneous, dense canopies under near-neutral stability, see Bailey and Stoll (2016).

Conditional sampling of the Reynolds stress (see Section 1.1.2 and 2.6 for details) in the CSL reveals fairly exuberant flow, with sweeps - the movement of above canopy air (*i.e.* typically higher momentum, colder, fluid) downwards into the canopy - dominating over ejections in the canopy environment (e.g. Raupach, 1981; Finnigan, 2000; Finnigan et al., 2009). Above the roughness sub-layer, the sweep/ejection ratio returns to unity as is expected for classical rough-wall boundary layer flow (e.g. Raupach, 1981; Bailey and Stoll, 2013), acting as an indication of the depth of the CSL.

1.1.2 Advances in CSL Understanding

Many authors have worked to extend known turbulent dynamics for the simple near-neutral case to those with further complexities, like varying stability (Leclerc et al., 1990; Launiainen et al., 2007; Thomas and Foken, 2007*a*; Dupont and Patton, 2012; Francone et al., 2012), varying canopy density (Poggi et al., 2004),

in regions of hilly terrain (e.g. Finnigan and Belcher, 2004; Francone et al., 2012), near canopy discontinuities, like forest edges (e.g. Irvine et al., 1997; Gash, 1986), and in canopies with specific orientations like the classical row-gap trellised vineyard environment investigated in the present study (Francone et al., 2012; Chahine et al., 2014; Miller et al., 2017).

Increased stability has been found to decrease shear length scales (Dupont and Patton, 2012; Miller et al., 2017), however, has no effect over the characteristic sweep/ejection cycle observed under near-neutral conditions (Miller et al., 2017). With stability comes the increased potential for wave motions, and wave breaking (e.g. Lee and Mahrt, 2005), which could introduce scales potentially on the order of coherent structures thus affecting measurements and analysis. Additionally, under stable conditions over slopes, the development of a drainage wind can occur (e.g. Lee and Mahrt, 2005), which further complicates the flux-gradient relationship (and corrections to it due to vegetation), among other things like advection (e.g. Aubinet et al., 2003; Aubinet, 2008; Belcher et al., 2008; Thomas, 2011) and the coupling between the canopy and the outer-canopy environment (for tall forest canopies) (e.g. Turnipseed et al., 2003; Froelich and Schmid, 2006; Sun et al., 2006; Rebman et al., 2010).

As for canopy density, there are two extremes under consideration, 1) the very dense case in which the mixing-layer analogy is expected to hold (e.g. Finnigan, 2000), and 2) the completely bare case in which rough-wall boundary layer theory is expected to hold. Using a canopy model in a flume, Poggi et al. (2004) describe the turbulent nature within a sparser canopy as a three-layered system, whereby deep-canopy turbulence is dominated by von-Kármán streets, the canopy-top region is influenced by both mixed-layer and boundary layer dynamics, and the above-canopy environment returns to the classical boundary-layer dynamics.

Dispersive flux, or transfer due to dispersion from high to low concentration, within the canopy is related to canopy density, whereby dispersive fluxes are largest for sparser canopies (Poggi and Katul, 2008). Böhm et al. (2013) show that the heterogeneity and geometry of the canopy can also affect whether or not there are general wake and/or non-wake regions, which can then add an additional spatial heterogeneity to the behaviour of turbulence within the canopy. Miller et al. (2017) show that for a row-gap aligned canopy, the direction of the above-canopy wind also affects whether or not the canopy behaves more like a dense canopy (*i.e.*, row-perpendicular wind vectors) or a sparse, open canopy (*i.e.*, row-parallel wind vectors). In either case, flow channelling by the canopy is present, making the direction of the approaching above-canopy wind in relation to the direction of row-orientation an important influence on the CSL turbulence (Miller et al., 2017). Miller et al. (2017) investigate this directional dependence in depth, revealing a further influence of

stability in the amount of wind-vector turning due to a trellised vineyard canopy, with the influence of the canopy-orientation extending higher into the atmosphere under moderately stable conditions compared with near-neutral conditions. The added turning of wind vectors then increases shear, depending on the wind direction. For example, when the above-canopy wind is angled more obliquely to the canopy-rows, the shear length scales are smaller, implicating higher shear near the canopy top (Miller et al., 2017). This dependence on the above-canopy wind vector and stability also holds implications for the location of the inflection point, and thus on the definition of the canopy height (Miller et al., 2017).

1.1.3 Common Methods

Canopy turbulence has been described using high frequency wind and temperature measurements (e.g. Christen et al., 2007; Launiainen et al., 2007; Miller et al., 2017), theoretical considerations (e.g. Wilson and Shaw, 1977; Finnigan, 2000; Finnigan and Belcher, 2004), wind tunnels and flume measurements (e.g. Shaw et al., 1995; Poggi et al., 2004; Böhm et al., 2013), and numerically using large eddy simulations (e.g. Finnigan et al., 2009; Bailey and Stoll, 2013, 2016). As the present study deals with data collected in the field, focus is given to similar studies, including methods of field data collection and analysis.

In most of the studies on CSL turbulence, at least one 3D sonic anemometer is set up to capture high frequency wind and temperature measurements of the flow (e.g. Launiainen et al., 2007). Often, the set-up includes instruments mounted vertically to capture the mean and turbulent profiles of wind and scalars. In a few studies, set-up of instrumentation has been on a horizontal transect, but the focus of these studies have been on the description of advection of CO_2, and occasionally the advection of heat and momentum (e.g. Thomas, 2011), rather than on the spatial nature of turbulence in the CSL. Commonly, averaging periods for CSL turbulence studies are the classical 30-minute periods (Christen et al., 2007; Launiainen et al., 2007; Miller et al., 2017). However, Dupont and Patton (2012) utilise a 5-minute averaging period for stable cases in their study of turbulence within an orchard, with the assumption that this period is small enough to avoid larger-scale trends and large enough to capture the largest scale turbulent fluctuations in the flow.

Time-series of scalar fields reveals the ramps associated with the predominant mode of sweeping and ejecting motions in the flow (Gao et al., 1989; Paw U et al., 1992). Conditional sampling such as the use of a quadrant analysis (Antonia, 1981) has elucidated the dominant modes, efficiency, and intermittency of turbulent transfer in teh RSL (Raupach, 1981; Christen et al., 2007; Launiainen et al., 2007; Poggi and Katul, 2007). The same information on turbulent transfer can be alternatively obtained using an analysis on the third and fourth order statistical moments (Launiainen et al., 2007; Poggi and Katul, 2007).

Integral statistics have allowed for the identification of characteristic turbulent scales. Integral methods typically involve the integration of time lagged single-point correlations to derive a dominant time scale for coherent structures (e.g. Shaw et al., 1995; Christen et al., 2007), and then the application of Taylor's frozen eddy hypothesis and an estimated convection velocity ($uc = 1.8u$) to formulate a single-point dominant length scale (e.g. Shaw et al., 1995; Christen et al., 2007; Launiainen et al., 2007). In the case of spatially separated sensors, a two-point length scale can be calculated using distance-lagged correlations (Shaw et al., 1995). Finally, the lagged correlations, as functions of lagged time or distance, can be used as a visualisation method for the coherent structures in the flow (e.g. Shaw et al., 1995; Christen et al., 2007).

For revealing the variety of turbulent scales, spectral analysis can be employed (e.g. Finnigan, 2000; Miller et al., 2017). However, as the Fourier transform is not localised in space/time, a more robust method for describing the variety of interacting turbulent scales is the use of a wavelet based analysis. Because wavelets retain the spatial/temporal information in the frequency spectrum, they can be used to locate structures and derive eddy spacing and frequency (e.g. Collineau and Brunet, 1993; Thomas and Foken, 2007*b*).

1.2 Drainage Wind

Under weak synoptic pressure gradients and relatively clear night skies over complex terrain, surface cooling induces negative buoyancy over a slope leading to the development of a down-slope (drainage) wind. Drainage wind is a common occurrence that influences local and regional climate (e.g. Sturman et al., 1999) and holds important implications for the transport of pollutants (e.g. Moroni et al., 2014; Chemel and Burns, 2015), the formation of cold air pools (e.g. Burns and Chemel, 2015; Geiss and Mahrt, 2015), CO_2 budgets (e.g. Aubinet et al., 2003), the formation and dissipation of fogs and low clouds, and the distribution of surface air temperatures which holds implications for frost damage in vineyards and orchards (Zardi and Whiteman, 2013). However, despite their importance in a variety of processes, drainage winds are often unresolved in current numerical weather prediction models and standard measurements (e.g. Grisogono et al., 2015). Further complicating this is the paucity of information on drainage winds over varying canopies, such as a vineyard canopy. In the following section, a brief overview of the theory and characteristics of drainage wind is provided and common observational techniques are reviewed.

1.2.1 Brief Theory and Characteristics of Drainage Flow

Drainage wind is a (generally) nighttime occurrence that develops over a slope due to the cooling of the slope atmosphere (e.g. Whiteman, 2000). This cooling occurs via a loss of radiative heat from the slope surface and a transfer of sensible heat from the near-slope air to the ground (e.g. Whiteman, 2000). As the slope air cools, a horizontal temperature gradient develops between the air just above the slope surface and that over the valley, leading to negative buoyancy along the slope which then drives the air to flow down-slope under the influence of gravity (e.g. Ball, 1956; Haiden and Whiteman, 2005; Poulos and Zhong, 2008; Mo, 2013; Zardi and Whiteman, 2013). Typically, the drainage flow is associated with temperature inversions that start at the slope surface, there is a near surface wind speed maximum, and a near-surface peak in the TKE (Figure 1.1).

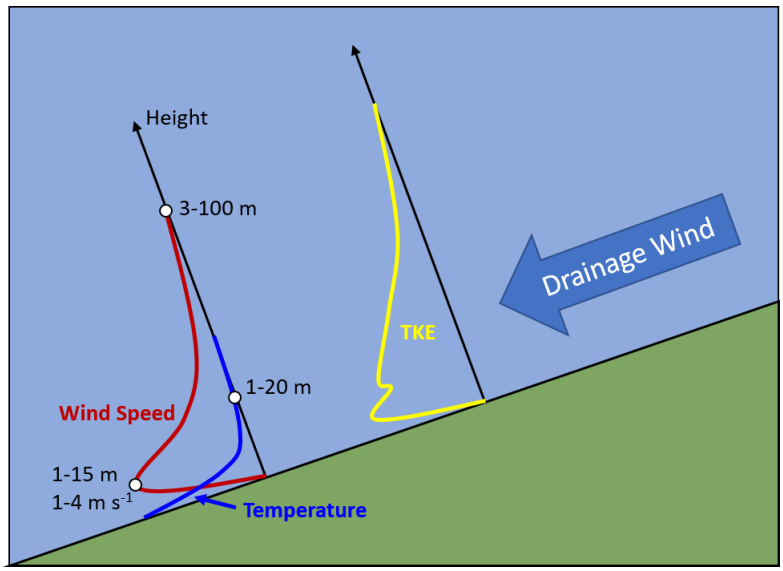

Figure 1.1: Schematic of typical temperature, wind, and turbulent kinetic energy (TKE) vertical profiles for the nighttime drainage wind, modified from the image provided in Zardi and Whiteman (2013).

Inversion depth defines the depth of the drainage layer, which can be on the order of 1 - 200 m (e.g. Amanatidis et al., 1992; Zardi and Whiteman, 2013). Ideally, the jet maximum occurs around 30-60% of the inversion depth, and decreases to zero at the top of the inversion layer (e.g. Zardi and Whiteman, 2013). Estimates for the depth of the inversion layer can be made using vertical drop distance from the ridge (e.g. Horst and Doran, 1986; Amanatidis et al., 1992), but different estimation techniques, which have been based on field data, yield different values for the location of the jet maximum. Theoretically, a return flow exists above the inversion layer, but, this is a rarely observed phenomenon in the field (e.g. Zardi and Whiteman, 2013; Burns and Chemel, 2015).

1.2.2 Typical Drainage Onset Conditions

The development of strong, locally generated, drainage flow is associated with outgoing long-wave radiation amounts of at least 30 W m^{-2}, while weaker flow can still develop for amounts as low as 15 W m^{-2} (Gudiksen et al., 1992). Synoptic activity must be weak, with larger-scale winds typically not exceeding 5 m s^{-1} (Gudiksen et al., 1992). This larger scale flow threshold is apparently variable, with other thresholds observed in association with drainage flow in the literature (2-3 m s^{-1} for Zardi and Whiteman (2013) and 6 m s^{-1} for Papadopoulos et al. (1997)). Naturally, there arises a seasonal dependence in many locations for drainage flow, requiring times when nighttime skies are relatively clear, synoptic pressure gradients are weak, and the atmospheric and soil moisture are relatively low (Devito and Miller, 1983; Gudiksen et al., 1992; Banta and Gannon, 1995; Komatsu et al., 2003; Zardi and Whiteman, 2013).

1.2.3 Observational Techniques

Historically, drainage winds have been observed and characterised using data collected through a vertical transect of the atmosphere either with tower mounted anemometers at various height levels (e.g. Papadopoulos et al., 1997; Aubinet et al., 2003; Froelich and Schmid, 2006; Rebman et al., 2010; Oldroyd et al., 2014) which provide a snapshot of the vertical structure with time, or with a single anemometer that is moved through the vertical in time, i.e. a tethered-balloon sounding (e.g. Manins and Sawford, 1979; Devito and Miller, 1983) which is a resource saving alternative, but is only appropriate if the wind can be assumed stationary. The use of fog machines has helped to visualise drainage flow dynamics (e.g Pypker et al., 2007).

Most studies using tower data have looked at point measurements (e.g. Oldroyd et al., 2014), with a few more recent studies deploying multiple tower point measurements around a sloped region for a more complete picture of the flow (e.g. Staebler and Fitzjarrald, 2005). However, drainage flow is not stationary (e.g. Mahrt, 2010), is highly sensitive to a variety of parameters that are typically not constant along or across a slope, and normally contains other sub-meso motions and gravity waves within the wind structure as well (e.g. Mahrt, 2014). This makes sparse point measurements aimed at characterising the structure of a drainage flow problematic.

In recent years, field investigations have begun to deploy instrumentation capable of the high spatial and temporal resolution needed to completely characterise drainage flow, like the 2D distribution of high resolution fibre-optic temperature sensors used by Thomas et al. (2012), and the thermal infrared screen and camera methods devised by Grudzielanek and Cermak (2015). While these new techniques present an op-

portunity to greatly further complete understanding on the dynamics of drainage wind, they have to date only been applied over grassy slopes.

1.3 Study Objectives

While numerous studies have characterised CSL turbulence for various canopies, most of the studies have focused on turbulence under near-neutral conditions. The few studies that have considered stability have done so for more homogeneous canopies - like tall forests (either dense or sparse) (e.g. Thomas and Foken, 2007*a*). While attention is beginning to turn to row-gap organised agricultural canopies, such as vineyards (Francone et al., 2012; Chahine et al., 2014; Miller et al., 2017), to our knowledge, the consequence of nighttime drainage within a vineyard has not been examined.

As the major wine-producing region of British Columbia, most of the vineyards in the Okanagan Valley are situated on or near complex terrain. To date, topographically forced drainage has not been resolved within and above canopies, let alone how the presence of drainage affects CSL turbulence and the communication between the atmosphere and the canopy. To understand the local affects of drainage and the advection of scalars and momentum, which hold potential implications to both vineyard and human health, the turbulent field within a vineyard under drainage conditions needs to be understood.

To this end, the goals of this study are to 1) characterise nighttime drainage flow within the vineyard CSL, and 2) quantitatively and qualitatively describe the turbulent exchange of heat and momentum within the vineyard CSL during the drainage events. Fulfilling these two objectives allows for a more robust understanding of the implications of nighttime drainage within an organised canopy with consequence to nighttime advection and dispersion of scalars, including heat and disease/pollutants, and to the canopy-atmosphere exchange of heat and momentum.

2 Methods

2.1 Field Site Description

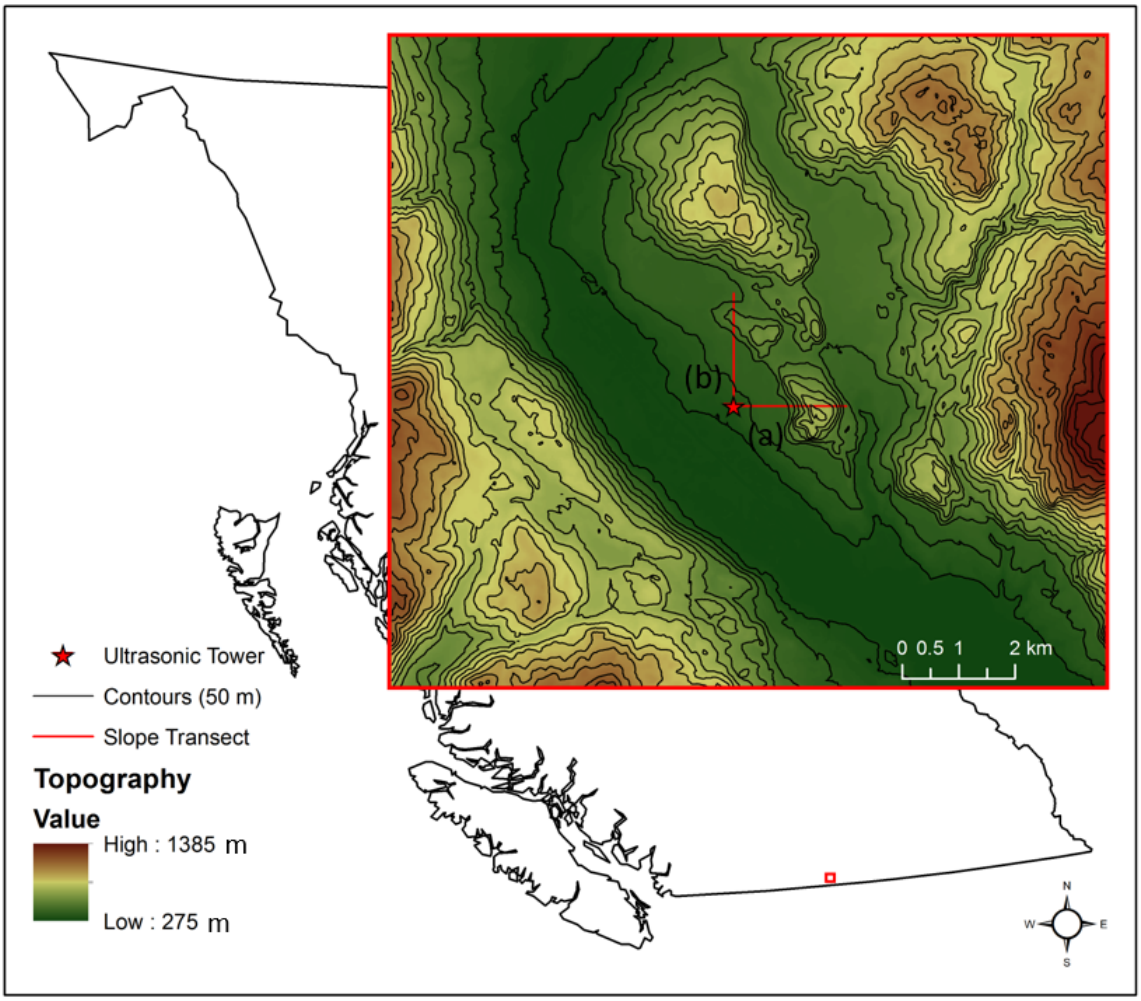

Figure 2.1: Topographic map of the southern Okanagan Valley. Map of British Columbia was obtained from ESRICanadaED (https://www.arcgis.com/home/item.html?id=dcbcdf86939548af81efbd 2d732336db). Map projection is BC Albers 1984. Scale provided is for the coloured topographic map.

The field campaign took place on a west-facing ∼7° vineyard slope on Burrowing Owl Estate Vineyard (BOV) property in Oliver, British Columbia, Canada. The particular plot was populated with Chardonnay grapevines, and was irrigated using a drip-method. This site is located within the Black Sage - Osoyoos viticulture region, which is dominated by sandy, rapidly draining soil with very low moisture holding capacity (Bowen et al., 2005). BOV property in Oliver is located approximately 3 km up-valley (north) from the northern tip of Osoyoos Lake, with the specific field site slope approximately 1 km down-slope (west) of the foot of steeper mountain terrain leading into the Inkadeep territory. A topographic map of the region

surrounding the study site, as well elevation profiles extending east (Figure 2.2(a) and north (Figure 2.2(b)) 2 km from the ultrasonic tower location (Mast A, Figure 2.3) is provided by Figure 2.1. The slope transect provided in Figure 2.1 correspond with the elevation transect provided in Figure 2.2. The slope of the chosen site was measured using an inclinometer iPhone application, to an assumed accuracy of $\pm 1°$, see Section 5 for an analysis and discussion on the implication of an inaccurate slope measurement on measured wind components and reported fluxes. The vineyard canopy was maintained at a height, h_c, of on average 2.3 m above ground level (AGL), with a fruit line at 0.65 m AGL; there were approximately four vine trunks per 6 m, and a row spacing of 3 m (Figure 2.3). Regular maintenance of the vineyard ensures that the row spacing is consistent. Throughout the campaign, vines deviating from the row were clipped back to ensure continuity. Vines were watered in the morning, to our knowledge, using a drip-watering system.

Table 2.1 summarises the time line of the set-up procedure, and all instrumentation related issues encountered during campaign. Most issues were related to thunderstorm activity in the region.

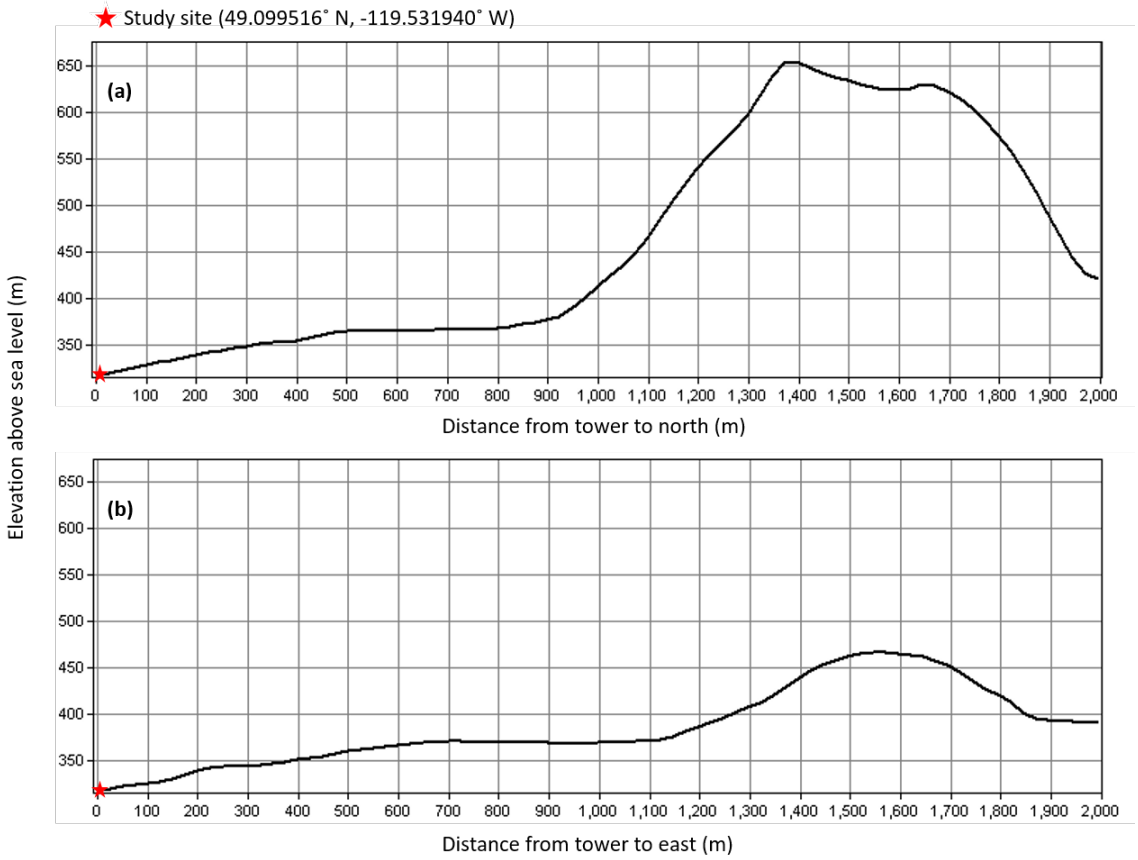

Figure 2.2: Elevation (m above sea level) transects between the ultrasonic tower and 2 km (a) east and (b) north.

Date (dd/mm/yy)	Site Visit Details
04/07/16	Arrive at field site early afternoon; Choice of exact field site slope made.
05/07/16	Set up of instrumented tower, including placement of CR3000 and CR1000 logger boxes, and AM25T boxes (2).
06/07/16	Installment of along-slope thermocouple masts. Thermocouples begin collecting data in early evening.
07/07/16	All thermocouples at below $z/h = 2$ removed due to approaching evening thunderstorm. Time of removal began around 12:30 LST.
09/07/16	Thermocouples replaced on masts by 14:30 LST.
10/07/16	CR3000 fuse breaks around 02:00 LST. Fuse is replaced at 12:00 LST. Thermocouple H3 replaced due to solder joint failure. Logger clocks were unaffected by main fuse break.
11/07/16	Battery accidentally connected at 10:45 LST briefly during regular site maintenance.
12/07/16	Lateral thermocouple masts installed between 10:30 and 11:40 LST.
15/07/16	All thermocouples at below $z/h = 2$ removed due to approaching evening thunderstorm. Time of removal began around 20:30 LST.
16/07/16	Thermocouples replaced on masts by 14:00 LST.
20/07/16	Thermocouples AR2, C1, C4, and F3 are replaced. AR thermocouple mast turned 90° at some point during measurements, and returned to original location during site visit.
22/07/16	All instrumentation removed from field site and returned to UBC.

Table 2.1: Time line of field campaign in the southern Okanagan Valley in July 2016.

2.2 Instrumentation

Five ultrasonic anemometers (CSAT-3D, Campbell Scientific Inc., Logan, Utah, USA) were co-mounted with five Type-E 0.001" thermocouples (TC, OMEGA Engineering, Laval, Quebec, CA) on a 4.73-m tall pump up tower (Figure 2.4) at vertical heights above ground level (AGL) of 0.45, 0.9, 1.49, 2.34, and 4.73 m. TCs were constructed by hand, except for the 0.001" bare Chr-Con junctions, which were factory-welded by OMEGA Engineering. Details on the construction of the fine-wire TCs can be found in Figure 2.5. Three

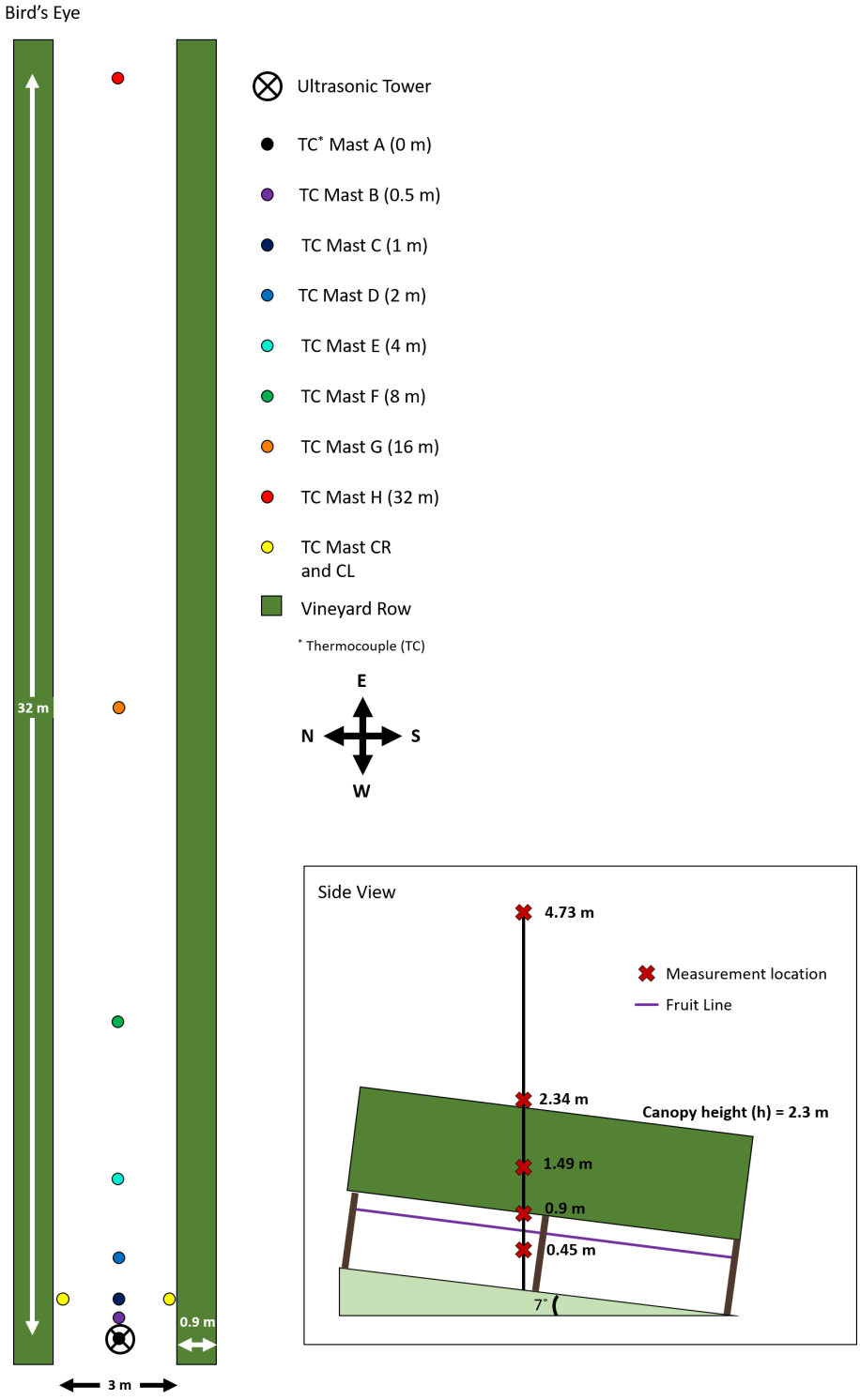

Figure 2.3: Schematic of field site set-up. Bird's eye view provides to-scale spacing of thermocouple (TC) masts and the ultrasonic tower. The side-view provides a to-scale visual of the vertical alignment of CSAT-3D's on the pump-up tower and the TCs on respective masts.

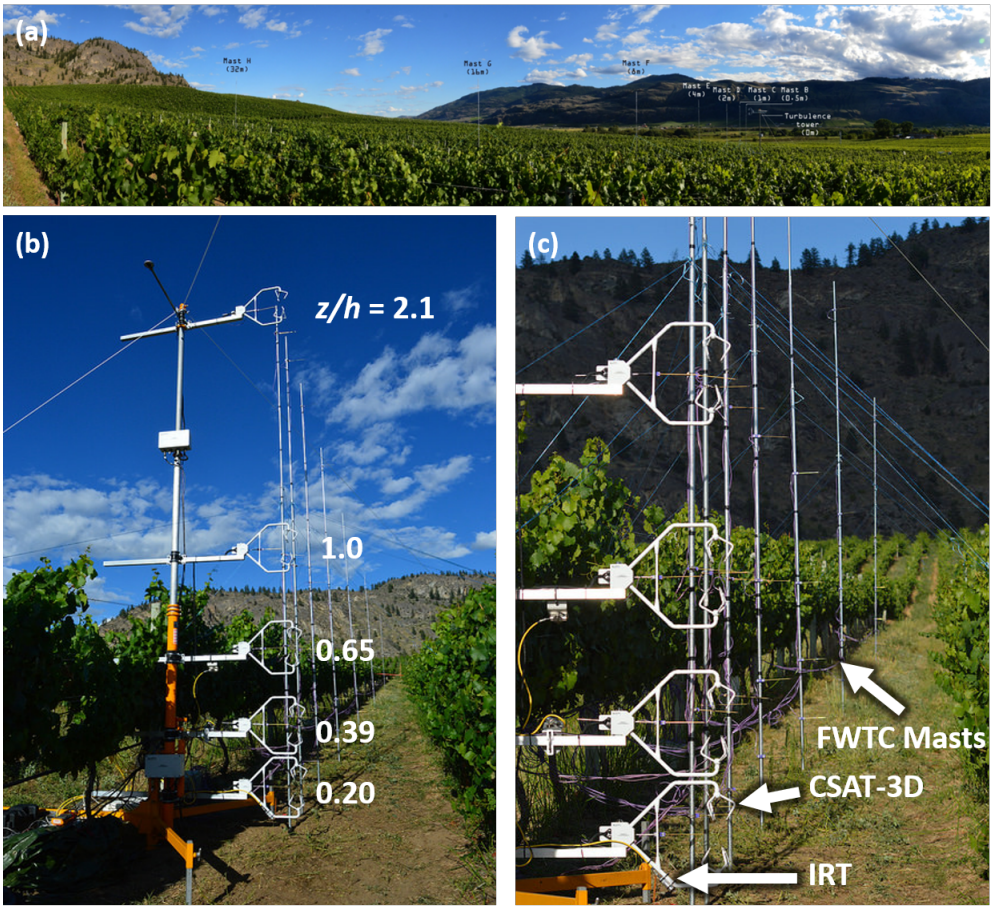

Figure 2.4: Photos of the field site. (a) is a panorama view from east (90°) over south to west (270°) of the vineyard plot where the study slope is located, position of thermocouple (TC) masts and ultrasonic tower are labelled (see also Figure 2.3). (b) is a close-up view looking up-slope (east) of the ultrasonic tower, with labelled vertical positions of the individual CSAT-3D's normalised by the canopy height $h_c = 2.3$ m AGL. (c) provides a close-up of TC mast set-up, the position of some of the TCs and the infrared thermometers (IRTs) that were mounted on the tower. Credit: A. Christen.

infrared thermal (IRT, Apogee Instruments Inc., Logan, Utah, USA) sensors were mounted on the tower, one directed at the ground below the ultrasonic array, one at the vegetation to the north of the tower, and one at the vegetation to the south of the tower. Seven TC masts (A - H) were placed up slope of the ultrasonic tower at distances of 0.5, 1.0, 2.0, 4.0, 8.0, 16.0, and 32.0 m to the east of the ultrasonic tower, on which five TCs each were mounted at heights AGL of 0.45, 0.9, 1.49, 2.34, and 4.73 m. Two additional TC masts were placed near the vegetation to the north and the south of the TC mast located at 1.0 m from the tower (Figure 2.3), with TCs placed at heights AGL of 0.45, 0.9, 1.49, and 2.34 m. All fine-wire TCs were multiplexed by two Campbell Scientific AM25T multiplexers; TCs on Masts A - C (including CN and CS, Figure 2.3) were multiplexed by AM25T1 (multiplexer closest to the ultrasonic tower), and TCs on Masts D - H were multiplexed on AM25T2 (multiplexer furthest from ultrasonic tower). The tower and the TC masts were secured in place throughout the campaign by guy wires extending into adjacent rows. All CSAT-3Ds, TCs and IRTs were logged by a Campbell Scientific CR3000 data logger. CSAT-3Ds were run at 60 Hz with a 20 Hz sampling frequency; TCs and TIRs were sampled at 2 Hz. An NR Lite2 Net radiometer was mounted facing west at 4.8 m AGL on the pump-up tower, set to sample and integrate at the slow, or 60-Hz rejection integration; samples were further averaged into 1-minute values and logged by a Campbell Scientific CR1000 data logger. Six extension-grade type-E TCs were placed in a vertical array in the soil spaced at 1 cm (Figure 2.6(a)). The soil thermocouple array was located near the centre of the adjacent row to the north of the site, and were sampled and logged at 1-minute intervals by the CR1000 data logger. Volumetric soil water content was sampled once a day during data download at the tower location (0 m) and at TC mast H (32 m up-slope) using a Campbell Scientific HydroSense Soil Water Measurement sensor.

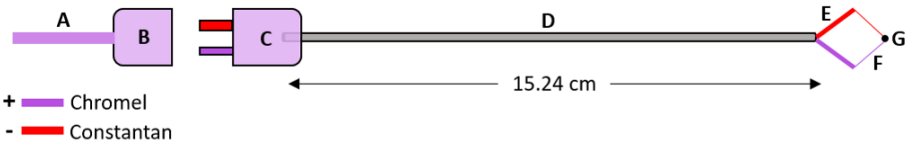

Figure 2.5: Schematic of fine-wire thermocouple (TC) deployed on slope for air temperature measurements. A: Polyvinyl shielded Chromel-Constantan (Chr-Con) extension grade wire (EXPP-E-24S-SLE) is connected to B: female connector which connects to C: male connector which connects to 30-gauge Chr-Con wire which feeds into D: a small brass protection tube of length 15.24 cm. E: the 30-gauge wire is then soldered to F-G: the 0.001" factory-welded bare Chr-Con TC junction. F represents the Chr-Con 0.001" wires, and G represents the factory-welded junction.

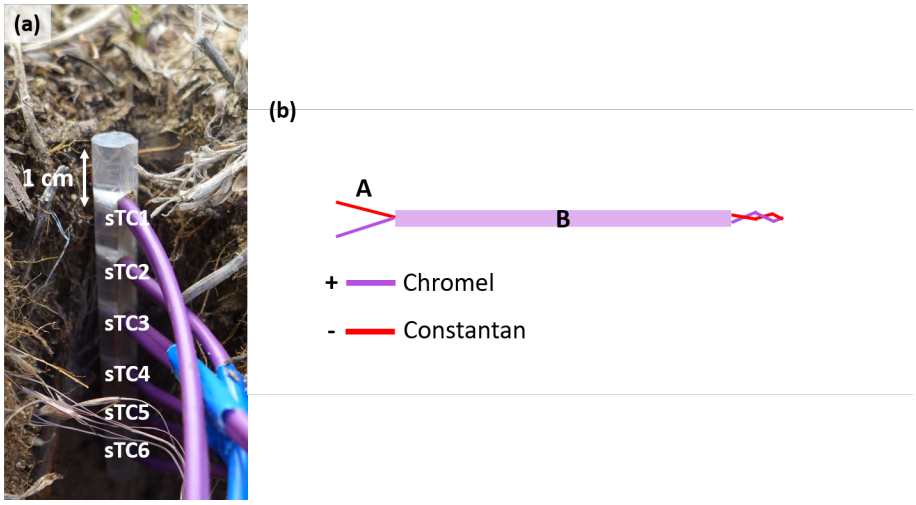

Figure 2.6: (a) Soil thermocouple (TC) array, located in the centre between the N-vegetation row and the adjacent row the the N of the study site. Six TCs constructed from polyvinyl shielded Chromel-Constantan (Chr-Con) extension-grade wire are spaced at 1 cm, with the topmost measurement at 1 cm below the soil surface. Note that photo was taken during installation; soil was filled in afterwards. (b) Diagram of soil TC. A: Extension-grade Chr-Con wires; B: Polyvinyl-shielded extension-grade Chr-Con wire. Soil TCs are constructed by twisting the ends of the Chr-Con wires to create a 'junction'. Chromel wires are coloured purple, and are the positive legs; Constantan wires are coloured red, and are the negative legs.

2.3 Measurement Uncertainties

2.3.1 Campbell Scientific 3D Sonic Anemometer

All of the ultrasonic anemometers employed in this study were part of an inter-comparison campaign in 2009 (Liss et al., 2009). Following the methodology of Emmel (2014), the calculated standard deviations from the inter-comparison campaign are used as the instrument related uncertainties. The uncertainties calculated for CSAT-3D 1341, which was the CSAT-3D positioned at the canopy top, are used in the present study as the instrument uncertainties for mean wind components, wind speed and temperature, Reynold's stresses and heat flux, turbulent kinetic energy (TKE), and velocity and temperature skewness (Table 2.2). As the uncertainty in $\overline{u'v'}$ was not given, it is calculated as the average between the uncertainty in $\overline{u'u'}$ and $\overline{v'v'}$.

Quantity	Uncertainty
$\overline{u}$	0.05274 m s^{-1}
$\overline{v}$	0.03627 m s^{-1}
$\overline{w}$	0.01335 m s^{-1}
$\overline{T}$	0.05286 K
$\overline{U}$	0.05674 m s^{-1}
$\overline{u'u'}$	0.02229 m^2 s^{-2}
$\overline{u'w'}$	0.00517 m^2 s^{-2}
$\overline{v'v'}$	0.01863 m^2 s^{-2}
$\overline{v'w'}$	0.00921 m^2 s^{-2}
$\overline{w'w'}$	0.00777 m^2 s^{-2}
$\overline{w'T'}$	0.00463 m K s^{-1}
$\overline{u'v'}$	0.03226 m^2 s^{-2}
Sk_u	0.08460 m s^{-1}
Sk_v	0.12312 m s^{-1}
Sk_w	0.07910 m s^{-1}
Sk_T	0.39635 K

Table 2.2: Table of CSAT-3D instrument uncertainty, as calculated from reported standard deviations in Liss et al. (2009)

Uncertainty in the vertical gradients of above-mentioned quantities is calculated using:

$$U_a dz = \frac{U_a}{dz} \tag{2.3.1}$$

where $U_a dz$ is the uncertainty in the vertical gradient and U_a is the uncertainty in the measurement. For the velocity gradients, a cubic spline was used to determine gradients at the measurement points using a layer of thickness = 0.04 m. The error in the velocity gradient is calculated as in equation (2.3.1), with the knowledge that the use of the natural cubic spline may affect the reported errors. Because the gradient used is so small, the error in the reported velocity gradients is large, despite the fact that with increasing measurement distance, the error in determining a gradient between the two sensors is reduced. The amount of curvature is assumed to be reduced through applying the natural cubic spline interpolation only on the 5-minute averaged data points.

2.4 Post-Processing

2.4.1 CSAT-3D Rotations

Coordinate rotation is an important step in the use of turbulence data. While there are a variety of methods available for coordinate rotation of CSAT-3D components (Lee et al., 2005), we employ a two-step rotation similar to the planar fit method in that we rotate the system into a plane parallel to the slope surface. The first rotation aligns the x-axis with the mean wind direction (using traditional meteorological wind direction definitions) using the rotation matrix $R1$:

$$R1 = \begin{bmatrix} -cos(\alpha) & -sin(\alpha) & 0 \\ -sin(\alpha) & -cos(\alpha) & 0 \\ 0 & 0 & 0 \end{bmatrix} \tag{2.4.1}$$

where α is the 30-minute averaged wind direction at $z/h_c = 2.05$, also referred to as the pitch angle. The rotation is set up such that $+x = 90°$ is flow directed down slope (*i.e.*, wind comes from the east). The choice of using the averaged wind direction at $z/h_c = 2.05$ has the possible consequence of non-zero mean cross-slope wind at the lower measurement heights. For this reason, Reynolds stresses cannot be simplified, and when possible, all terms are calculated and reported.

The second rotation aligns the z-axis with the local slope via a rotation about the y-axis using rotation matrix $R2$:

$$R2 = \begin{bmatrix} cos(\beta sin(\alpha)) & 0 & -sin(\beta sin(\alpha)) \\ 0 & 0 & 0 \\ sin(\beta sin(\alpha)) & 0 & cos(\beta sin(\alpha)) \end{bmatrix} \tag{2.4.2}$$

Where β is the slope, or yaw, angle. Directionally dependent yaw rotations have been applied in other studies on flow measurements within a sub-canopy environment (e.g. Mahrt and Lee, 2005; Francone et al., 2012; Miller et al., 2017), and our use of a sine function is justified by observed sinusoidal behaviour of streamlines with varying wind direction at the site (Figure A1, Appendix 5). This rotation assumes that the slope is planar and oriented E-W, which is generally true, but could be modified due to the highly variable terrain in the region. However, rotation into one plane allows for the calculation of vertical gradients in a straightforward manner. Sub-canopy momentum fluxes are sensitive to the choice of rotation method (e.g. Mahrt

et al., 2000; Mahrt, 2010; Francone et al., 2012), thus it is necessary to consider the overall implications of the current choice of methods.

While both the pitch and yaw rotations merely redistribute fluxes, vertical fluxes are highly sensitive to the choice of yaw rotation method (if employed at all). In the case of a sloped environment, a slope rotation should be employed, but, it is recognised here that the errors in the slope angle measurement may hold implications for the sign of reported fluxes. Over-rotation would be especially problematic in the current study given the implied (and interpolated) location of a jet maximum within the measurement domain (see Figure 3.8(a) in Section 3.2). Analysis on the effect of rotation errors with relation to potential momentum flux sign changes reveals little to no effect on the total fluxes presented here (see Appendix 5 for details). Appendix 5 additionally provides the mean absolute error (MAE) in the calculated fluxes associated with a $\pm 1^{\circ}$ measured slope angle uncertainty.

The uncertainty in the measured slope angle will be most critical to the octant and associated analyses. Given that the largest (potential) errors are concentrated during low-flux times, use of a hyperbolic hole in all octant and associated analyses circumvents the issue of potential uncertainty induced momentum flux sign changes. Therefore, a hole size of $H = 3$ for vertical stresses and a hole size of $H = 1$ for horizontal stresses is applied for all octant related analyses (see Section 5 for details).

2.4.2 CSAT-3D Wind Components

Theoretically, under zero-wind conditions, the ultrasonic anemometers should measure zero for all wind components. However, this is not the case in reality, and while factory specific offsets are provided by Campbell Scientific Inc (2015), instrument specific offsets are calculated in the present study.

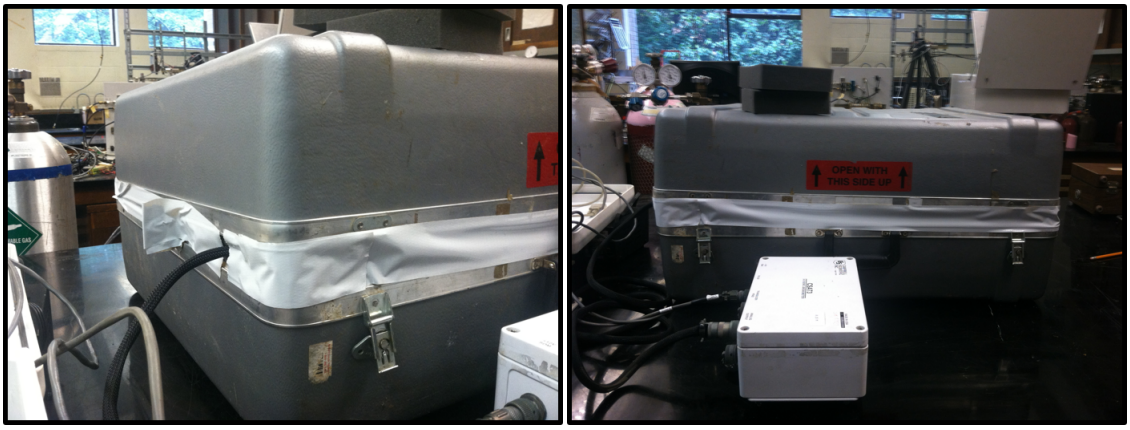

Figure 2.7: Photos of CSAT-zeroing set-up.

To test the ability of the ultrasonic anemometers deployed during the 2016 Okanagan field campaign to reach zero (*i.e.*, during no-wind conditions), a radius of approximately 6 cm of protective foam was removed from the ultrasonic anemometers storage containers where the 'head' of the sensor normally rests. The ultrasonic anemometers were sealed (using duct tape) in their cases, with additional foam added to the exit site of the SDM connection cable for the sensor as damage protection (see Figure 2.7). The ultrasonic anemometers were then connected to the data logger and run for at least 24 hours in a temperature controlled lab. The lab is occasionally frequented during the day, and empty and locked during the night. Because it is recognised that small thermal gradients could potentially develop around the sensor, particularly during the night, a variety of case rotations were conducted to investigate the effect on the mean measured components as they cycled through representing the vertical wind. Each case rotation was tested for the same diurnal cycle. Vertical thermal gradients and diurnal changes in temperature did not affect the wind components and quality of zero-tests, thus were not accounted for in the final offset calculations. Table 2.3 provides the final offset values applied to the ultrasonic anemometer data as a first step in post-processing.

Ultrasonic Anemometer (CSAT-3D) Serial Number	z/h_c	Wind Components		
		x	y	z
0428	2.05	-0.0388 m s^{-1}	0.0221 m s^{-1}	-0.0064 m s^{-1}
1341	1.01	-0.0909 m s^{-1}	0.0377 m s^{-1}	-0.0051 m s^{-1}
1389	0.647	0.0028 m s^{-1}	0.0354 m s^{-1}	-0.0365 m s^{-1}
1393	0.391	0.1047 m s^{-1}	-0.1159 m s^{-1}	0.0554 m s^{-1}
1396	0.195	0.0744 m s^{-1}	0.0138 m s^{-1}	0.0056 m s^{-1}

Table 2.3: Corrections obtained through ultrasonic anemometer zero-wind calibration tests. ultrasonic anemometers are identified by serial number, and their vertical placement on the flux tower indicated (z/h_c; z = height AGL, h_c = height of canopy). Corrections for x- y- and z- were subtracted from all CSAT-3D measurements.

All of the corrections are on the order of 1 cm s^{-1}, except for CSAT-3D 1393 ($z/h_c = 0.391$) yielded corrections values of ∼10 cm s^{-1}. Running under the assumption that the applied zeroing methods were adequate (it is argued that the method deployed is superior to common bag methods deployed), this indicates a potential issue with CSAT-3D 1393. However, it seems as though the application of the corrections makes vertical gradients more physically reasonable (Figure 2.8), and confidence is still held in all of the ultrasonic anemometers deployed during the campaign.

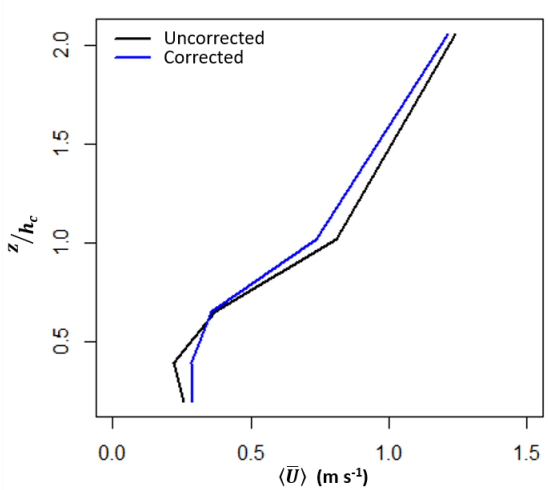

Figure 2.8: Vertical profiles of mean wind speed for case study on the night of 06/07/2017. $U_i = \frac{1}{N}\sum_{t=1}^{N}\sqrt{\bar{x}_i(t)^2 + \bar{y}_i(t)^2}$, where N = number of 30-minute records in case study night (18), $\bar{x}_i(t)$ is the 30-minute mean of component x for record t, and index i indicates the CSAT-3D at which the average is calculated.

2.4.3 CSAT-3D Acoustic Temperatures

It is well known that the mean acoustic temperatures measured by the CSAT-3D ultrasonic anemometers tend to drift, due to sensitivity to humidity and other quantities that affect the speed of sound, thus yielding

unreliable mean temperatures. To correct for any drift, five minute averaged acoustic temperatures are compared with five minute averaged tower co-mounted TC temperatures (Mast A) for all of the selected case studies. Using this select grouping of data ensures that the corrections not only avoid daytime radiation errors, but also ensures that the comparison is made during times when both the ultrasonic array and the TC array were operating properly. Figure 2.9(a) and Table 2.4 summarise the acoustic temperature offsets. The mean difference between CSAT-3D measurements and TC measurements of temperature were subtracted from the acoustic temperatures prior to further investigation. Figure 2.9(b) shows improved agreement between two temperature measurements post correction.

z/h_c	**Correction (K)**
2.06	1.334
1.02	1.616
0.647	0.134
0.391	2.424
0.195	0.948

Table 2.4: Calculated mean difference between CSAT-3D acoustic temperature and the mean thermocouple temperature.

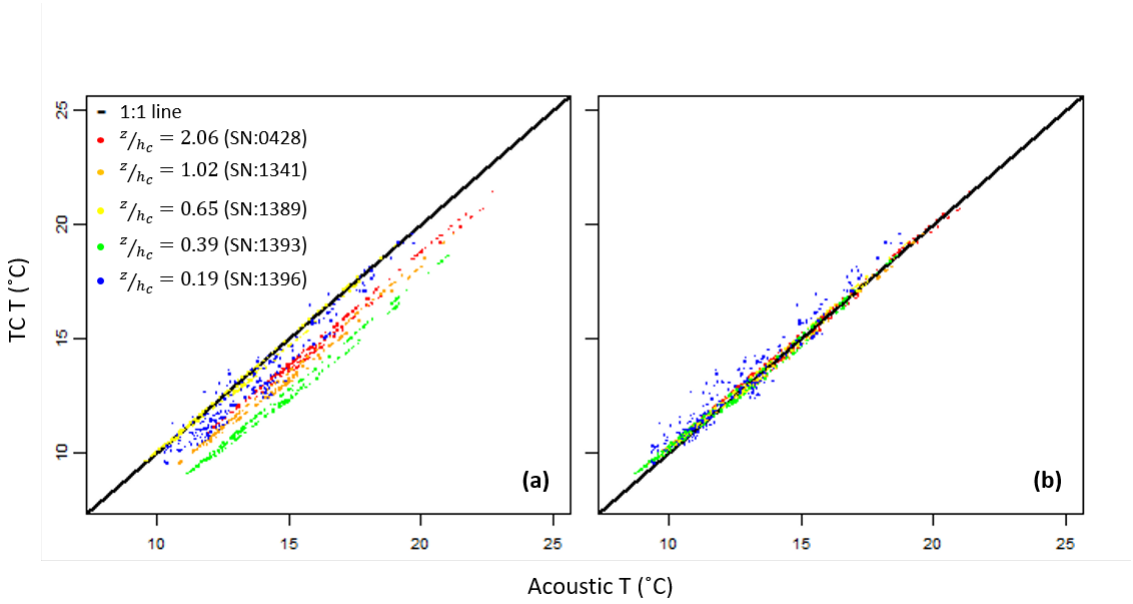

Figure 2.9: Comparison between the CSAT-3D acoustic temperatures and the thermocouple (TC) temperatures before (a) and after (b) applied acoustic temperature corrections.

2.4.4 Thermocouple Temperatures

During the nighttime cases, an unexplained warm bias is observed for the five TC masts (D - H) multiplexed by AM25T2 (located ∼16 m up-slope from AM25T1) at all heights. The bias could be due to either instrumentation failure or some real phenomenon. Post-campaign testing reveals no apparent issue with TC instrumentation, but at present, we are unable to physically explain the bias. To remove the potential effects of this bias from analysis, the five minute average vertical temperature gradient at $z/h_c = 2.05$ between Masts A (0 m up-slope) and H (32 m up-slope) was used to calculate 'reference' five-minute average temperatures at $z/h_c = 2.05$ for the other six masts along the slope. The difference between the 'reference' five minute average temperatures and that of the actual five minute average temperatures at $z/h_c = 2.05$ was then subtracted from the five minute blocks of 2 Hz data for each mast. An example of this calculation is provided in Appendix 5.

In the case that the observed bias is indeed physically based, this adjustment was not necessary. However, as this method corrects temperatures on an average tower basis, there are no implications for the quantities of interest in the present study, like turbulence statistics (*i.e.*, two point length scales) or vertical gradients. The only implication in the present study is that presented absolute TC temperatures are in reference to the 'background' stratification, and only the absolute mean temperatures at Masts A and H are the actual measured temperatures. For this reason, all presentation of first statistics for TC temperatures are for Masts A and H only (and are further specified when reported).

2.5 Case Study Selection

For the selection of case studies, five-minute block averages are analysed. Nighttime is here defined as between 21:30 local standard time (LST) and 06:30 LST. This selection of nighttime includes evening and morning transitions during and right after sunset and sunrise, respectively. The issue of transition is addressed in step 2 of the case study selection process (using a net radiation threshold). A three-step pseudo-objective method was used to select the case studies in the current analysis. In the first step, the evolution of relevant variables (*i.e.*, net radiation (Q^*), temperature stratification (Γ_{local}), wind direction (WD), and turbulent kinetic energy (TKE)) was analysed to subjectively determine whether or not the night had the potential for drainage flow. In the case of strong synoptic activity, lack of winds from the drainage range, and/or no apparent temperature stratification anywhere in the measurement domain, the night was discarded from further analysis. During this first step, drainage events were identified, and the general characteristics of the events were noted (see Table 2.5 and used to inform clustering in step 2). In the second step, the block-

averages are clustered into two groups using a k-means clustering routine, and in the third step, individual cluster identities are redefined to make more physical sense for the drainage cases.

2.5.1 Time Series Investigation

Five nights were excluded from analysis due to stormy conditions and a broken fuse on one of the nights (see Table 2.1). Initial visual inspection of gradient Richardson numbers (R_i) at canopy top, wind direction at canopy top and topmost CSAT-3D, buoyancy frequency (N^2), and local thermal stratification reveal two dominant regimes. The first is the anticipated drainage flow due to temperature stratification and the local sloping terrain (DF); the second is an either presumably stronger valley flow or drainage flow from terrain complexities to the northwest of the site. Figures 2.10 and 2.11 provide the most ideal and stationary examples of a stable DF night and a more neutral VOF night, respectively. Under both regimes, Q^* and N^2 suggest a general stable environment. However, strong local stratification is achieved only during the DF cases. There are two possible explanations for why similar larger scale atmospheric stability can correspond to two different regimes. Either 1) larger scale stability allows for strong valley drainage (which is perpendicular to the vineyard rows) which acts to increase shear generated turbulence in the local vineyard environment, thus mixing out thermal gradients in the vineyard canopy environment and preventing the generation of local drainage; or 2) strong synoptic activity under clear sky conditions prevents the generation of local drainage in the same way that a strong valley flow, or drainage from nearby mountains to the northwest, would. Current data does not allow us to resolve whether or not this is stronger larger scale drainage, or synoptic activity at play, but the direction of the prevailing wind under these locally neutral nighttime cases suggests larger scale drainage.

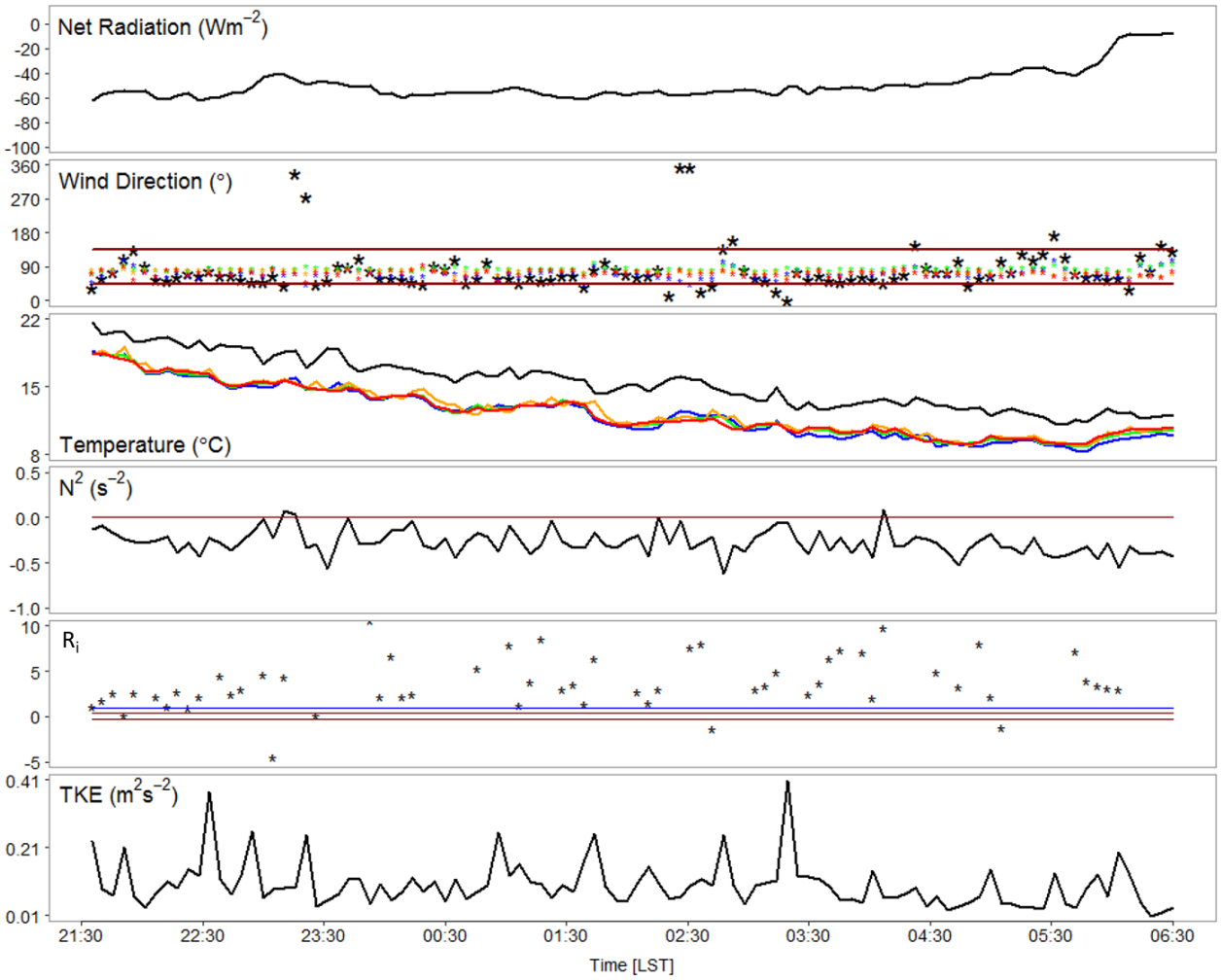

Figure 2.10: Example of a drainage flow night (DF). Five minute averages of variables are plotted for the night of 07 July 2016.

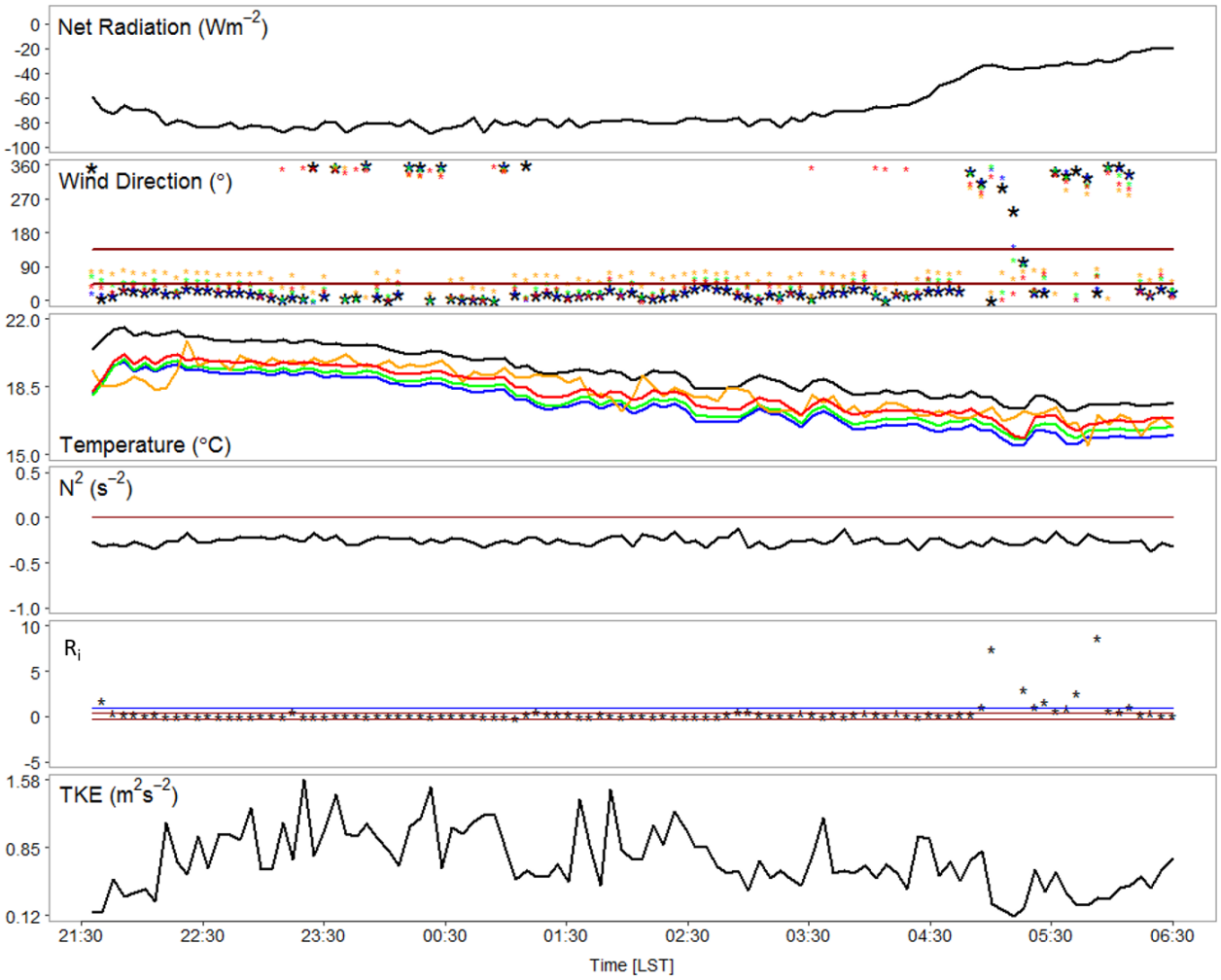

Figure 2.11: Example of a valley drainage or other flow type (VOF). Five minute averages of variables are plotted for the night of 07 July 2016.

Case study nights were selected on the basis of six criteria, four of which differ based on whether or not the period was to be classified as local slope drainage or drainage either down-valley or from other terrain complexities to the northwest of the site. Selection was based on the behaviour of net radiation (Q^*), the buoyancy frequency (N^2), wind direction (WD), local thermal stability (either strong temperature gradient apparent or week/nonexistent), gradient Richardson number (R_i), and the turbulent kinetic energy (TKE, either low/very low or moderate, with relative regards to typical TKE values during the night at field site). Selection criteria are summarised in Table 2.5 below. This method is subjective, and is only carried forward in step 2, during which clustering variables are chosen and thresholds for clusters are defined.

	Slope Drainage	Valley/Other Drainage
Net Radiation	$Q^* < -30\ Wm^{-2}$	
Buoyancy Frequency	$N^2 < 0\ s^{-2}$	
Wind Direction	$45° < WD < 135°$	$0° < WD < 45°$ or $315° < WD < 360°$
Local Stability	Strong	Weak or Neutral
Gradient Richardson number	$R_f i > 1$	$-\frac{1}{3} < R_i < \frac{1}{3}$
Turbulent Kinetic Energy	Low	High

Table 2.5: Summary of selection criteria during initial visually based clustering methods.

2.5.2 K-Means Clustering

As evidenced from time series analysis, drainage events at the site are associated with low TKE and high R_i, whereas the valley flow (or otherwise) events are associated with higher TKE and lower R_i. Using this knowledge, a k-means clustering routine was performed using the five minute bock averaged TKE and R_i at $z/h_c = 2.05$ and $z/h_c = 1.01$ as a more objective separation of cases. The clustering routine was performed on nighttime cases with $Q^* < -30$ W m^{-2}, leaving a total of 639 five minute block averages to be evaluated. The routine was performed for the identification of two clusters, one which contains the drainage events (DS cluster), and the other which contains unrelated events (valley drainage or 'other' flow (VOF) cluster). In the present study, we only focus on drainage events and an exploration of the suspected larger scale valley-drainage events are reserved for a later study.

Further refinement of cluster identification was employed to 'correct' classifications. Cases classified in the DS cluster with block averaged wind directions at $z/h_c = 1.01$ outside of the down-slope domain were re-classified into the VOF cluster. This step redistributed 17 five minute blocks into the VOF cluster. This out-of-range issue is possible during very weak wind conditions outside of the domain, so that despite an enhancement of shear and mixing due to the angle of attack of the wind at the top of the vineyard, TKE is still relatively low. Additionally, cases classified in the VOF cluster with block averaged wind directions at $z/h_c = 1.01$ within the down-slope domain and block averaged temperature gradients (between $z/h_c = 0.2$ and $z/h_c = 2.05$) greater than 1 K m^{-1} were reclassified into the DS cluster. This step redistributed 81 five minute blocks into the DS cluster. All redistribution occurred on the boundary between the two clusters, and in effect adds pertinent directional and stability information to the classifications in the present study. Figure 2.12 provides an example of the separated clusters, following the additional corrections. The reclas-

sification step is justified as it increases the temporal stability of cluster identity and coerces the clustering towards the classifications described in Section 2.5.1. Following the reclassification, drainage events occurred during 25.25 hours of the campaign (∼17.5% of all nights).

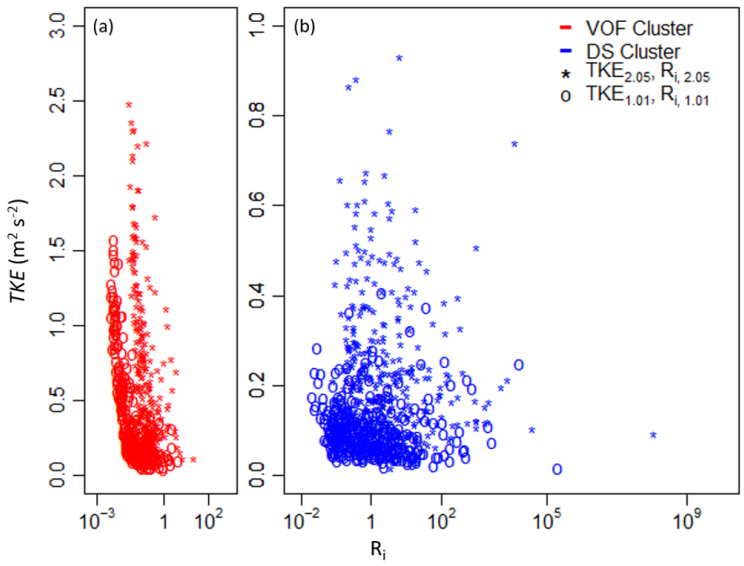

Figure 2.12: Five-minute block averaged turbulent kinetic energy (TKE) versus five-minute block averaged gradient Richardson number (R_i) for all nighttime cases with outgoing net radiation (Q^*) < -30 W m^{-2} at $z/h_c = 1.01$ and $z/h_c = 2.05$. (a) cases with a five-minute averaged wind direction at $z/h_c = 1.02$ outside of the down-slope domain (between 45° and 135°; (b) cases with a five-minute averaged wind direction at $z/h_c = 1.02$ within the down-slope domain. Valley or other flow (VOF) clusters are coloured red; Drainage flow (DS) clusters are coloured blue. TKE and R_i at $z/h_c = 2.06$ are denoted by asterisks, and that at $z/h_c = 1.02$ by open circles.

As the reclassification did not completely ameliorate stationarity issues, a further test is applied to isolate drainage events. Only drainage conditions that persist for at least 25 minutes are considered drainage events. Furthermore, of these drainage events, only the middle 15 minutes is used in further analysis to avoid any 'leakage' from non-drainage events into the analysis (i.e. leakage into the five minute block averages). Furthermore, cases are excluded when the identification switches between regimes more than two times within a 45 minute time period. This conservative time padding allows for further confidence in the selected data for further analysis.

After the time padding, 211 five minute data chunks, or 17.6 hours of the campaign, are classified as drainage events for further analysis, summarised by Table 2.5.2. Occasional TC failure (see Table 2.1) does not affect the selected case studies, however, there are only six hours of side-wall temperature data (Masts CS and CN, see Figure 2.3 available within the selected case studies due to the delay in the set-up of the TCs, and the side-wall TCs breaking easily and often (not reflected in the Table 2.1).

Night	Time Range (LST)
06 - 07 July 2016	21:35 – 00:00
	00:20 – 5:25
12 - 13 July 2016	00:30 – 00:55
	01:20 – 01:40
	02:20 – 5:25
18 - 19 July 2016	03:05 – 03:50
	04:10 – 04:30
	04:50 – 05:25
20 - 21 July 2016	22:45 – 23:20
	03:15 – 06:30

Table 2.6: Summary of selected drainage events.

2.6 Analysis

Averaging Procedure

The five-minute average of a variable, a is denoted as $\overline{a}$, while the ensemble averaged of multiple five-minute averages is denoted, $\langle\overline{a}\rangle$. A five minute averaging period, as opposed to the classical 30-minute period, is chosen to avoid including lower frequency motions in the analysis, and is used in other CSL studies under stable conditions (e.g. Dupont and Patton, 2012).

Spatial averages of the five-minute mean, which can be calculated for the TC array, are denoted with curly brackets, $\{\overline{a}\}$.

Turbulent Flux Calculations

The turbulent portion of a variable, a, is defined as the deviation from the five-minute mean:

$$a'(t) = a(t) - \overline{a} \tag{2.6.1}$$

where t is a time step in the five-minute interval. The variable a stands for the 3 wind components, u, v, and w, and measured temperature, T, and calculated potential temperature, θ.

Turbulent fluxes, or correlations, are then defined as the five-minute average of the product of two turbulent quantities:

$$\overline{a'b'} = \frac{1}{N}\sum_{t=1}^{t=N} a'b' \tag{2.6.2}$$

where N is the number of time steps within the five-minute block, and b is a second dummy variable representing the same parameters as a. The nine possible correlations between the three velocity components make up the Reynolds Stress, τ_{ij}:

$$\tau_{ij} = \begin{bmatrix} u'u' & u'v' & u'w' \\ v'u' & v'v' & v'w' \\ w'u' & w'v' & w'w' \end{bmatrix} \tag{2.6.3}$$

where i and j are indices equal to either 1, 2, or 3, which represent the wind components, u, v, and w, respectively.

Potential Temperature and Stability

Potential temperature, θ is calculated as:

$$\theta = T_z + \Gamma z \tag{2.6.4}$$

where $\Gamma = 0.00981$ °C m^{-1} is the dry adiabatic lapse rate and z is the height in m above ground level. As pressure is not measured during the campaign, we substitute the ground surface for the 1000 mb height.

Canopy top stability is characterised using the Obukhov length:

$$L_o = \frac{u_*^3 \overline{\theta}}{kg\overline{w'T'}} \tag{2.6.5}$$

where $k = 0.4$ is the von Karman constant, $\overline{w'T'}$ is the kinematic heat flux (m °C s^{-1}, and u_* is the friction velocity (m s^{-1}), calculated as:

$$u_* = (\overline{u'w'}^2 + \overline{v'w'}^2)^{1/4} \tag{2.6.6}$$

where both $\overline{u'w'}$ and $\overline{v'w'}$ are used because cross-stream velocities are non negligible. Friction velocities and stability parameters are calculated for the five-minute intervals, and are only calculated at the top of the array where surface layer physics are most likely to still hold.

The Brunt-Väisälä frequency was calculated using the TC array as:

$$N^2 = -\frac{g}{\theta_{A5}} \frac{\theta_{H5} - \theta_{A5}}{dsin(\alpha)} \tag{2.6.7}$$

where g is the acceleration due to gravity, θ_{A5} and θ_{H5} are the potential temperatures at $z = 4.73$ m for Masts A and H, $d = 32$ m is the distance between Masts A and H, and $\alpha = 7°$ is the slope angle.

Ground Heat Flux and Temperature Gradients

Ground heat flux is calculated using:

$$G = -k\frac{dT}{dz} \tag{2.6.8}$$

where $k = 0.68$ W m^{-1} K^{-1} is the approximate thermal conductivity for a sandy soil, calculated as the linearly interpolated value at 6% (the average volumetric soil water content for the site at 12 cm depth) between a volumetric water content of 0% and 10% for a mineral soil. Negative G is defined as heat entering the subsurface, whereas positive G is defined as heat leaving the subsurface. The soil thermal gradient is calculated as:

$$\frac{dT}{dz} = \frac{T_{IRT} - T_{TC6cm}}{0 - 0.06} \tag{2.6.9}$$

Wind Direction Difference

Following the methods of Miller et al. (2017), the difference between the wind direction as the top of the canopy ($z/h_c = 1.02$) and the direction of the vineyard row (90°), δ, is calculated as:

$$\delta = |90° - \overline{WD}| \tag{2.6.10}$$

Turbulence Intensity

Turbulence intensity can be quantified by the turbulent kinetic energy, TKE:

$$TKE = \frac{1}{2}(u'^2 + v'^2 + w'^2) \tag{2.6.11}$$

Gradient Richardson Number

The gradient Richardson number, R_i, is calculated as:

$$R_i = \frac{\frac{g}{T}\frac{\partial \theta}{\partial z}}{(\frac{\partial u}{\partial z})^2 + (\frac{\partial v}{\partial z})^2} \tag{2.6.12}$$

Flux Richardson Number

The flux Richardson number, R_f, is calculated as:

$$R_f = \frac{\frac{g}{T}\overline{w'\theta'}}{\overline{u'w'}\frac{\partial u}{\partial z} + \overline{v'w'}\frac{\partial v}{\partial z}} \tag{2.6.13}$$

Conditional Sampling

Fluxes are conditionally sampled (e.g. Antonia, 1981) to analyse the contribution of along-gradient and cross-gradient fluxes in the flow. An octant analysis is applied with the along slope velocity fluctuations, u', the temperature fluctuations, T', and the vertical velocity fluctuations, w', to evaluate gradient heat transfer by the along-slope momentum stress ($\overline{u'w'}$; Figure 2.13). Octants are simplified into quadrants for a more general analysis of the momentum flux (see Table 2.7, and general quadrants are analysed for the sensible heat flux.

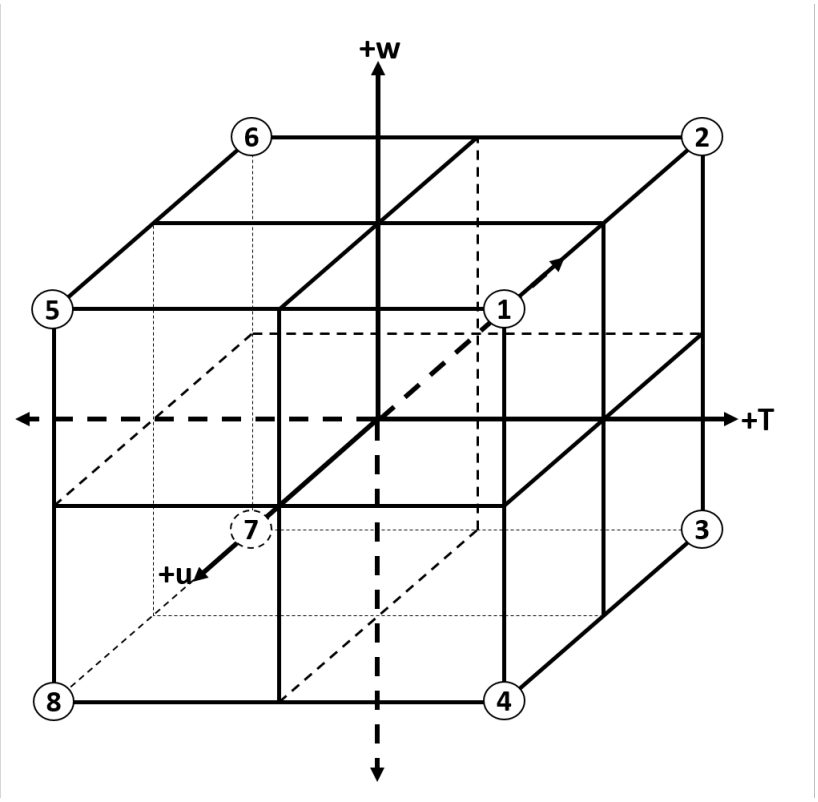

Figure 2.13: Diagram of octants. The numbers identify the octants.

Description	$\overline{u'w'}$	$\overline{w'T'}$
Quadrant 1 (Outward Interaction)	O1 & O5	O1 & O2
Quadrant 2 (Ejection)	O2 & O6	O5 & O6
Quadrant 3 (Inward Interaction)	O3 & O7	O7 & O8
Quadrant 4 (Sweep)	O4 & O8	O3 & O4

Table 2.7: Octants necessary for the calculation of quadrant stress fractions for common quadrant analysis for both the stream-wise vertical momentum flux ($\overline{u'w'}$) and the cross-stream vertical momentum flux ($\overline{w'T'}$).

Given the potential for a change in sign of the various momentum fluxes (which then affects the quadrant analysis), a hyperbolic hole is used to not only investigate the importance of short-lived, large magnitude, events to the bulk transfer of momentum and heat (e.g. Shaw et al., 1983), but to also constrain the analysis to those events that are not associated with the uncertainty in the slope angle measurement (see Appendix 5). The size of the hole, H is defined as:

$$H = \frac{|u'w'|}{|\overline{u'w'}|} \tag{2.6.14}$$

where the point (u',w') lies on the hyperbola bounding the hole region. This hole size changes with every 5 minute block. The hole size necessary to avoid most of the error related to slope angle uncertainties (except for the already very small flux situations, as discussed in Appendix5) is $H = 3$ for the stream-wise and cross-stream vertical stresses, and a hole size $H = 1$ for the horizontal stress (see Figure A2).

Stress fractions, $S_{i,H}$, for both the quadrants and the octants, are defined as:

$$S_{i,H} = \frac{\langle a'w' \rangle}{\overline{a'w'}} \tag{2.6.15}$$

Where the angle brackets ($\langle\ \rangle$) denote a conditional average in this case (not a time ensemble average as otherwise defined), a' is either u', v', or T', i is the octant (or quadrant), and H is the hole size - unless otherwise stated, $H = 3$. The conditional average is the average stress within the quadrant.

To avoid averaging fractions, ensemble averages of the stress fractions are calculated by taking the average of total conditional stresses ($TS_{i,H}$) and the total stresses ($a'w'_{total}$) and then computing stress fractions, where the total conditional stress and the total stress is defined by:

$$TS_{i,H} = \sum_{t=0}^{t=T} a'w'_{i,H}(t) \tag{2.6.16}$$

$$a'w'_{total} = \sum_{t=0}^{t=T} a'w'(t) \tag{2.6.17}$$

Where T is 5 minutes, and a' again represents either u', v', or T'. Time fractions, $TF_{i,H}$ are computed in the same way as the stress fractions, except they represent the fraction of time during the five-minute block interval that the stresses reside in a certain octant/quadrant.

Exchange Efficiency

As a measure of the efficiency of momentum transport, the exuberance, e, of the flow is calculated, which is the ratio of the counter-gradient stress to that of the along-gradient stress (Shaw et al., 1983):

$$e = \frac{S_{1,H} + S_{3,H}}{S_{2,H} + S_{4,H}} \tag{2.6.18}$$

Where $S_{2,H}$ and $S_{4,H}$ are the traditional ejections and sweeps characteristic of gradient transport and $S_{1,H}$ and $S_{4,H}$ are the traditional outward and inward interactions characteristic of counter-gradient transport. When $e = 1$, the transport of high momentum fluid downwards is equally balanced by the transport of high momentum upwards. For $-1 < e < 0$, transport of high momentum fluid downwards dominates.

Measurements of Sweep/Ejection Cycle Imbalance

The skewness in the 3D velocity components, Sk_u, Sk_v, and Sk_w, and acoustic temperatures, Sk_T, are used to elucidate any imbalances in the sweep/ejection cycle. For example, $Sk_u = 0$ and $Sk_w = 0$ would implicate a balance between the contribution of sweeps and ejections to the transfer of momentum.

While Shaw et al. (1983) report ratios of sweeps (traditionally Q4) to ejections (traditionally Q2), we report the ratio of ejections to sweeps as a means of direct comparison with Miller et al. (2017).

Integral Scales

To characterise the length and time scales of the larger turbulent coherent structures, integral length and time scales are calculated (e.g. Shaw et al., 1995). These integral scales represent the largest eddies which are assumed responsible for the bulk of turbulent transfer. Integral scales are calculated by integrating the either

time lagged (for time scale) or distance 'lagged' (for length scale) Eulerian correlation tensor. Correlations for increasing time (τ) or distance (horizontal = r, vertical = d) lags are calculated as:

$$\boldsymbol{R}_a(\boldsymbol{x}, z, t, \boldsymbol{r}, \boldsymbol{d}, \tau) = \frac{\overline{a'(\boldsymbol{x}, t)a'(\boldsymbol{x}+\boldsymbol{r}, \boldsymbol{z}+\boldsymbol{d}, t+\tau)}}{(\overline{a'^2(\boldsymbol{x}, \boldsymbol{z}, , t)}\ \overline{a'^2(\boldsymbol{x}+\boldsymbol{r}, \boldsymbol{z}+\boldsymbol{d}, t+\tau)})^{1/2}} \tag{2.6.19}$$

Where (x, z) is the distance origin, and t is the time origin of the correlation. For time scales, r and $d = 0$, and for length scales, $\tau = 0$. Correlations are fit with an exponential decay function, and then the function is numerically integrated with a distance/time steps of 0.01 m / 0.25 s, respectively. As time and length correlations may not reach zero within the five-minute and 32 m constraints, integration is performed from $R_a = 1$ to $R_a = \frac{1}{e}$. In the case that the correlation does not reach the $e - folding$ distance or time, a scale is not calculated.

The time scales ($\dot{T}$) are known as one-point scales as information from only one sensor is needed, while the length scales ($\ddot{L}$) are two-point as information from two separated sensors is needed. Integral time and length scales are calculated at each TC. Horizontal and vertical length scales are calculated individually, while the combination of horizontal and vertical separation correlations are used to visualise the approximate shape and size of coherent structures in the flow. An average convection velocity, $\overline{uc}$, can then be calculated using:

$$\overline{uc} = \frac{\ddot{L}}{\dot{T}} \tag{2.6.20}$$

3 Results

3.1 Graphical Definitions

For the following results section, box plots represent the ensemble of five-minute averaged measurements or calculations. The notches in the box plots provide the 95% confidence interval for the median, the solid black lines within the boxes represent the median, the outer boundaries of the boxes represent the 25^{th} and 75^{th} percentiles (inter-quartile range), the lower whiskers represent either the minimum of the data or the 25^{th} percentile $-1.5 * IQR$ (whichever is the largest of the two values), and the upper whisker represents either the maximum of the data or the 75^{th} percentile $+1.5 * IQR$ (whichever is the smallest of the two values) (see Figure 3.1). Ensemble averages are represented by solid red lines in the box plots, and asterisks represent the outliers. The translucent green shading in each profile plot represents the approximate location of the 'crown-space' for the vineyard. The translucent grey shading represents the associated measurement error for the represented quantity. All above-ground heights are normalised by the height of the canopy, $h_c = 2.3m$.

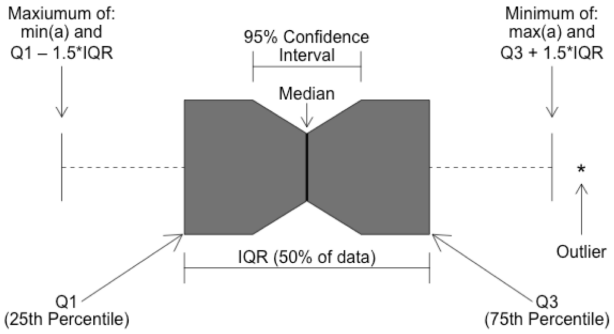

Figure 3.1: Diagram describing the statistics represented by the box plots presented in this study. Q1 represents the 25^{th} percentile, Q2 is the median, Q3 is the 75^{th} percentile, and the IQR is the Inter-Quartile Range, defined as Q3 - Q1. The notches in the box plots represent the 95% confidence interval for the calculated median, and a represents the parameter described by the box plot.

3.2 General Case Overview

Thermal

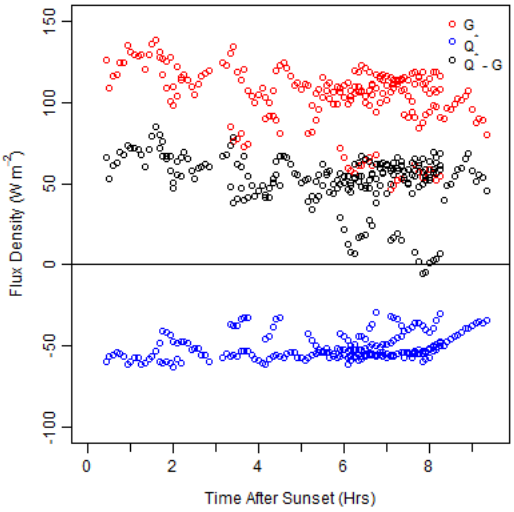

Figure 3.2: Measured and calculated components of the energy balance for the drainage layer as a function of time after sunset (Sunset is approximately 21:05 LST)

Five-minute averaged net radiation, shown in blue, is negative and fairly constant throughout the night. The soil heat flux at the surface, shown in red, is positive, with a slight decrease in magnitude throughout the night. Assuming that the measured net radiation at the top of the domain and the ground heat flux at the bottom of the domain are representative of the whole volume in which measurements are made, $|G| > |Q^*|$ implies an overall positive input of available energy into the measurement domain (in black) through the night, which slightly decreases in magnitude with time (Figure 3.2).

Day	**%Water Content**			
	0 m (Tower)		32 m (up-slope)	
	12 cm	20 cm	12 cm	20 cm
09-07-16	8	4	9	4
10-07-16	7	3	7	3
11-07-16	7	4	6	3
12-07-16	6	2	6	3
13-07-16	8	4	6	2
14-07-16	8	4	6	2
15-07-16	6	3	4	1
17-07-16	5	2	6	2
18-07-16	7	3	4	1
19-07-16	6	3	6	2
20-07-16	6	3	4	1
21-07-16	6	3	5	2
22-07-16	6	3	6	2
Average	**6.6**	**3.2**	**5.8**	**2.2**

Table 3.1: Measured soil volumetric water content at the tower and at 32 m up-slope from the tower (near Mast H).

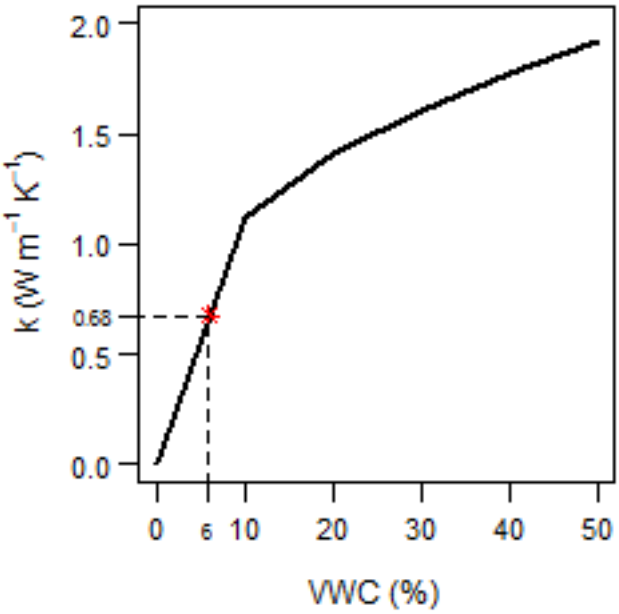

Figure 3.3: Relationship between volumetric water content and the soil thermal conductivity for a mineral soil. Red star indicates value used for soil in study.

Overall, the volumetric water content (VWC) of the soil was consistent throughout the campaign, with the down-slope location being slightly wetter than the up-slope location. The soil closer to the surface is wetter than that deeper in the surface (Table 3.1). Thermal conductivity of the soil, k, is estimated to be around 0.68 W m^{-1} K^{-1}. This estimate is based off of a linear interpolation between the known conductivity at a VWC at 0% and that at 10% (Figure 3.3).

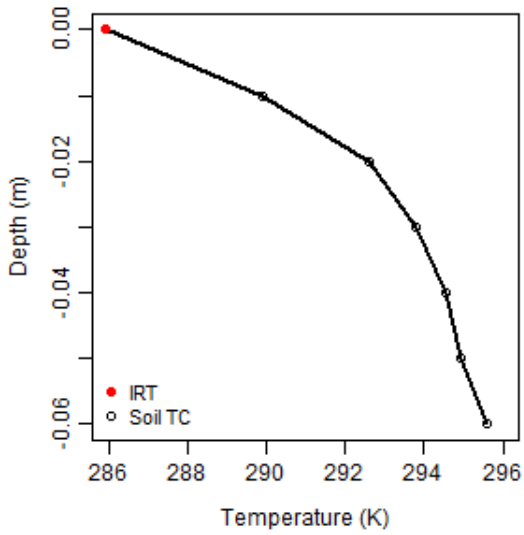

Figure 3.4: Ensemble average of nighttime case study soil temperature with depth. Surface temperature is measured by the IRT (red dot), whereas soil temperatures are measured by extension-grade TCs (black dots).

The soil warms with depth, implicating a movement of heat upwards towards the surface (Figure 3.4). The average soil heat flux, is -87 W m^2, where the negative sign indicates a movement of heat away from the sub-surface and into the atmosphere.

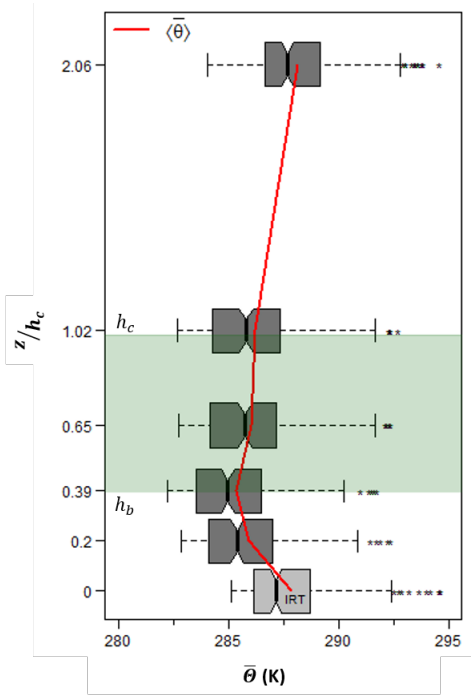

Figure 3.5: Box plots of the 211 five-minute averaged potential temperature profiles as measured by fine-wire TCs (dark-gray) and infrared thermal sensor (light-gray; labelled IRT). For box plot statistics definitions, see Figure 3.1 at the beginning of Section 2.6. The translucent green shading provides approximate location of the vegetated portion of the vineyard canopy at the site; h_c denotes the approximate top of the canopy; h_b denotes the approximate bottom of the vegetated portion of the vineyard canopy. Ensemble average is given by red line.

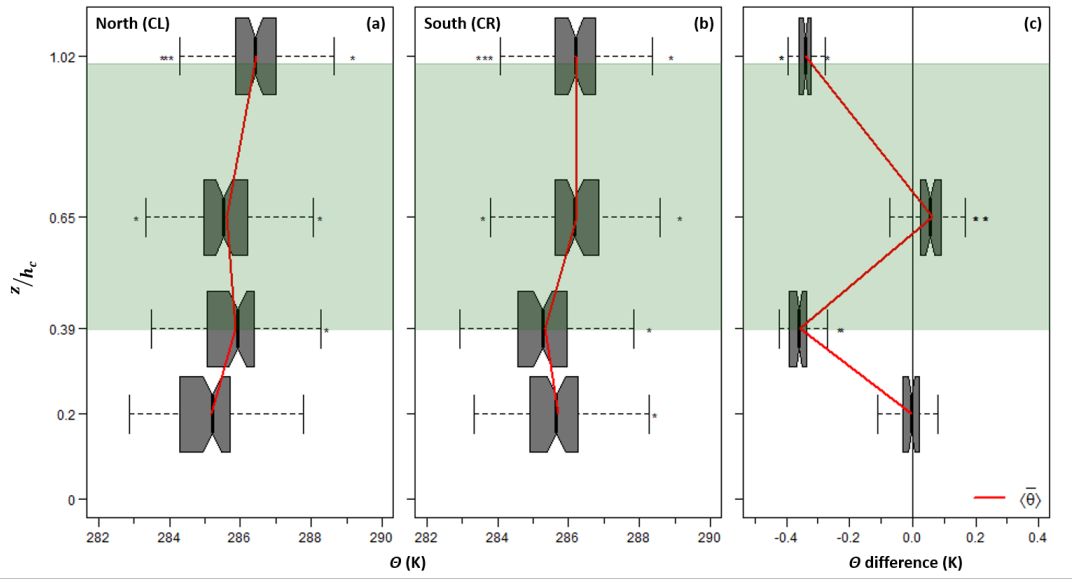

Figure 3.6: Profiles of side wall temperature (north (a) and south (b)) and the average horizontal gradient between the centre of the gap and the vineyard rows (c). Box plot statistical definitions are provided by Figure 3.1 at the beginning of Section 2.6.

An inversion is observed within the 'crown-space' (between $z/h_c = 0.39$ and $z/h_c = 1.02$) of the canopy, whereas a lapse is present in the 'trunk-space' (between $z/h_c = 0$ and $z/h_c = 0.39$; Figure 3.5). The inversion strength between $z/h_c = 0.39$ and $z/h_c = 2.06$ is on average 0.73 K m^{-1}, that between $z/h_c = 0.39$ and $z/h_c = 2.06$ is on average 0.52 K m^{-1}, that between $z/h_c = 0$ and $z/h_c = 2.06$ is 0.059 K m^{-1}, and that between $z/h_c = 0$ and $z/h_c = 0.9$ is -2.77 K m^{-1}, where a positive value indicates an inversion and a negative value indicates a lapse.

Very mild temperature inversions are observed near the vegetation to the north and south of the tower (Masts CN and CS, respectively), but the gradients on each side act in opposite direction. For example, between $z/h_c = 0.39$ and $z/h_c = 0.65$, the near-vegetation air to the north (CN) of the tower is lapsed, while that to the south (CS) is inverted (Figure 3.6(a - b)). These opposing temperature profiles yield unclear horizontal temperature gradients between the vegetation and the gap centre. Figure 3.6(c) provides the average difference between the two vegetation side walls and the centre of the gap. Only near the centre of the canopy ($z/h_c = 0.65$) does the average horizontal temperature gradient indicate a favourable horizontal gradient for heat loss from the canopy.

Mechanical

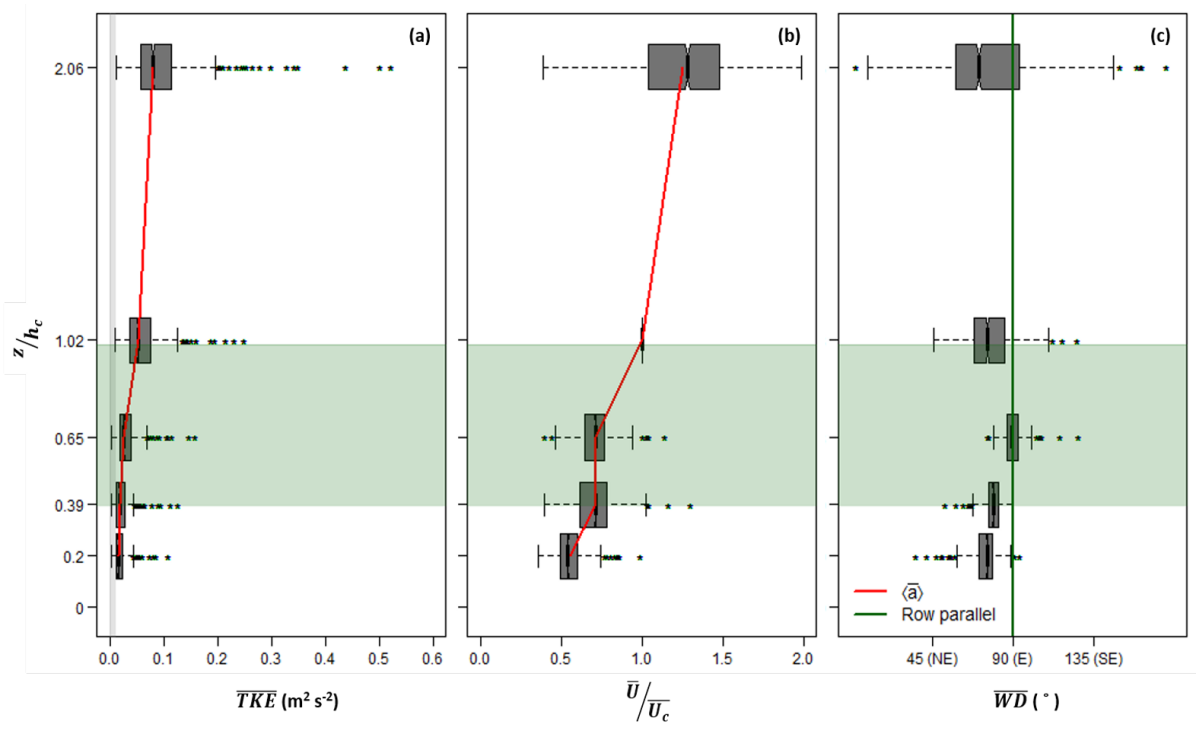

Figure 3.7: Boxplots of the 211 five-minute averaged profiles of turbulent kinetic energy (a), normalised wind speed (b), and wind direction (c). (a) Turbulent kinetic energy (TKE), ensemble average is given by red line; (b) wind speed ($ms^{-}1$) measured by CSAT-3D's normalised by the wind speed at h_c, ensemble average is given by red line; (c) Wind direction ($\overline{WD}$ °) measured by CSAT-3D's, wind coming from the east (90°; down-slope) is given by dark green line. Box plot statistical definitions are provided by Figure 3.1 at the beginning of Section 2.6

TKE is smaller within the canopy than in the above-canopy environment. The vertical gradient of TKE is also relatively small and unchanging between the ground and the centre of the canopy, but steepens near the top of the canopy and in the above-canopy environment (Figure 3.7(a)).

Wind speed increases with height, with an apparent inflection point in the profile near the canopy top (Figure 3.7(b)). The steepest gradients in wind speed are on average between the retarded wind near the surface ($z/h_c = 0.19$) and that at the crown-space bottom ($z/h_c = 0.39$), and between the centre of the crown-space ($z/h_c = 0.65$) and the top of the canopy ($z/h_c = 1.02$). There is no significant gradient in wind speed between $z/h_c = 0.39$ and $z/h_c = 0.65$.

The canopy acts as a channel to the drainage layer. While wind directions aloft have a wider range (note: only $\overline{WD}_{1.02}$ was constrained in the analysis), wind flow is more-or-less parallel to the vineyard rows, especially

deeper within the canopy at $z/h_c = 0.65$ and $z/h_c = 0.39$. Near the surface, the wind directions slightly turn north again out of the canopy alignment (Figure 3.7(c)).

3.3 Fluxes

During 50.7% of the cases, u_* at the canopy top is less that the commonly used threshold of 0.08 m^2 s^{-2}, implicating a low-flux situation for the chosen drainage cases, which is not entirely unexpected given the selection criteria described in section 2.5.2. During the case studies, the median R_i and R_f at the top of the canopy was 0.0402 and 0.1334, respectively, indicating that shear is an important driver in the generation of turbulence, despite the low-flux stably stratified situations.

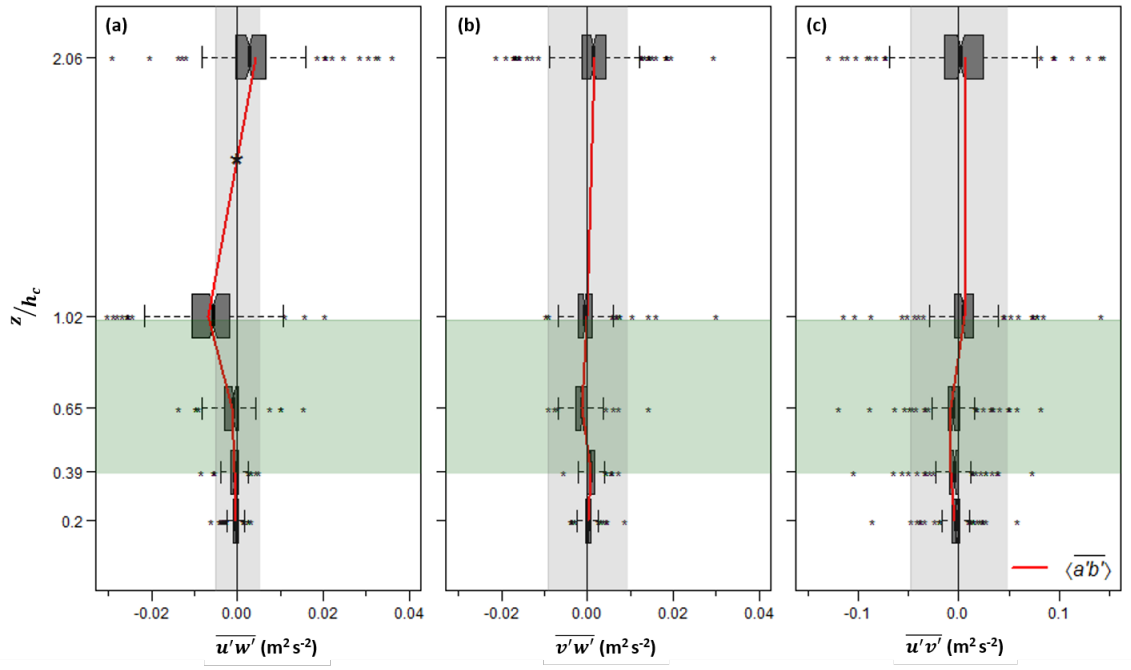

Figure 3.8: Vertical profiles of (a) stream-wise vertical, (b) cross-stream vertical, and (c) cross-vine momentum fluxes. Box plot statistical definitions are provided by Figure 3.1 at the beginning of Section 2.6. Asterisk at $z/h_c = 1.65$ in (a) gives location of interpolated jet-height.

The stream-wise momentum flux ($\overline{u'w'}$) is greater in magnitude than that of the cross-stream momentum flux ($\overline{v'w'}$), except for near the ground where both fluxes are completely within the uncertainty range for the ultrasonic anemometers (Figure 3.8(a - b)). The cross-vine flux ($\overline{u'v'}$) is larger than the vertical momentum fluxes by about an order of magnitude, and is generally negative within the canopy and positive above the canopy (Figure 3.8(c)). While others have briefly considered cross-vine fluxes (Miller et al., 2017), it has been reported to be generally noisy and thus focus is given to the stream-wise momentum flux here.

The maximum flux in the stream-wise momentum is located at the top of the canopy, with the secondary maximum at the top of the measurement domain (Figure 3.8(a)). The stream-wise momentum flux changes sign between the canopy top and the top of the measurement domain, indicating the presence of a jet maximum. With linear interpolation (Grachev et al., 2015), the location is on average at approximately 3.79 m, or $z/h_c = 1.65$, indicated by an asterisk in Figure 3.8(a).

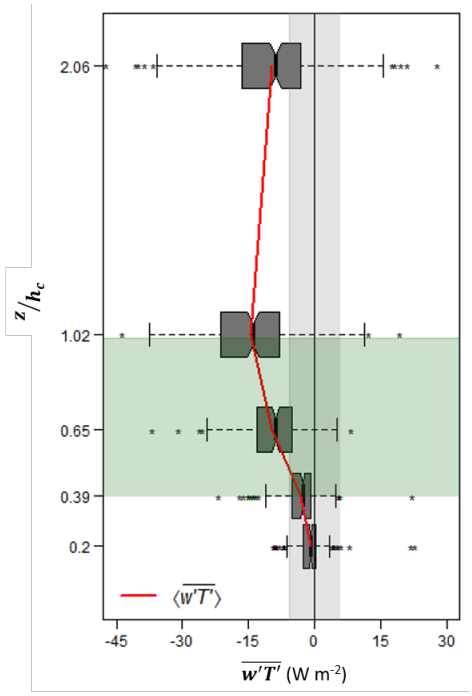

Figure 3.9: Kinematic sensible heat flux with height. Box plot statistical definitions are provided by Figure 3.1 at the beginning of Section 2.6

Heat flux within the inter-quartile range of the five-minute averaged data is everywhere negative (towards surface), with the strongest flux at the top of the canopy (Figure 3.9). Flux in the inter-quartile range at $z/h_c = 0.19$ and $z/h_c = 0.39$ is within the instrument uncertainty bounds for the heat flux, with some outliers indicating both positive and negative heat fluxes during some of the five-minute cases. The location of the maximum heat flux is at the canopy top, which is the same for the along slope momentum flux.

3.3.1 The Flux-Gradient Relationship

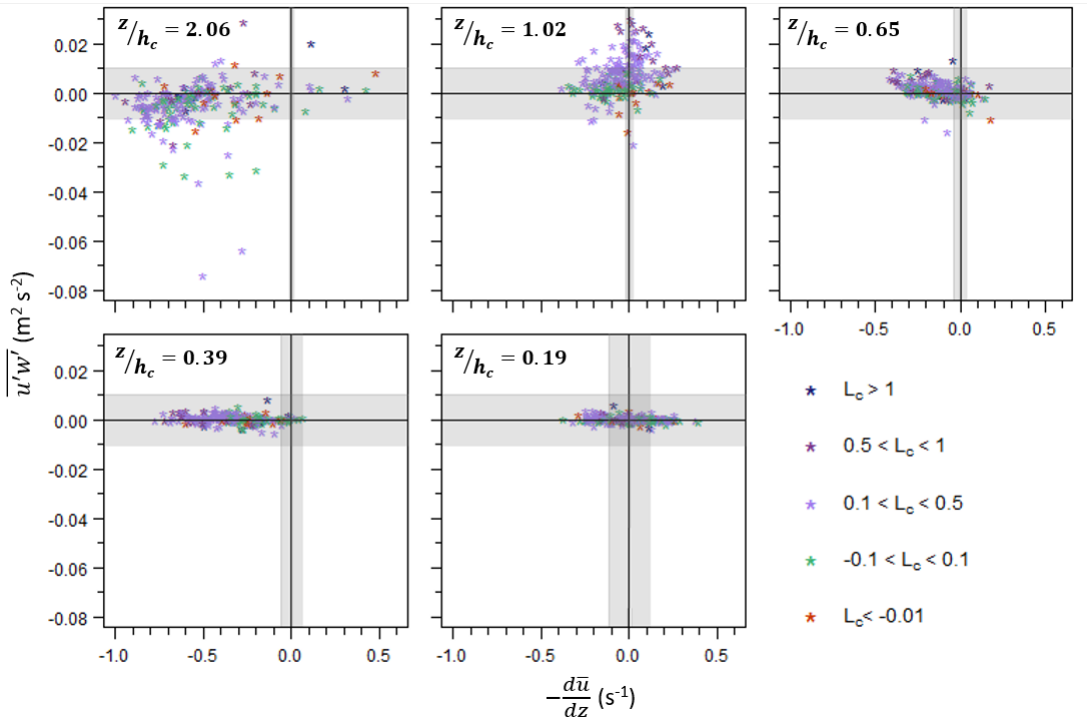

Figure 3.10: Relationship between the vertical gradient in $\overline{u}$-momentum and the vertical flux $\overline{u'w'}$.

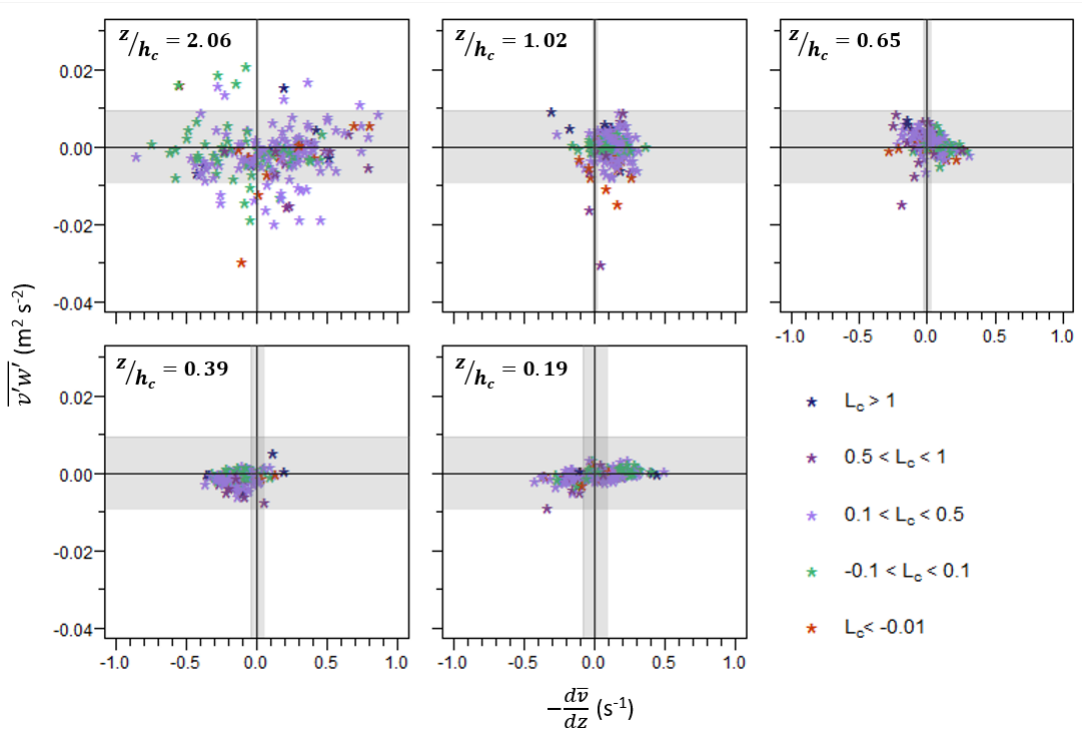

Figure 3.11: Relationship between the vertical gradient in $\overline{v}$-momentum and the vertical flux $\overline{v'w'}$.

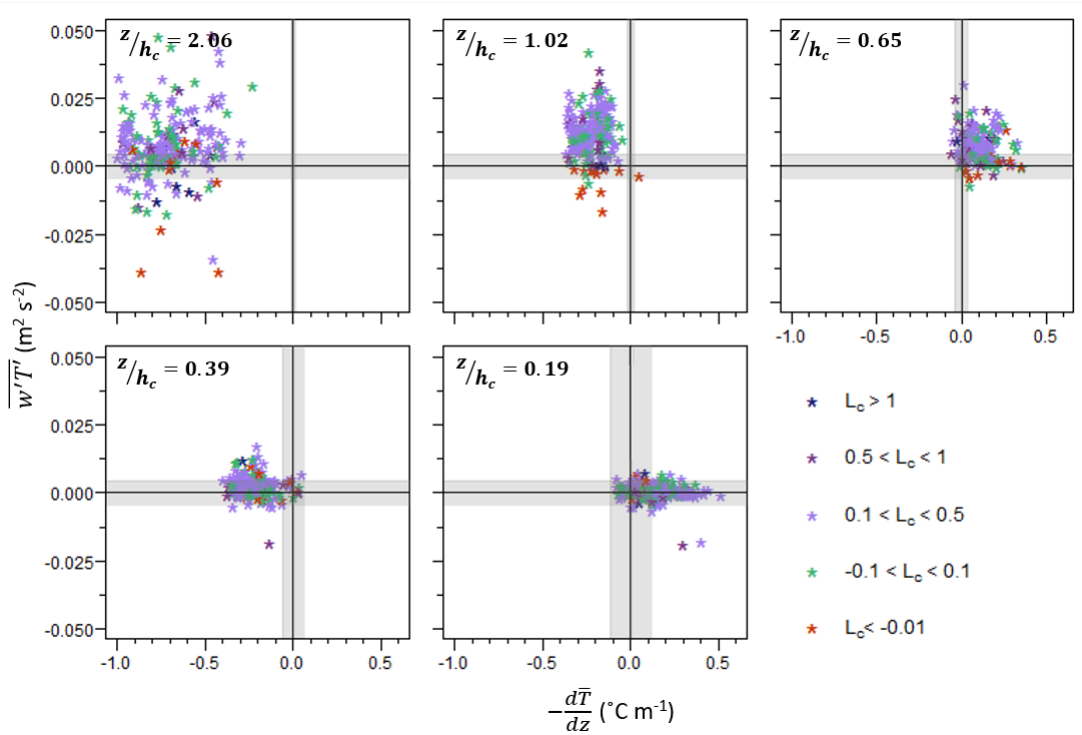

Figure 3.12: Relationship between the vertical gradient in $\overline{T}$ and the vertical heat flux $\overline{w'T'}$.

Figures 3.10 - 3.12 provide the relationship between the vertical gradient in $\overline{u}$, $\overline{v}$, and $\overline{T}$, and the vertical fluxes $\overline{u'w'}$, $\overline{v'w'}$, and $w'T'$, respectively. Quadrants 1 and 3 (upper right-hand corner and lower left-hand corner, respectively) represent gradient fluxes, whereas Quadrants 2 and 4 (upper left-hand corner and lower right-hand corner, respectively) represent counter-gradient fluxes. For the most part, there is no strong relationship between the vertical gradient and the vertical flux for any of the quantities. There does not seem to be any relationship between stability and the correlation between turbulent flux and vertical mean gradient.

3.4 Characterising Exchange

3.4.1 Profile of Third Moments

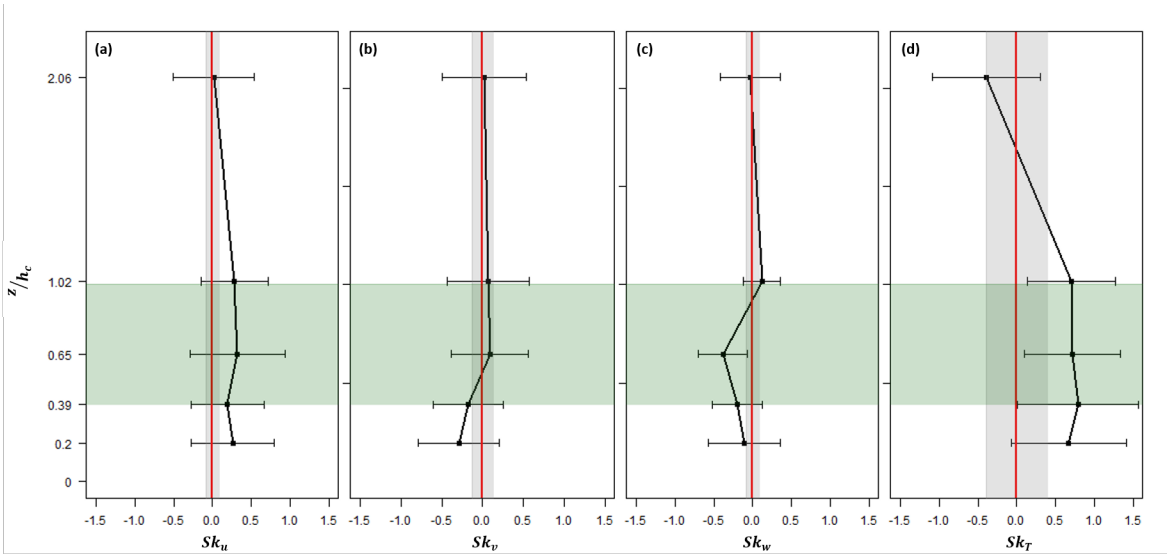

Figure 3.13: Vertical profiles of ensemble averaged skewness in the 5 minute data blocks for all three velocity components and for temperature during the selected case study nights. Error bars represent the standard deviation of the skewness data, and the grey shading represents the uncertainty due to instrumentation errors.

Skewness in the combined horizontal velocity components and temperature, u, v and T, and the vertical components, w, reveals the offset from a joint Gaussian distribution, which is an indication of an unequal contribution of either sweeps or ejections (depending on the sign of the skewness) to the gradient transport of momentum. Within the canopy, u is skewed towards positive values, except for at the top of the array where the average skewness is within the uncertainty bounds (Figure 3.13(a)). Skewness in the cross-stream component, v is very small and within the uncertainty bounds at the top three heights ($z/h_c = 2.06$, 1.02, and 0.65), and is then skewed negatively near the ground (Figure 3.13(b)). Skewness in the vertical component is near zero near at the top of the measurement domain, positive at the canopy top, and then negative within

the canopy (Figure 3.13(c)). Temperature skewness is positive within the canopy and negative at the top of the measurement domain (Figure 3.13(d)).

3.4.2 Connectivity between Heat and Momentum

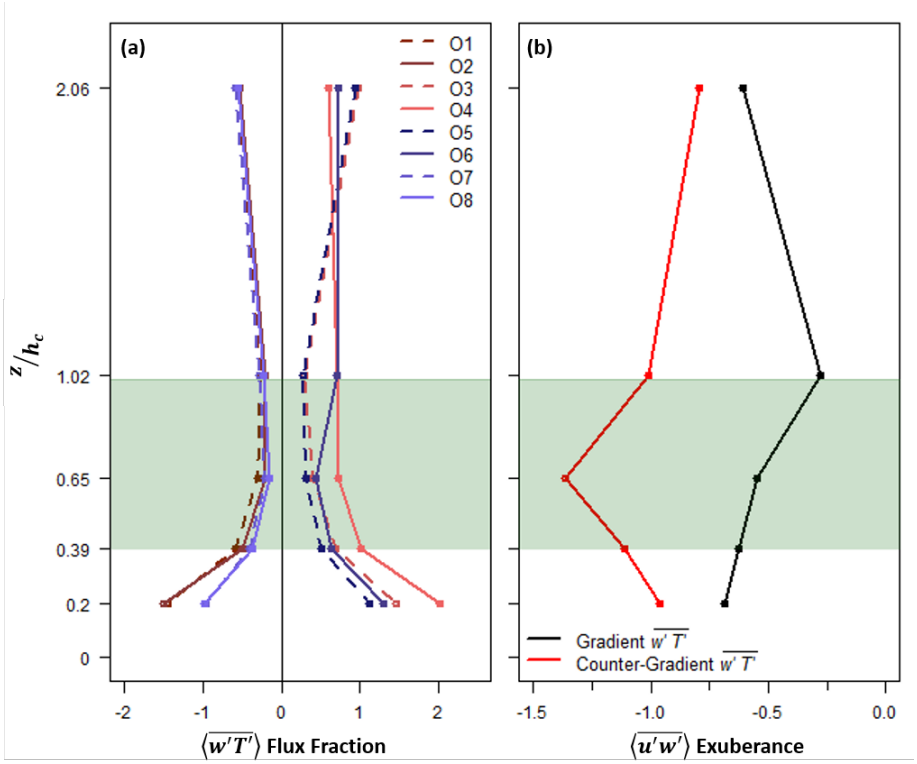

Figure 3.14: (a) Octant heat flux stress fractions. Blue colours are associated with $-T'$ and red colours with $+T'$. Solid lines represent gradient transport of stream-wise momentum, and dashed line represent counter-gradient transport of stream-wise momentum. (b) Separation of the stream-wise momentum flux exuberance into instances of gradient (red) and counter-gradient (black) sensible heat flux.

Figure 3.14(a) provides the ensemble averaged flux fraction for the heat flux as a function of height for each octant. The colouring represents whether or not the octant represents a cooler (blues) parcel or a warmer (reds) parcel. The solid lines represent octants for gradient transport of stream-wise momentum, and the dashed lines represent the counter-gradient transport of stream-wise momentum. Octants 3, 4, 5, and 6 represent gradient transport of heat (warmer air downwards/colder air upwards), and octants 1, 2, 7, and 8 represent counter-gradient transport of heat. At all heights, the gradient transport of heat contributes positively to the heat flux, whereas counter gradient transport contributes negatively, as is expected given the sign of the heat flux at all levels (Figure 3.14(a)). Octants 4 and 6 contribute the most to the flux fraction, which are associated with gradient transport of momentum. Further, octant 4 contributes the most within the canopy to the heat flux, which is associated with sweeps of high momentum and higher temperature

(Figure 3.14(a)).

Figure 3.14(b) provides a breakdown of the stream-wise momentum flux exuberance as a function of heat transport either along the gradient (black) or against the gradient (red). During times of gradient sensible heat transport, the momentum flux is exuberant, and follows closely the overall trend for the total (Figure 3.16(b)). For the instances of counter-gradient sensible heat transport, the momentum flux is not exuberant, indicating that neither sweeps nor ejections dominate the counter-gradient transport of sensible heat (Figure 3.14(b)). In particular, inward and outward interactions (counter-gradient momentum transfer) become more important to the counter-gradient transport of sensible heat near the centre of the canopy, whereas near the canopy-top and the surface, there is no discernible preference towards gradient or counter-gradient momentum transport and the counter-gradient transport of sensible heat (Figure 3.14(b)).

3.4.3 Event Size and Transfer Mechanisms

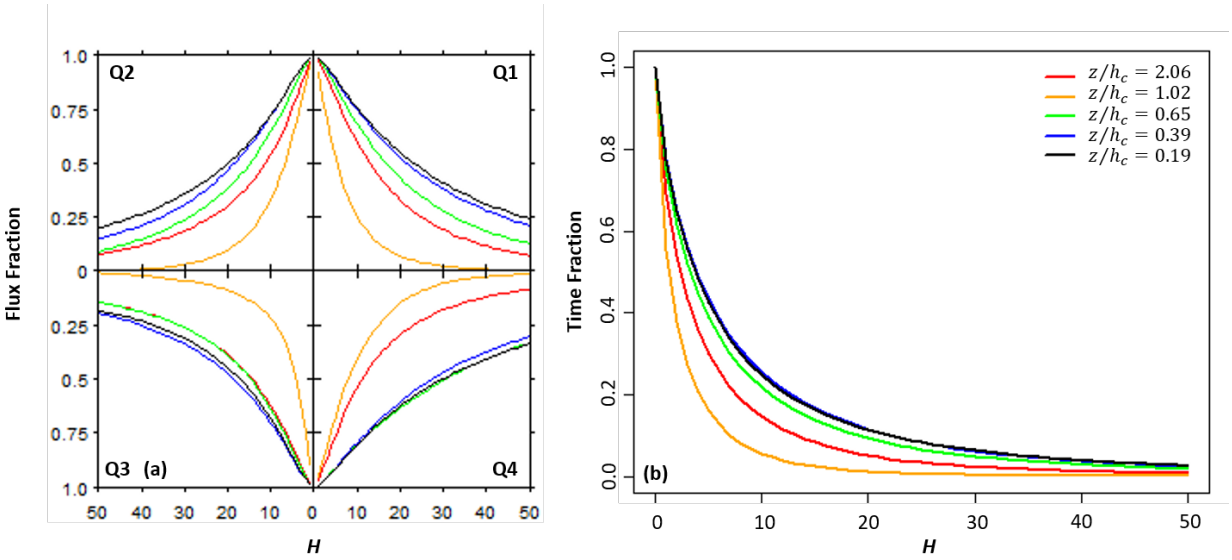

Figure 3.15: $\langle\overline{u'w'}\rangle$ quadrant stress fractions (a) and time fractions (b) as a function of hole size, H

3.15(a) describes the decline in flux contribution as a function of the magnitude of the stream-wise flux event. Quadrants 1 and 3 (upper right and lower left, respectively) represent the contribution due to outward/inward interactions, respectively, and quadrants 2 and 4 (upper left and lower right, respectively) represent the contribution due to ejections and sweeps, respectively. Figure 3.15(b) provides information on the amount of time that the events of a certain size spend contributing to the flux. For example, if a very large event contributed to 20% of the five-minute total flux, but an event of this size or larger only occurred once during the time period, then the time fraction for the event would be $\frac{1}{6000}$, where the denominator

represents the number of measurements made within a five-minute period, and the numerator represents the number of times the flux magnitude is detected within the time period.

As hole size increases, the fraction of stream-wise momentum flux remaining at or above the threshold hole size slowly decays (Figure 3.15(a)). The decay is the slowest for the stream-wise momentum flux near the surface ($z/h_c = 0.19$ and $z/h_c = 0.39$), and quickest at the top of the canopy (Figure 3.15(a)). Instantaneous flux is most frequently small (Figure 3.15(b)), evidenced by the quick decay in the time fractions with increasing hole size. This is particularly true for the momentum flux at the top of the canopy, which is dominated by smaller (relative to the ensemble averaged of the flux at the canopy top) more frequent events. The time fraction decays the slowest for the near-surface measurements (Figure 3.15(b)).

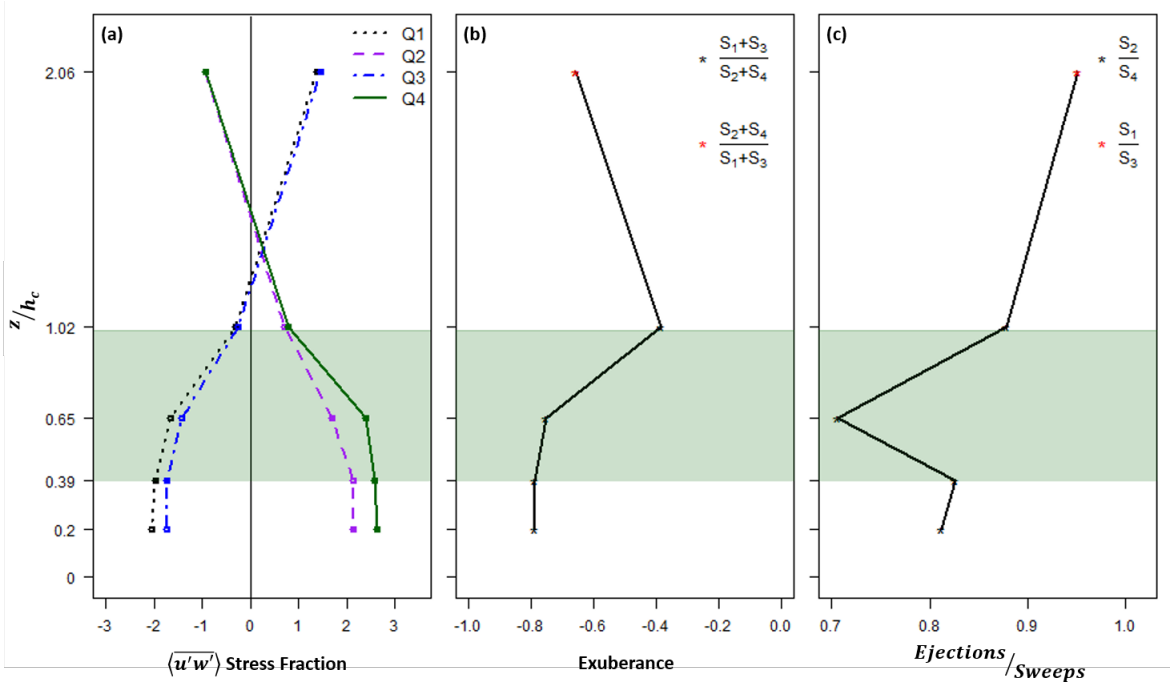

Figure 3.16: (a) $\langle \overline{u'w'} \rangle$ quadrant stress fractions as a function of normalised height for a hole size, $H = 3$; (b) Ensemble averaged exuberance of the $\overline{u'w'}$ flux; (c) the ejection sweep ratio for the $\overline{u'w'}$ flux

Figure 3.16(a) provides the ensemble averaged heat flux fraction for each of the quadrants. Gradient transport is represented by a positive flux fraction, whereas counter gradient transport if represented by a negative flux fraction. There is an apparent regime change between the exchange of momentum within the canopy and that at the top of the measurement domain. Stress fractions for the vertical momentum fluxes are generally smallest in magnitude at the canopy top. Within the canopy, quadrants 2 and 4 contribute the

most to the stream-wise momentum flux, with quadrant 4, which is associated with sweeps, dominating at and below $z/h_c = 0.65$ (Figures 3.16(a).

Figure 3.16(b) provides the exuberance, e as a function of height. Exuberance is used to describe the efficiency of the transfer of high momentum fluid to the surface (Shaw et al., 1983). However, in the present case we adopt a flexible definition of e so that it represents the efficiency of the transport of high momentum fluid downwards below the jet, and high momentum fluid upwards above the jet. When $e = -1$, the transfer of high momentum fluid downwards below the jet (upwards above the jet) is equal to the transfer of low momentum fluid downwards (upwards). When $-1 < e < 0$, the transport of high momentum fluid downwards (upwards) exceeds that of the transport of low momentum fluid downwards (upwards). Exchange of stream-wise momentum is most efficient at the top of the canopy. At and below $z/h_c = 0.65$ and at $z/h_c = 2.06$, the exchange is still efficient, but only slightly (Figure 3.16(b)).

Figure 3.16(c) provides the ratio of ejections to sweeps as a function of height. When this ratio is less than one, sweeps dominate, and vice versa for when it is greater than one. This is inverse to what is given by Shaw et al. (1983). Sweeps are most dominant near the centre of the crown-space ($z/h_c = 0.65$), and remain slightly dominant within and above the canopy (Figure 3.16(c)). The profile of the ejection/sweep ratio found here follows closely that reported by Shaw et al. (1983) for a corn canopy under near-neutral conditions. Miller et al. (2017) found sweeps to dominate over ejections within a vineyard up to $z/h_c = 2.4$ where the ejection/sweep ratio equals 1, which is consistent with our results.

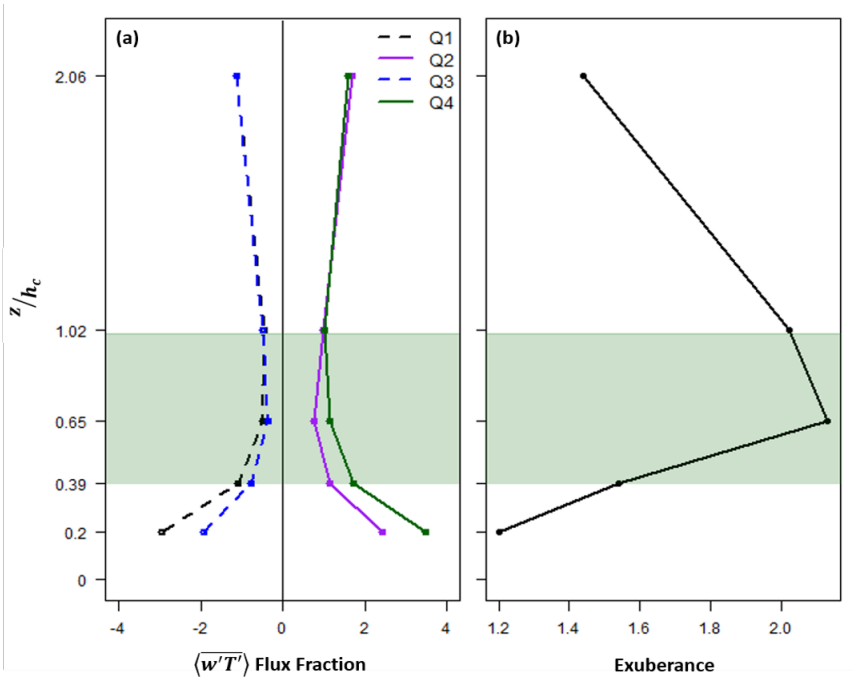

Figure 3.17: Flux fractions (a) and exuberance (b) for the heat flux as a function of height.

Figure 3.17(a - b) is the same as Figure 3.16(a - b), except for the heat flux. There is no change in regime for the heat flux - quadrants 2 and 4 are consistently contributing to the flux across the entire domain (Figure 3.17(a)). Within the canopy, quadrant 4, which is associated with sweeps, contributes the most to the transport of heat. At the canopy top, the contribution of sweeps and ejections is almost exactly the same (Figure 3.17(a)). The flow is most exuberant within the top portion of the canopy (between $z/h_c = 0.65$ and $z/h_c = 1.02$; Figure 3.17(b)).

3.5 Characteristic Turbulent Scales

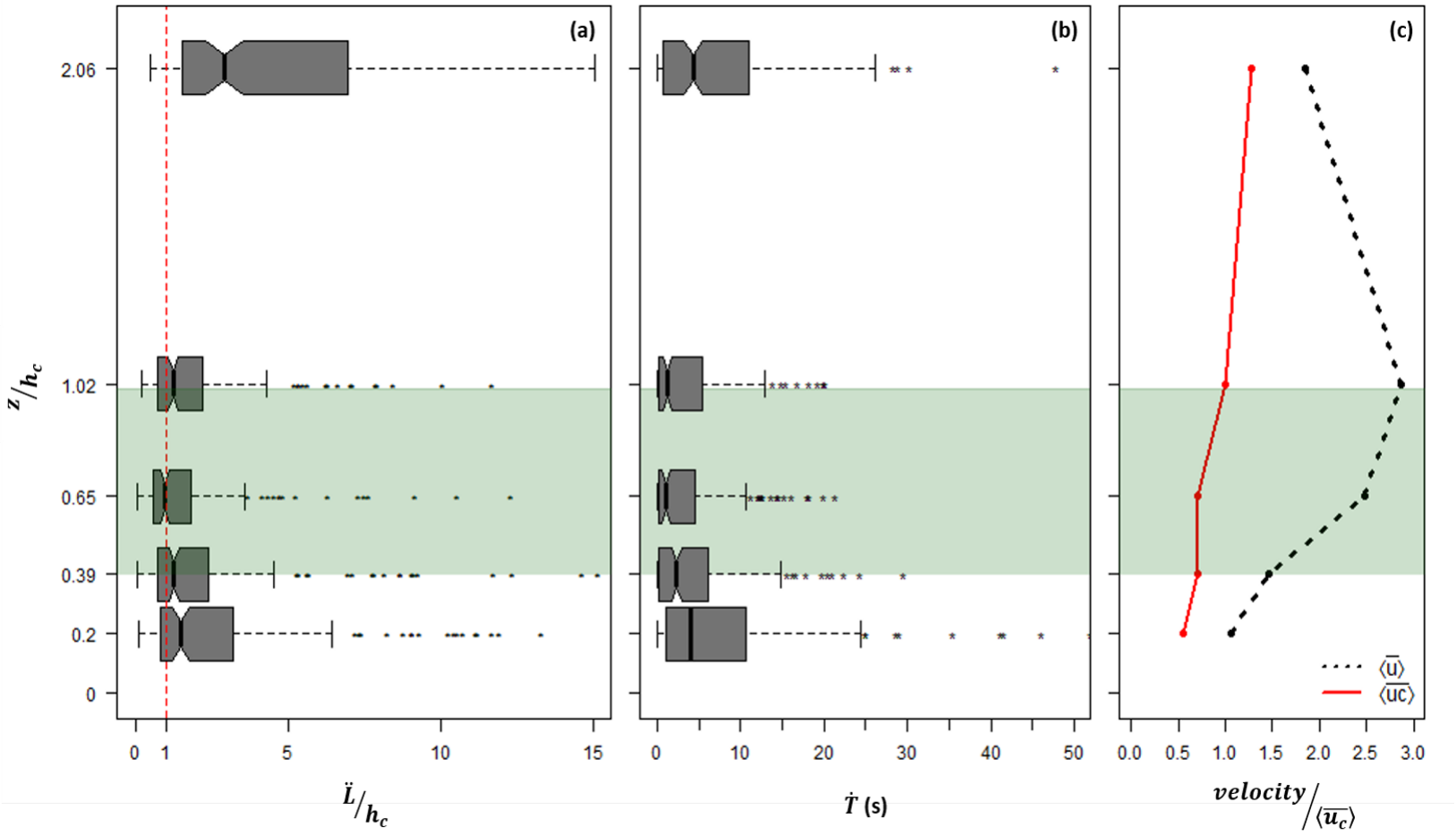

Figure 3.18: Normalised two point length scales (a), time scales (b) and normalised, ensemble averaged, wind speed and convection velocity (c) with height.

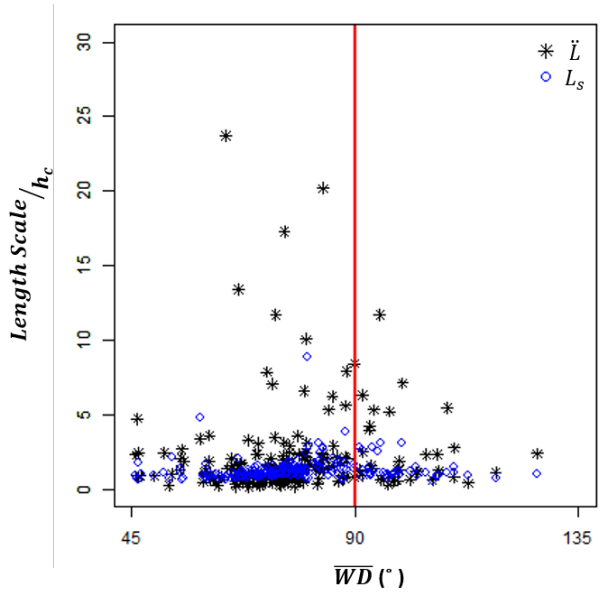

Figure 3.19: Dependence of two point, $\ddot{L}$ and shear, L_s, length scales on the incident wind angle at canopy top. $\overline{WD} = 90°$ corresponds with row-parallel flow.

One-point time scales ($\dot{T}$) are shortest within the canopy, with the longest $\dot{T}$ occurring at the top of the measurement array (Figure 3.18(a)). Two-point length scales ($\ddot{L}$) follow the time scale pattern closely. $\ddot{L}$ scales well with canopy height within the canopy, particularly in the centre of the canopy (Figure 3.18(b)). The behaviour of $\ddot{L}$ and $\dot{T}$ across the entire domain results in quicker convection velocities at the canopy top and within the canopy, and slower convection velocities at the top of the measurement domain and near the surface (Figure 3.18(c)).

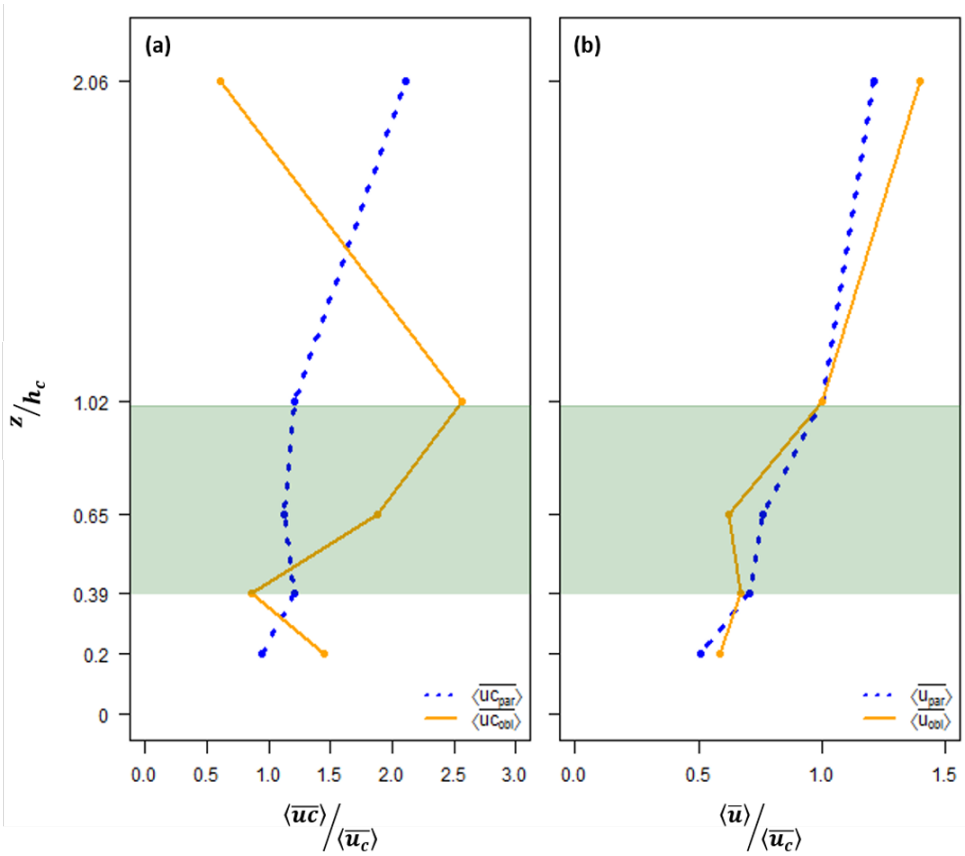

Figure 3.20: Median convection velocity for parallel wind (a; 12 five minute cases) and oblique wind (b; 5 five minute cases) normalised by average canopy top wind speed

When five-minute cases are isolated into strictly parallel cases ($88.5° < \overline{WD} < 92.5°$; 12 total cases) and oblique cases ($\overline{WD} < 47.5°$ or $\overline{WD} > 132.5°$; five total cases), new patterns in the convection velocities arise (Figure 3.20). During the oblique cases, convection velocity ($\langle \overline{uc_{obl}} \rangle$) behaviour with height is very similar to the all-direction case given in Figure 3.18(c). $\langle \overline{uc_{obl}} \rangle$ is greatest at the top of the canopy, and less than the Eulerian velocity at the canopy top under oblique wind conditions ($\langle \overline{u_{obl}} \rangle$) at $z/h_c = 2.06$ and $z/h_c = 0.39$. During the parallel cases, the convection velocities ($\langle \overline{uc_{par}} \rangle$) increase as a function of height, except for within the crown-space of the canopy, where $\langle \overline{uc_{par}} \rangle$ is more or less constant with height (Figure 3.20(a). The Eulerian velocity as a function of height for the strictly parallel cases reveals a weaker inflection point at the canopy top as compared to that for the strictly oblique cases (Figure 3.20(b)).

Figures 3.21 - 3.23 are ensemble averaged contour plots of the spatial temperature correlations for all 211 cases (Figure 3.21), the 12 parallel wind cases (Figure 3.22), and the 5 oblique wind cases (Figure 3.23). Positive distances in the plots indicate a correlation in which the 'stationary' TC is down-slope (x-direction) of, or vertically (z-direction) below, the 'roving sensor'. Therefore, the correlations at Up-slope Distances of

-32 m are between masts A and H, where H contains stationary sensors and A contains the roving sensors. The stationary sensor is located at the (x, z) point (0,0) in the plots. To ensure a common correlation scale, following the ensemble averaging procedure and prior to contour plotting, all negative correlations are re-coded as zero-correlations. This exaggerates the extent of 'no correlation' at the edges of the plotting domains, but allows for inter-comparison between the five different heights.

There is agreement between calculated longitudinal length scales and the size of the eddies in Figure 3.21, whereby the largest structures are located at the top of the measurement domain and the smaller structures are located within the crown-space. According to Figure 3.21, eddies are more circular near the top of the canopy, whereas within the canopy space, the structures are flatter, and near the centre of the crown-space ($z/h_c = 0.65$), are tilted upwards from the surface facing down-slope. During conditions when the wind angle at $z/h_c = 1.02$ is between $90° \pm 2.5°$, structures are more elongated, particularly near the canopy top, and the structures within the canopy are slightly more tilted from slope-parallel (Figure 3.22). During conditions when the wind angle at $z/h_c = 1.02$ is less than $47.5°$ or greater than $132.5°$, structures within the canopy are less elongated, and more correlated in the vertical (Figure 3.23).

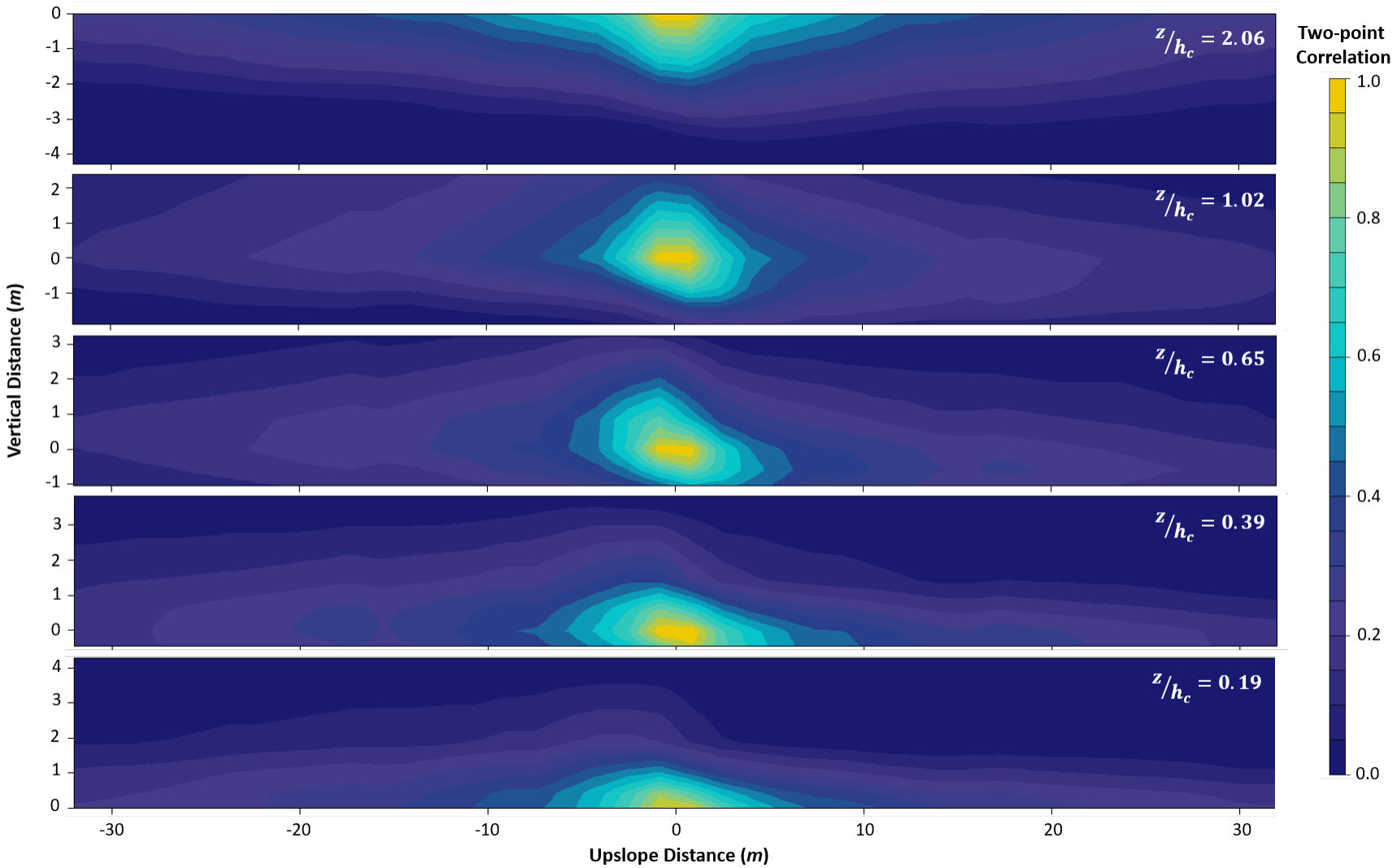

Figure 3.21: (Time) ensemble averaged two-point correlations between all possible TC distance combinations. Correlations made up-slope are positive $x-$distances, and correlations made upwards are positive $z-$distances.

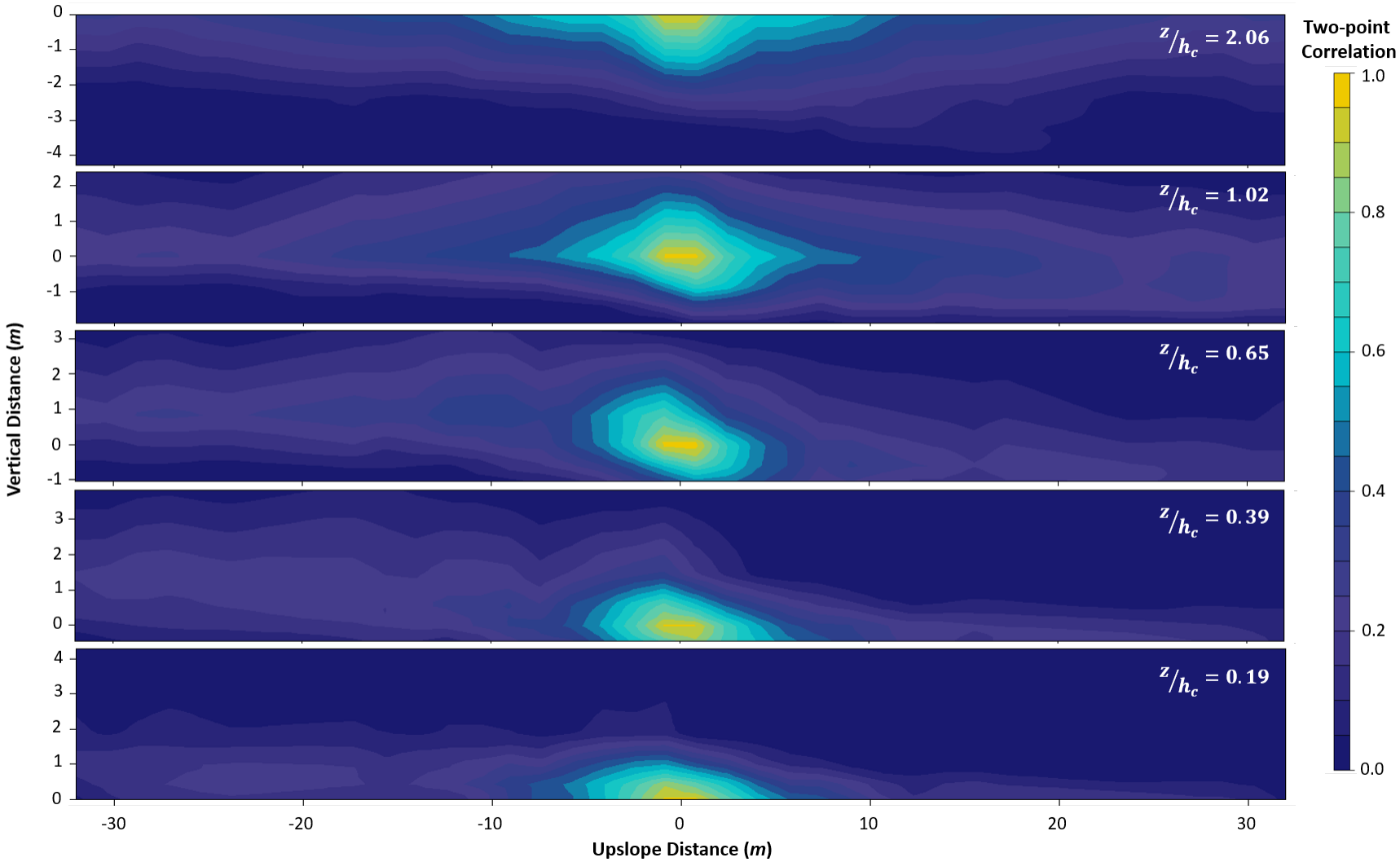

Figure 3.22: (Time) ensemble averaged two-point correlations between all possible TC distance combinations for cases during which the five-minute averaged wind direction was within $90\circ \pm 2.5°$. Distance definitions are provided in Figure 3.21

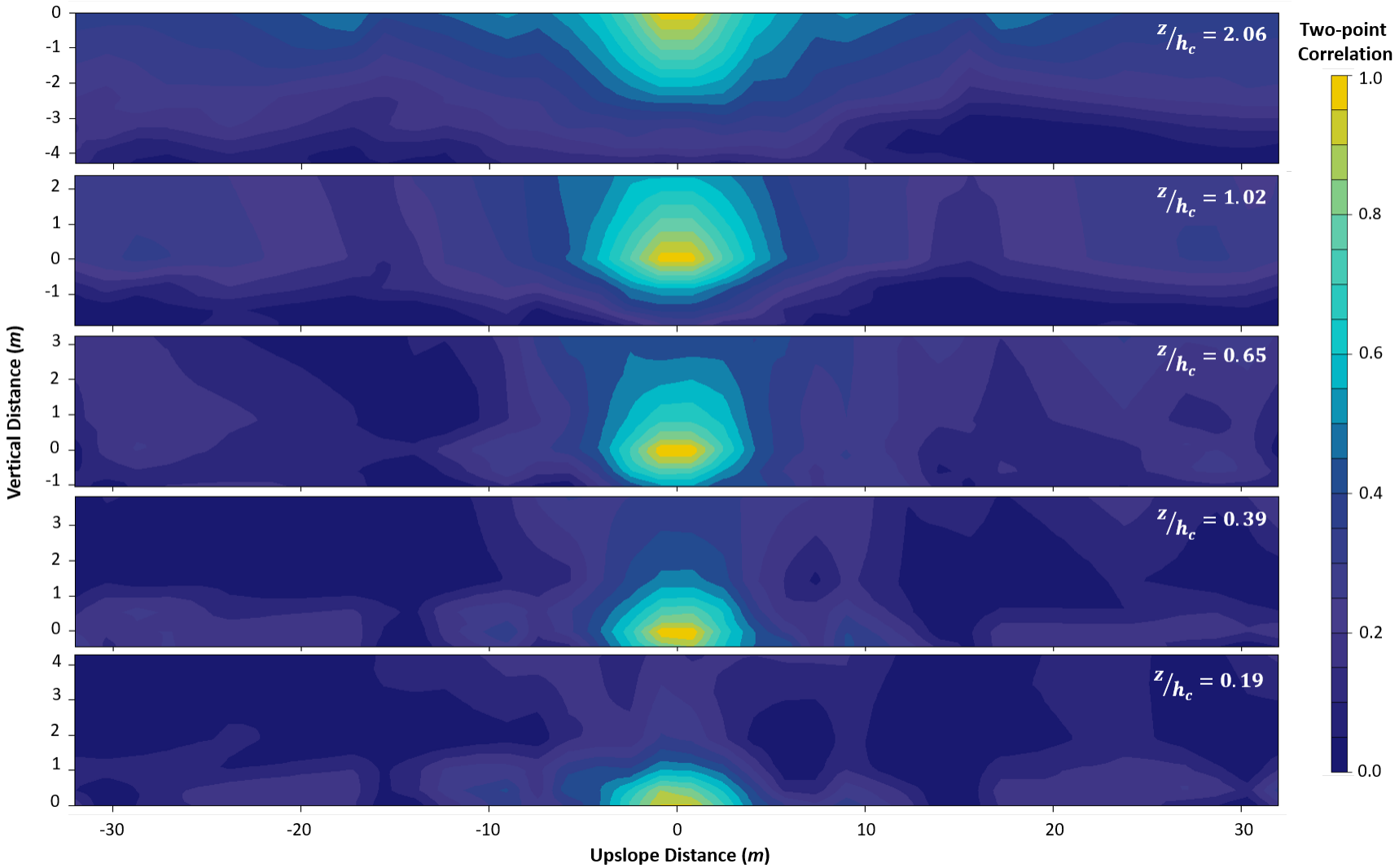

Figure 3.23: (Time) ensemble averaged two-point correlations between all possible TC distance combinations for cases during which the five-minute averaged wind direction was less than 47.5◦ or greater than 132.5°. Distance definitions are provided in Figure 3.21

4 Discussion

4.1 Drainage Flow Characteristics within the Vineyard

4.1.1 Thermal Aspects

Contrary to typical drainage flow over non-vegetated slopes where an inversion is found from the ground up (see Section 1.2.1), the characteristic temperature inversion - which forces the drainage flow - does not start until around $z/h_c = 0.39$ (Figure 3.5). An elevated inversion such as observed here has been observed in other canopies under stable conditions (Jacobs et al., 1994; Dupont and Patton, 2012). However, these canopies were all denser than the present case (*i.e.*, orchard and forest canopies), whereas for more 'open' canopies, strong inversions have been observed in the trunk-space under stable conditions (Launiainen et al., 2007). For the denser canopy cases, a lapse is not entirely surprising in the near-surface region during the nighttime given that the vegetation at the 'crown' can act to prevent out-going long-wave radiation from the surface escaping to the above-canopy environment. Furthermore, it could be expected that under the denser canopy conditions, a fair amount of heat is redirected to the surface from the crown-space of the canopy given that the canopy elements cool throughout the night as well. However, in the present case, the canopy is open (at least in comparison with a forest canopy), the soil is dry, and the skies mostly clear, so it would be expected that cooling from the surface would overcome any small heating due to long-wave radiation from the canopy elements, and that the canopy elements would not act to trap the outgoing long-wave radiation, particularly in the gap region, allowing for an inversion to develop from the ground surface upwards. While the outgoing long-wave radiation is considerable, and great enough to force a drainage flow (e.g. Gudiksen et al., 1992), this loss is overcome by the heat input from the surface (Figure 3.2). Assuming that heat is only exchanged in the vertical, and that our measurements at the top and bottom of the domain are representative for the entire vertical domain, this imbalance would indicate a gradual heating of the air layer around the ultrasonic tower during the nighttime, which is not the case (Figure 3.5). Therefore, it is likely, especially given the presence of drainage (Thomas, 2011), that a non-negligible amount of heat, on the order of $\sim$52 W m^{-2}, is advected out of the domain in the horizontal. While advection is difficult to estimate in canopies (Thomas, 2011), given the flow direction, it is likely that some of this heat is transported down-slope with the drainage layer.

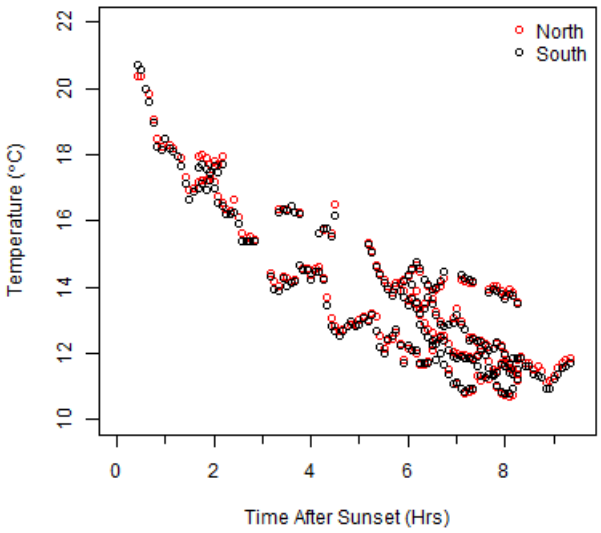

Figure 4.1: Measure surface temperature of vegetation to the north and south sides of the instrumented tower as a function of time since sunset

Given the lapse, it is highly unlikely that the drainage layer itself has been formed locally due to surface cooling. Further, the average temperature profiles near the north and south vegetation sidewalls (masts CN and CS, Figure 2.3) in comparison with those at the centre of the gap (mast C) do not demonstrate favourable horizontal gradients for cooling at the side walls, except for near $z/h_c = 0.65$ (Figure 3.6). However, vegetation surface temperatures do cool throughout the night (Figure 4.1, indicating that, in combination with the horizontal temperature gradients near canopy centre, the canopy could possibly play a role in the formation and sustainment of the nighttime drainage layer. It is likely, given the proximity of the site to steeper slopes to the east and north-east, that the drainage layer is fed both locally and non-locally within the measurement domain. This non-local influence is evidenced further by the predominance of above-canopy flow from the north/north-east (Figure 3.7(c)), suggesting a forcing from the steeper slopes upwind of these directions (see Figures 2.1 and 2.2).

4.1.2 Mechanical Aspects

It is clear, given the weak inflection point near h_c (see Figure 3.7(b)) and the interpolated near-surface jet within the measurement domain (see Figure 3.8(a)), that both dynamics related to drainage and typical CSL flows are present during the case studies. The weak inflection point implies a region of hydrodynamic instability that could lead to the generation of the larger coherent structures known to be responsible for a

large fraction of momentum transfer in canopies (e.g. Finnigan, 2000). At the same time, the presence of the jet acts as a near-surface source of high momentum fluid to feed turbulence within the CSL, despite the stable stratification within the region. How the presence of the inflection point and the near-surface jet in concert influences the character of nighttime exchange is an important question not yet addressed in past studies, and is explored more in the following sections, particularly Section 4.2.

Further complicating the nature of mechanically generated turbulence in the present case is the orientation of the above-canopy wind vectors with respect to the orientation of the canopy, which under favourable conditions (*i.e.*, when $\delta > 0$, Miller et al. (2017)) leads to smaller $\ddot{L}$ (see Figure 4.2). From Figure 3.7(c), it is apparent that shear is added in the presence of drainage within the study site, given that the winds from aloft are consistently forced to flow along the vineyard rows, particularly near $z/h_c = 0.65$. This type of forced turning of the wind vectors was also observed by Miller et al. (2017), who also found that under stable conditions, this effect is increased. This added shear is evidenced by the apparent relationship between an increasing δ and decreasing shear and two-point length scales (L_s and $\ddot{L}$, respectively). The modulation of the turbulent field by δ is explored in more detail in Section 4.3.

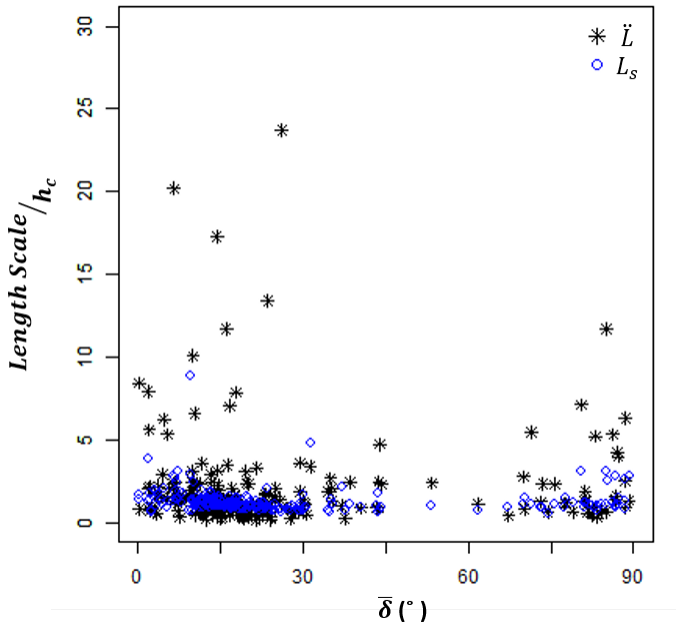

Figure 4.2: Relationship between length scales - shear, L_s, and integral, $\ddot{L}$ - and δ

4.2 Fluxes, Gradients, and their Relationship

4.2.1 Flux-Gradient Relationship

Given that the transfer of both heat and momentum is dominated by larger events, it is unsurprising that K-theory fails to represent the relationship between turbulent correlations and the mean gradients (Figures 3.10-3.12). This failure of gradient transport theory is not unlike other canopies under neutral conditions (Denmead and Bradley, 1987; Finnigan, 2000) due to the predominance of larger structures controlling much of the turbulent flux.

Further, the sensible heat flux, especially near the surface, is dominated by counter-gradient flux, which is not unlike other canopies (Finnigan, 2000). This result, while not new to CSL studies, does hold new implications for future drainage flow models within vineyards, which would be advantageous from a management perspective. Higher-order closure is needed within the canopy (e.g. Wilson and Shaw, 1977), particularly under stable conditions when the likelihood for exchange deeper in the canopy to be dominated by very large, coherent, structures is even higher. This conclusion, of course, must not be taken as absolute. Similarly to Emmel (2014), low-flux situations in the nighttime are related to counter-gradient flux within the canopy, particularly near the surface. While there doesn't seem to be any strong relationship at any height between the the vertical flux and the mean vertical gradients in heat and momentum, the results presented are for the most part within the uncertainty range of the instruments, and could be under-representations of the total flux. Further, because the measured flux is for the most part within the uncertainty range of the instrument, final conclusions on the validity of the flux-gradient relationship within the vineyard canopy under drainage cannot at present be made. Because our ability to measure finer scale structures is limited, our analysis is missing the contribution of flux due to the canopy element-scale (*i.e.*, leaf and stem scale) wake production of turbulence (e.g. Cava and Katul, 2008; Böhm et al., 2013), as well as any dispersive flux (e.g. Poggi and Katul, 2008), and turbulent longitudinal and lateral flux (due to instrumentation set-up).

For the following discussion on the momentum and heat fluxes, the terms 'gradient' and 'counter-gradient' transport are still used to describe the behaviour of the local fluxes, despite the apparent failure of gradient-transport theory. For the most part, the break-down of the fluxes via the quadrant and higher-order statistical moment analyses indicate a slight preference towards gradient transport. Further, these terms are used to describe the 'general' or expected gradients. For example, the transfer of warm air downwards, even in the lapsed near-surface region, is classified as gradient transport. This is because this transfer near the surface is likely due to canopy-top activity, where a negative heat flux is indeed along the gradient. This is done

to make clear the non-local nature of transport, especially near the surface. Additionally, while the terms 'sweeps' and 'ejections' are not classically used to describe modes of heat transport, they are used here for ease of explanation.

4.2.2 Momentum Flux

The change in the sign of the momentum flux between the top of the canopy and the top of the measurement domain indicates the presence of a low-level jet between $z/h_c = 1.02$ and $z/h_c = 2.06$ (e.g. Grachev et al., 2015). The presence of this jet is particularly important to the way that the total exchange between the surface and the outer environment behaves. While high momentum is transferred downwards towards the surface below the jet, high momentum is also transferred upwards away from the jet and the canopy. The transport of the high momentum fluid away from the jet is more efficient below the jet than above it, likely due to canopy acting as a strong momentum sink compared to the above-jet environment which lacks roughness elements to impose drag (Figure 3.16(b)). Because the jet is located above the canopy, and not within it, the classical dominance of sweeps to the transfer of momentum should, and does hold. This predominance of sweeps within the canopy is supported both by the quadrant analysis (Figure 3.16(a and c) and by the sign of Sk_u and Sk_w (Figure 3.13(a and c)). $Sk_u > 0$ and $Sk_w < 0$ indicates a preference towards higher momentum transported downwards. A notable difference between this canopy and others is that the skewness in u- and $w-$components is less than that typically found in canopies under neutral stability (Raupach et al., 1996), indicating that the sweeps occurring are either weaker, and/or not as dominant in comparison. Further, the location of the most negative Sk_w, which has been observed near the canopy top in other studies (Dupont and Patton, 2012; Miller et al., 2017), is here observed near the centre of the canopy. This is supported by the ejection sweep ratio for the momentum flux within the canopy, which reaches a minimum at $z/h_c = 0.65$, indicating that sweeps are the most dominant mode of transfer in this region, compared to the other measured regions in the domain. This is not wholly surprising, and is an indication that the structures generated in the shear-instability region are penetrating downwards into the canopy, despite the inversion, but only to a certain extent perhaps due in part to the inversion. This penetration of turbulence into the canopy decreases as a function of distance from h_c towards the surface, as evidenced by the increase in the ejection-sweep ratio past $z/h_c = 0.65$ (Figure 3.16(c)). The ejection to sweep ratios within the canopy during stable conditions are comparable to those found during near-neutral conditions by Miller et al. (2017) for the row-parallel momentum flux. The average ejection to sweep ratio here is $\sim$0.8, whereas in the neutral case, the average was found to be $\sim$0.7, likely suggesting that during the stable cases, the strength of the mixing layer at canopy top is slightly weaker than that during the near neutral situations, which makes sense given flux magnitudes and velocity inflection strength.

While the stream-wise momentum flux is greatest in magnitude near the canopy top (Figure 3.8(a)), flux in this region is dominated by more frequent, (locally) relatively smaller events (Figures 3.15(a - b)). This, however, does not mean that the events near the top of the canopy are smaller than the ones within the canopy - when hole sizes are calculated, they are based upon a local vertical flux threshold, meaning that a hole size, $H = 4$, at $z/h_c = 1.02$ could be the same size as that of $H = 6$ at $z/h_c = 0.65$. Therefore, the flux at the top of the canopy is dominated by 'smaller', more frequent events, which then penetrate into the canopy and are perceived as much larger events relative to the local average vertical flux.

Indicative of the amount of turning necessary to force the drainage wind along the vineyard rows, cross-stream fluxes ($\overline{v'w'}$) are greatest in magnitude near the centre and bottom of the canopy ($z/h_c = 0.65$ and $z/h_c = 0.39$; Figure 3.8). Interestingly, the average cross-stream flux is negative near the centre of the 'crown space', whereas the cross-stream flux is on average positive at the bottom of the vineyard 'crown space'. Given that these fluxes are calculated under the same rotation, this change in sign indicates that the wind near the surface turns again out of the canopy. Whether this turning near the surface is due to drainage is not a resolvable question, in spite of the wind direction, as the presence of the lapse would suggest the potential for anabatic (or up-slope) flow (e.g. Whiteman, 2000) if the flow situations are topographically influenced as assumed here.

Vexing questions that remain include how the jet affects the communication of canopy sub-layer air with the above-canopy environment, and how the presence of the jet adjusts our definitions of the roughness sub-layer, which is normally defined as at least twice the height of the canopy (Raupach et al., 1996; Finnigan, 2000). By traditional definition, the roughness sub-layer would extend at least up to 4.68 m, which is about 1 m above the interpolated jet height. Under classical drainage wind theory, the above jet and below jet environments are somewhat decoupled, with MOST applying well in the above-jet environment (Horst and Doran, 1988; Grachev et al., 2015), and unknown scaling applying in the below-jet near-surface environment. Both the above-jet and below-jet environments are contained within the present CSL (note that the jet location still calls into question whether or not the CSL truly extends past the jet). Given the additional thermal profile of the current case, the communication between the very near-surface environment, canopy 'crown-space' environment, and the above-canopy environment is complicated. Due to the importance of sweep/ejection motion to the transport of momentum, decoupling is not entirely likely.

4.2.3 Sensible Heat Flux

Of particular interest is the behaviour of the sensible heat flux near the surface. Despite the lapse near the surface, the turbulent heat flux is negative, indicating that heat is still being transported towards the ground despite how warm the ground surface is. The downwards transport of heat is typical for a drainage layer, and is the mechanism by which the near-surface air loses heat. While the near surface air does cool through the night, the lapse persists (Figure 4.3). There are a variety of reasons why the heat flux measurement in the near surface reason could be compromised, however. For one, the measured flux is small and within the uncertainty range of the instrument. Further, spectral flux corrections are not applied, despite being so near to the surface, so it is very likely that flux is in general under-estimated (note that this would not, however, impact the sign of the flux). The eddies that are resolved by the ultrasonic anemometers are fairly large, but there are likely a wide variety of smaller sizes impacting the transport of heat and momentum. With the prospect of large dispersive fluxes (e.g. Poggi and Katul, 2008) and spectral short circuiting limiting the medium-range eddy sizes (e.g. Cava and Katul, 2008), the small eddies unresolved by the anemometers could be contributing largely to the flux, especially near the surface.

Despite the possibility for the flux to be under sampled, and inconclusive in the region, the persistence of the lapse and the cooling throughout the nighttime at a similar rate as the measurement locations within the inversion region (Figure 4.3), makes the lapse further perplexing. As the surface is comparatively warm, and because the soil heat flux is negative (*i.e.*, the surface is losing heat to the air), it would make more sense for the near surface air to be warming - or as discussed earlier, for there to be a significant advective heat flux. The considered advective heat flux in Section 4.1.1 only accounts for the vertical imbalance in the radiative heat loss at the top of the domain and the heat input at the bottom of the domain, and not entirely the additional cooling throughout the night. This additional cooling is indicative of heat loss within the layer near the surface, which could mean either an advective loss larger than the original estimate, could explain in part the negative turbulent kinetic heat flux in the region, and/or could be related directly to the dispersive flux that current anemometry is unable to resolve, but has been shown to be large in sparse canopies (Poggi and Katul, 2008). While there are uncertainties in the ability of the TCs to capture mean temperatures, the uncertainty is very small, and would not change the fact that the air near the surface is cooling throughout the night.

Assuming that the measurements near the surface are at the very least correct in terms of the sign, the downwards turbulent flux near the surface is likely due to a combination of the presence of the drainage

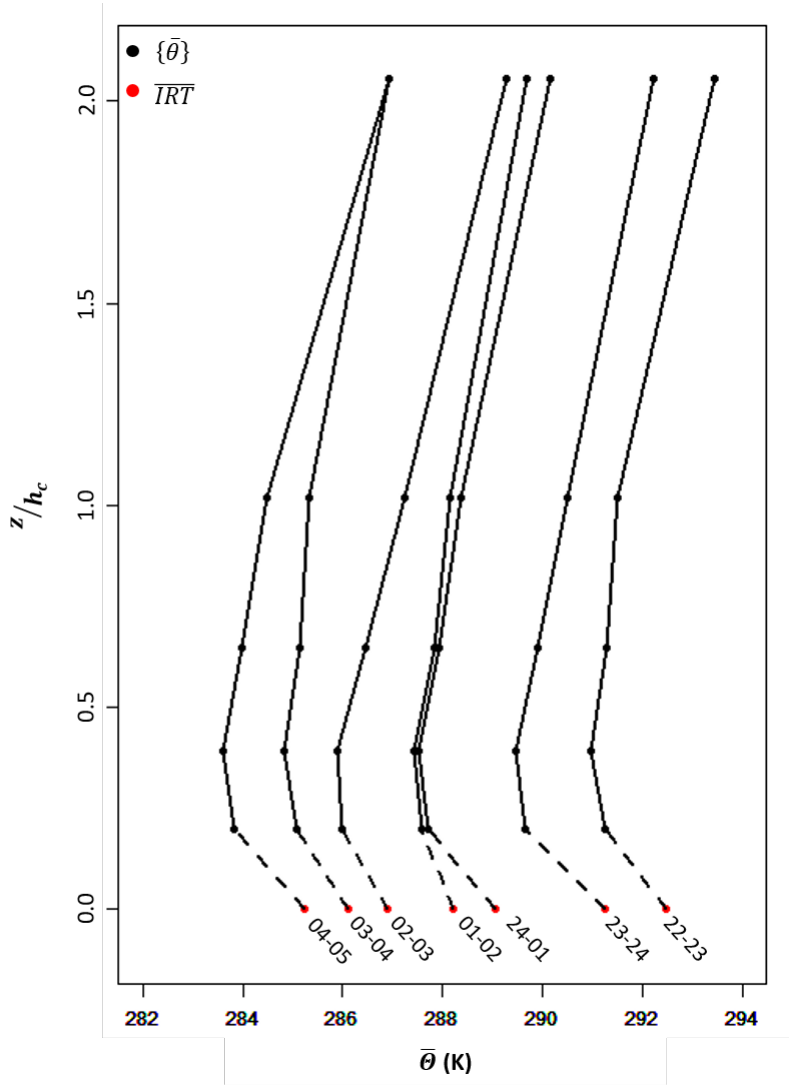

Figure 4.3: Hourly averaged potential temperature profiles through night of 07-06 - 07-07, 2016. Times are displayed in LST for each profile. Over bars in the present plot indicate hourly averages as opposed to five-minute averages.

layer and CSL turbulent dynamics. Consistent with other canopies under near-neutral stability, sweeps and ejections are the most dominant modes of transport for heat in the vineyard (Figure 3.14(a)) (e.g. Finnigan, 2000). Further, sweeps dominate within the canopy, with increasing dominance as the surface is approached 3.14(a)), consistent with behaviour over rough surfaces (Raupach, 1981). The fact that sweeps dominate within the canopy and that the canopy is cooling, further validates the assumption that the negative heat fluxes within the canopy (despite the lapse) are not erroneous measurements (Cava et al., 2006). Further, it is apparent that the gradient transport of heat (*i.e.*, associated with sweeps and ejections, rather than interactions, and along the 'general' inversion gradient) is connected to the gradient transport of momentum (Figure 3.14(b)). This could indicate that the structures sweeping into and out of the canopy retain to some extent their 'original' temperature - where original here does not necessarily mean an absolute origin. Therefore, it is likely that as higher momentum fluid is swept into the canopy, so too is warmer air. If the penetration of structures is deep enough, this warmer air can reach the near-surface region. Despite the near-surface lapse, the average temperatures are still lower than those above the canopy - and even with in the canopy (Figure 3.5) - which would mean a measured negative turbulent heat flux in the region. Interestingly, at the canopy top, the movement of colder air upwards slightly overtakes the movement of warmer air downwards ($\frac{O5+O6}{O3+O4} = 1.06$; Figure 3.14(a)), which further implies the coupling of the movement of heat and momentum in the present case. While the imbalance is very slight, it is in contrast to the within-canopy case where the movement of warm air downwards dominates the heat flux. The fact that ejections overtake sweeps at the top of the domain calls into further question the definition of the CSL when drainage is present.

4.3 Turbulent Scales and Coherent Structures

It is apparent that the movement of coherent structures though the flow is a very important mode of transport within the canopy. Therefore, characterising these structures is a first step towards further understanding the major mechanism behind transport under stably stratified conditions over a vegetated slope. In characterising the scales for coherent structures, it is of important note that our results depend on the quantities we measure. As aptly observed by Finnigan (2000), "coherent structures in canopy flows... are complex patterns of pressure, velocity, and translating air particles and that their presence is manifested in different ways depending upon which variables we choose to measure". Data here allows us to characterise single-point time ($\dot{T}$) and two-point length ($\ddot{L}$) scales using correlations in temperature fluctuations for a 2D transect along the slope, whereas the ultrasonic anemometer tower allows us to investigate time scales. An advantage to the TC array is the circumvention of applying Taylor's frozen hypothesis, which is thought to fail within

canopies (e.g. Thomas, 2011), to describe the structures.

$\ddot{L}$ and $\dot{T}$ are smallest near the canopy top (Figure 3.18), which is in agreement with the apparent inflection point near the top of the canopy. As is the case in the urban environment, where flow channelling and canopy-top shear is important, $\ddot{L}$ increases towards the surface from h_c, and also increases upwards from h_c (Christen et al., 2007). This is a direct effect of the differences in shear intensity as a function of height. $\ddot{L}$ seems to scale well with h_c, but there is a $z-$-dependence that is otherwise not present in 'typical' canopy flows (Finnigan, 2000). The increase of $\ddot{L}$ into the canopy is likely a result of the flow channelling present in the trellised environment. $\ddot{L}$ scales well with the height of the canopy, and $\dot{T}$ profiles follow the same trend as those for $\ddot{L}$.

Of particular interest is the speed at which the structures move through the flow. While median wind speeds reach a maximum outside of the canopy, the convection velocity (uc) - which is the speed at which the coherent structures move - reaches a maximum at the canopy top. This follows along the line of thought that smaller eddies will transverse more quickly through the flow. Contrary to reports from other roughness and canopy sub-layer studies, the ratio of uc to the Eulerian velocity at the height of the canopy (u_c) is not exactly 1.8, rather is almost twice that at the top of the canopy (u_c 2.85 m s^{-1}). The ratio at the top of the measurement domain agrees with other studies, but does not agree within the canopy. The speed at which the structures move through the flow changes with height in the canopy, more-so than $\overline{U}$, which is in contrast to other findings (Finnigan, 2000). The lack of consistency in uc within the canopy could be a consequence of the stability, drainage layer, and structure of the canopy, all of which influence the turbulence in the flow.

4.3.1 Coherent Structure Form

The dual influence of a drainage flow layer and that of the canopy becomes more apparent when investigating the shape of the structures in relation to vertical location. Structures within the canopy are inclined at an angle as would be expected (Shaw et al., 1995), while those at the top of the domain do not seem (visually) to be inclined, and are more elongated in the row-parallel direction (Figure 3.21). Determination of specific inclination angles of the structures is outside of the scope of the study, but is worth further investigation in the future. The elongation along the drainage path is a result of the drainage layer and the lack of roughness elements acting to break up the larger structures - especially in the centre of the gap. The effect of drainage to elongate the structures in the row-parallel direction is more apparent when comparing the structure shapes and sizes between more obliquely-oriented wind directions ($45° < \overline{WD} < 47.5°$ or $132.5° < \overline{WD} < 135°$; Figure 3.23) and row parallel wind directions ($88.5° < \overline{WD} < 92.5°$; Figure 3.22). When the wind is angled

obliquely to the vine rows, coherent structures are smaller, and more circular - the correlation with height and along-slope distance is more similar. Whereas when the wind at the top of the canopy is directed along the vine rows, the structures are flatter and more elongated (*i.e.*, $x > z$), as well as more inclined, especially near the centre of the canopy. In consequence, it is likely that under more parallel drainage (*i.e.*, drainage directed along the rows), the turbulence is more non-local in a horizontal distance sense (turbulence within the canopy is still swept in from at canopy top, and therefore non-local in a vertical sense near the surface), and during more oblique drainage (*i.e.*, drainage from mountains to north-east of site), the turbulence within the canopy is more locally generated in a horizontal sense. While correlations are only made along the row-parallel transect, is can be easily assumed that the structure sizes, at least within the canopy, along the cross-vine direction, are constrained by the vine gap distance ($\sim$3 m).

4.3.2 Structure Scale and Behaviour Dependence on Wind Direction

The canopy orientation is perhaps one of the more important factors in determining the turbulent nature of the flow under drainage conditions. When the wind angle is obliquely oriented in relation to the vineyard canopy, shear and two-point length scales decrease (Figure 4.2), indicating an increase in turbulent activity. The importance of the incident wind angle on CSL turbulence has been explored by Miller et al. (2017), but only for neutral and unstable cases. Even under the stably stratified situations, the canopy architecture is important, and slight deviations from row-parallel flow introduces more turbulence into the canopy. Interestingly, when the wind angle is parallel to the vineyard rows, the median convection velocities within the canopy are very similar to the canopy-top velocity (Figure 3.20), meaning that structures moving within the canopy may be controlled by the Eulerian velocities at canopy top during these situations. If $\overline{uc}$ within the canopy is determined by the Eulerian wind speed at the location of the core of the generated structures (Bailey and Stoll, 2016), then during these row-parallel cases, it can be expected that unstable mode in the flow is indeed near $z/h_c = 1.02$. Under more oblique cases, $\overline{uc}$ within the canopy is much larger than the actual velocity within the canopy (Figure 3.20), which is likely reflecting the fact that during the oblique cases, canopy air is sheltered a bit more from the mean flow, thus yielding lower wind velocities within the canopy (Figure 3.20). During these more oblique wind direction cases, shear is higher, thus the structures are smaller and move quicker along the canopy gap. As the restrictions placed on the wind direction limits oblique cases to 25 minutes of data and the parallel cases to only an hour of data, these results need to be checked against more robust data sets.

4.3.3 Similarity to Plane Mixing Layer Theory

Although it is mentioned throughout earlier discussion, it is worth summarising the similarities between the observed flow through the vineyard, and the plane mixing layer. It is well known that canopy velocity profiles mirror those of plane mixing layers, and that this fact is the reason why coherent structures play such a large role in RSL turbulence (Raupach et al., 1996; Finnigan, 2000). As in the plane mixing layer, velocity profiles for the drainage flow through the vineyard display mild inflection points near the canopy top. This canopy top region is thus also the location of maximum (observed) stream-wise shear stress. While Sk_u does not entirely follow that of a plane mixing layer (where it would be expected that the skew would be zero at the interface between the two fluid layers), Sk_w does follow a trend very similar to that of the plane mixing layer. While the data presented here is of the first to explore drainage through a vineyard canopy in such a way, it is apparent that such flows are a complex combination of the dynamics characteristic of plane mixing layers and that of cold-air drainage.

Perhaps a consequence of this dual canopy mixing-layer and canopy drainage situation is an alteration to the form of the coherent structures, and the way in which they move through the canopy space. For a homogeneous canopy, like a wheat field, coherent rollers develop perpendicular to the stream-wise direction due to Kelvin-Helmholtz instabilities (e.g. Finnigan, 2000; Finnigan et al., 2009). These instabilities arise due to shear at the canopy top, but in the case of a wheat field, the direction from which the wind aloft originates does not affect the generation of these rollers. In the case of the vineyard, 'classical' rollers at the canopy top may be inhibited under certain wind directions. For example, due to drainage, structures are elongated in the stream-wise direction, rather than the cross-stream direction, and are (at least within the canopy) restricted in size along the cross-stream axis, due to the inflexible canopy organisation. While there is still an inflection point visible in the Eulerian velocity profile under vine-parallel conditions (Figure 3.20(b)), the behaviour of the structures is apparently different from typical CSL structures under neutral conditions, and is worth further investigation with methods that are able to resolve structure size in more than just one direction (*i.e.*, large eddy simulations) as is the case here.

5 Conclusions and Outlook

High frequency wind and spatially distributed high frequency temperature measurements were made within a vineyard in the interior of British Columbia to assess turbulent exchange under drainage conditions over and within a vineyard canopy on a slope. Drainage was observed for approximately 17.6 hours during the three-week campaign in July 2016. Typical drainage in the vineyard is associated with a persistent temperature inversion starting around the bottom of the vineyard 'crown-space' (around $z/h_c = 0.39$, where $h_c = 2.3$ m is the canopy height), and a persistent lapse in the near-surface environment. While the near-surface lapse indicates that the drainage flow is not locally generated, there is still the possibility that the flow is buoyantly fed by cooling of the vineyard canopy. The character of the drainage flow is similar to that of both the canopy-plane mixing layer and a drainage layer. A weak inflection point is identified in the velocity profile near the top of the canopy, while a near-surface jet is identified around $z/h_c = 1.65$ using linear interpolation between the stream-wise momentum flux at $z/h_c = 1.02$ and $z/h_c = 2.06$. The duality of the situation influences the transfer of heat and momentum both within and above the canopy.

Turbulence is found to be most intense near the top of the canopy, where the the location of the hydrodynamic instability in the velocity profile is located and where higher momentum fluid swept downwards from the jet interacts with the row-oriented roughness elements. This interaction between the jet and the canopy top is further influenced by the angle of attack of the stream-wise momentum - when canopy-top wind is directed at a more oblique angle to the rows, turbulence length scales decrease. The structures created at the top of the canopy then penetrate into the canopy, increasing the transfer of heat and momentum between the within and above-canopy environments. Turbulent kinetic energy decreases with distance from the top of the canopy as the canopy elements absorb the momentum of the structures generated at the top of the canopy, but perhaps not to the same extent as in a denser, more homogeneous canopy. This is apparent in the vertical flux profiles within and above the canopy. Unique to drainage cases within vegetation, high momentum is additionally transported upwards away from the canopy due to the jet, calling into question the extent of canopy influence on the above-canopy environment during drainage conditions, in addition to application of traditional definitions of the CSL.

It is found that while the turbulent exchange of heat and momentum do not follow basic K-theory, precluding the estimation of a turbulent Prandtl number, both heat and momentum appear to be transported together during the larger coherent events responsible for the failure of K-theory. These larger events occur infrequently, but contribute to most of the transfer of momentum. As is expected for canopy flow, the

transfer of the stream-wise momentum is exuberant, with the most efficient transfer occurring at the canopy top. Sweeps dominate everywhere, but are particularly important at the centre of the canopy, likely due to proximity to the top of the canopy where the coherent structures are generated. Another unique feature of the drainage layer is the change in definition of the classical quadrants, necessitating careful consideration of transfer mechanisms during drainage conditions within the canopy.

Coherent structure visualisation via 2D temperature correlations indicate that the structures dominating the transfer of heat are elongated in the stream-wise direction. In particular, the structures are most elongated under row-parallel conditions, corresponding with more local drainage, when the flow at the centre of the gaps interacts the least with the vegetated side-walls. During the parallel wind-angle attacks, when drainage is assumed to be more locally feds, horizontal transfer of turbulence is more non-local. During the oblique wind-angle attacks, when drainage is assumed to be more non-locally fed, the structures generated are more vertically coherent, and more circular. During this non-local drainage, the transport of turbulence is more horizontally local.

Current data does not allow for absolute conclusions to be made for over 50% of the time due to inadequate u_* values (less than the typical threshold of 0.08 $m^2\ s^{-2}$). Furthermore, most of the measured and calculated values from ultrasonic anemometer data is within the instrument uncertainty limits. Because the situations investigated here are during expected (and observed) low-flux and weak turbulent activity, this instrumentation issue is unavoidable at present. The characterization of the cases as 'low-flux' situations is made based on what is observable by the ultrasonic anemometers. It is recognised that the current anemometry is unable to capture the very small scale turbulent wakes produced by the canopy elements, and that within the canopy, the conversion from lower frequency turbulence to frequencies outside the detection range of the ultrasonic anemometers, deemed spectral short-circuiting, is likely occurring (e.g. Finnigan, 2000; Cava and Katul, 2008), thus further lending to an underestimation of the total flux. To fully resolve the stably stratified drainage canopy situation within the vineyard, instruments with the ability to capture much smaller scale fluxes are necessary. We are also at present unable to resolve the origin of the drainage layer.

It is worth noting that the quadrant analysis employed here tends to underestimate the contributions due to ejections. It is well known that sweeps in the canopy tend to be larger, more infrequent events, whereas ejections tend to be smaller, more frequent events (e.g. Thomas and Foken, 2007*a*). Due to the use of the hyperbolic hole method, we are knowingly excluding a number of smaller ejection events. However, as these fluxes are very small, and do not lend an incredible amount to the total flux, conclusions made on total flux

contributions are not affected. Further, the quadrant analysis does not represent the spatial or temporal scales of the transporting eddies, making it difficult to conclusively link the transport of heat and momentum with the passing of the coherent structures with the described scales. To do this, a wavelet based conditional sampling method, like that described in Thomas and Foken (2007*a*) could be employed.

Despite the instrumentation limitations, future work can still be done on the current data set. A thorough investigating into the advective heat flux is possible, given the TC array, and would help to resolve unanswered questions about the abnormal near-surface thermal character of the flow. The use of a wavelet based analysis to characterise the turbulent length and time scales would be advantageous - particularly in determining the validity of the use of integral scales to describe eddy length and time scales. Wavelet based methods have been used successfully in other canopy studies as objective event detection methods (Brunet and Irvine, 2000; Salmond et al., 2005; Christen et al., 2007), which would allow for the additional calculation of event frequency and stream-wise eddy separation, and would allow for a more detailed investigation on the fluxes associated with particular coherent events. Calculation of the spectra would allow for additional identification of dominant scales within the flow, but would not be necessary if a wavelet based approach were to be taken.

Knowledge on the mean and turbulent character of drainage conditions within the sloped vineyard environment is important not only to current efforts to completely understand nighttime surface fluxes, but also to the furtherance of viticulture. For example, in the present vineyard, heat is advected down-slope, which is of importance to not only the health of the BOV vines, but also to the vineyards at the bottom of the slope within the Okanagan Valley which may depend on the advected energy to prevent frost damage. Furthermore, in the case of heat advection, there is the possibility that energy is wasted while running the inversion-preventing wind mill devices found in the Okanagan.

References

Amanatidis, G., Papadopoulos, K., Bartzis, J. and Helmis, C. (1992), 'Evidence of katabatic flows deduced from a 84 m meteorological tower in Athens, Greece', *Boundary-Layer Meteor.* **58**, 117–132.

Antonia, R. A. (1981), 'Conditional sampling in turbulence measurement', *Annu. Rev. Fluid Mech.* **13**, 131–156.

Aubinet, M. (2008), 'Eddy covariance co_2 flux measurements in nocturnal conditions: An analysis of the problem', *Ecological Appl.* **18**(6), 1368–1378.

Aubinet, M., Heinesch, B. and Yernaux, M. (2003), 'Horizontal and vertical co_2 advection in a sloping forest', *Boundary-Layer Meteor.* **108**, 397–417.

Bailey, B. N. and Stoll, R. (2013), 'Turbulence in sparse, organized vegetative canopies: a large-eddy simulation study', *Boundary-Layer Meteor.* **147**(3), 369–400.

Bailey, B. N. and Stoll, R. (2016), 'The creation and evolution of coherent structures in plant canopy flows and their role in turbulent transport', *Journal of Fluid Mechanics* **789**, 425–460.

Bailey, B. N., Stoll, R., Pardyjak, E. R. and Mahaffee, W. F. (2014), 'Effect of vegetative canopy architecture on vertical transport of massless particles', *Atmospheric environment* **95**, 480–489.

Ball, F. K. (1956), 'The theory of strong katabatic winds', *Aus. J. Phys.* **9**, 373–386.

Banta, R. and Gannon, P. T. (1995), 'Influence of soil moisture on simulations of katabatic flow', *Theoret. Appl. Clim.* **52**, 85–94.

Belcher, S., Finnigan, J. and Harman, I. (2008), 'Flows through forest canopies in complex terrain', *Ecological Appl.* **18**(6), 1436–1453.

Böhm, M., Finnigan, J. J., Raupach, M. R. and Hughes, D. (2013), 'Turbulence structure within and above a canopy of bluff elements', *Boundary-layer meteorology* pp. 1–27.

Bowen, P., Bogdanoff, C., Estergaard, B., Marsh, S., Usher, K., Smith, C. and Frank, G. (2005), 'Geology and wine 10: Use of geographic information system technology to assess viticulture performance in the okanagan and similkameen valleys, british columbia', *Geoscience Canada* **32**(4).

Brunet, Y. and Irvine, M. R. (2000), 'The control of coherent eddies in vegetation canopies: Streamwise structure spacing, canopy shear scale and atmospheric stability', *Boundary-Layer Meteor.* **94**, 139–163.

Burns, P. and Chemel, C. (2015), 'Interactions between downslope flows and a developing cold-air pool', *Boundary-Layer Meteorol.* **154**, 57–80.

Cava, D. and Katul, G. G. (2008), 'Spectral short-circuiting and wake production within the canopy trunk space of an alpine hardwood forest', *Boundary-Layer Meteorology* **126**(3), 415–431.

Cava, D., Katul, G. G., Scrimieri, A., Poggi, D., Cescatti, A. and Giostra, U. (2006), 'Buoyancy and the sensible heat flux budget within dense canopies', *Boundary-Layer Meteorology* **118**(1), 217–240.

Cellier, P. and Brunet, Y. (1992), 'Flux-gradient relationships above tall plant canopies', *Agricultural and Forest Meteorology* **58**(1-2), 93–117.

Chahine, A., Dupont, S., Sinfort, C. and Brunet, Y. (2014), 'Wind-flow dynamics over a vineyard', *Boundary-Layer Meteor.* **151**, 557–577.

Chemel, C. and Burns, P. (2015), 'Pollutant dispersion in a developing valley cold-air pool', *Boundary-Layer Meteorol.* **154**, 391–408.

Christen, A., van Gorsel, E. and Vogt, R. (2007), 'Coherent structures in urban roughness sublayer turbulence', *Int. J. Climatol.* **27**, 1955–1968.

Collineau, S. and Brunet, Y. (1993), 'Detection of turbulent coherent motions in a forest canopy part i: Wavelet analysis', *Boundary-Layer Meteorology* **65**(4), 357–379.

Denmead, O. T. and Bradley, E. F. (1987), 'On scalar transport in plant canopies', *Irrigation Science* **8**(2), 131–149.

Devito, A. and Miller, D. (1983), 'Some effects of corn and oak forest canopies on cold air drainage', *Agricult. Meteorol.* **29**, 39–55.

Dupont, S. and Patton, E. G. (2012), 'Influence of stability and seasonal canopy changes on micrometeorology within and above an orchard canopy: The CHATS experiment', *Agric. For. Meteor.* **157**, 11 – 29.

Emmel, C. (2014), Vertical distribution of carbon dioxide, water vapour, momentum and energy exchange within and above a forest stand affected by the mountain pine beetle, PhD thesis, University of British Columbia.

Finnigan, J. (2000), 'Turbulence in plant canopies', *Annual review of fluid mechanics* **32**(1), 519–571.

Finnigan, J. and Belcher, S. (2004), 'Flow over a hill covered with a plant canopy', *Quarterly Journal of the Royal Meteorological Society* **130**(596), 1–29.

Finnigan, J. J., Shaw, R. H. and Patton, E. G. (2009), 'Turbulence structure above a vegetation canopy', *Journal of Fluid Mechanics* **637**, 387–424.

Francone, C., Katul, G., Cassardo, C. and Richiardone, R. (2012), 'Turbulent transport efficiency and the ejection-sweep motion for momentum and heat on sloping terrain covered with vineyards', *Agric. For. Meteor.* **162-163**, 98–107.

Froelich, N., Grimmond, C. and Schmid, H. (2011), 'Nocturnal cooling below a forest canopy: Model and evaluation', *Agric. For. Meteor.* **151**, 957–968.

Froelich, N. and Schmid, H. (2006), 'Flow divergence and density flows above and below a deciduous forest. Part II. Below-canopy thermotopographic flows', *Agric. For. Meteor.* **138**, 29–43.

Gao, W., Shaw, R. et al. (1989), 'Observation of organized structure in turbulent flow within and above a forest canopy', *Boundary-Layer Meteorology* **47**(1-4), 349–377.

Garrett, A. (1983), 'Drainage flow prediction with a one-dimensional model including canopy, soil and radiation parameterizations', *J. Clim. Appl.Meteorol.* **22**, 79–91.

Gash, J. H. C. (1986), 'Observations of turbulence downwind of a forest-heath interface', *Boundary-Layer Meteorology* **36**(3), 227–237.

Geiss, A. and Mahrt, L. (2015), 'Decomposition of spatial structure of nocturnal flow over gentle terrain', *Boundary-Layer Meteorol.* **156**, 337–357.

Grachev, A. A., Leo, L. S., Sabatino, S. D., Fernando, H. J. S., Pardyjak, E. R. and Fairall, C. W. (2015), 'Structure of turbulence in katabatic flows below and above the wind- speed maximum', *Boundary-Layer Meteorol.* .

Grisogono, B., Jurlina, T., Večenaj, Z. and Guttler, I. (2015), 'Weakly nonlinear prandtl model for simple slope flows', *Q.J.R. Meteorol. Soc.* **141**, 883–892.

Gross, G. (1987), 'Some effects of deforestation on nocturnal drainage flow and local climate – a numerical study', *Boundary-Layer Meteorol.* **38**, 315–337.

Grudzielanek, A. and Cermak, J. (2015), 'Capturing cold-air flow using thermal imaging', *Boundary-Layer Meteorol.* **157**, 321–332.

Gudiksen, P., Leone Jr, J., King, C., Ruffieux, D. and Neff, W. (1992), 'Measurements and modeling of the effects of ambient meteorology on nocturnal drainage flows', *Journal of Applied Meteorology* **31**(9), 1023–1032.

Haiden, T. and Whiteman, C. D. (2005), 'Katabatic flow mechanisms on a low-angle slope', *J. Appl. Meteorol.* **44**, 113–126.

Heinesch, B., Yernaux, M. and Aubinet, M. (2007), 'Some methodological questions concerning advection measurements: a case study', *Boundary-Layer Meteorol.* **122**, 457–478.

Horst, T. and Doran, J. (1986), 'Nocturnal drainage flow on simple slopes', *Boundary-Layer Meteorol.* **34**, 263–286.

Horst, T. W. and Doran, J. C. (1988), 'The turbulence structure of nocturnal slope flow', *J. Atmos. Sci.* **45**(4), 605–616.

Irvine, M. R., Gardiner, B. A. and Hill, M. K. (1997), 'The evolution of turbulence across a forest edge', *Boundary-Layer Meteorology* **84**(3), 467–496.

Jacobs, A. F. G., Van Boxel, J. H. and El-Kilani, R. M. M. (1994), 'Nighttime free convection characteristics within a plant canopy', *Boundary-Layer Meteorology* **71**(4), 375–391.

Katul, G. G., Cava, D., Siqueira, M. and Poggi, D. (2013), 'Scalar turbulence within the canopy sublayer', *Coherent flow structures at Earth's Surface* pp. 73–95.

Komatsu, H., Yoshida, N., Takizawa, H., Kosaka, I., Tantasirin, C. and Suzuki, M. (2003), 'Seasonal trend in the occurrence of nocturnal drainage flow on a forested slope under a tropical monsoon climate', *Boundary Layer Meteorol.* **106**, 573–592.

Launiainen, S., Vesala, T., Mölder, M., Mammarella, I., Smolander, S., Rannik, Ü., Kolari, P., Hari, P., Lindroth, A. and Katul, G. G. (2007), 'Vertical variability and effect of stability on turbulence characteristics down to the floor of a pine forest', *Tellus B* **59**(5), 919–936.

Leclerc, M. Y., Beissner, K. C., Shaw, R. H., Hartog, G. D. and Neumann, H. H. (1990), 'The influence of atmospheric stability on the budgets of the Reynolds stress and turbulent kinetic energy within and above a deciduous forest', *J. Appl. Meteor.* **29**, 916–933.

Lee, X., Finnigan, J. and Paw U, K. (2005), 'Coordinate systems and flux bias error', *Handbook of Micrometeorology* pp. 33–66.

Lee, Y.-H. and Mahrt, L. (2005), 'Effect of stability on mixing in open canopies', *Agric. For. Meteor.* **135**, 169–179.

Liss, K., Leitch, A. and Christen, A. (2009), Sonic anemometer field inter-comparison, internal report, Technical report, The University of British Columbia.

Mahrt, L. (2010), 'Computing turbulent fluxes near the surface: Needed improvements', *Agric. For. Meteor.* **150**, 501–509.

Mahrt, L. (2014), 'Stably stratified atmospheric boundary layers', *Annu. Rev. Fluid Mech.* **46**, 23–45.

Mahrt, L., Lee, X., Black, A., Neumann, H. and Staebler, R. (2000), 'Nocturnal mixing in a forest subcanopy', *Agric. For. Meteor.* **101**, 67–78.

Mahrt, L. and Lee, Y.-H. (2005), 'Effect of stability on mixing in open canopies', *Agric. For. Meteor.* **135**, 169–179.

Manins, P. and Sawford, B. (1979), 'Katabatic winds: A field case study', *Q.J.R Meteorol. Soc.* **105**, 1011–1025.

Miller, N. E., Stoll, R., Mahaffee, W. F., Neill, T. M. and Pardyjak, E. R. (2015), 'An experimental study of momentum and heavy particle transport in a trellised agricultural canopy', *Agric. For. Meteor.* **211**, 100–114.

Miller, N. E., Stoll, R., Mahaffee, W. F. and Pardyjak, E. R. (2017), 'Mean and turbulent flow statistics in a trellised agricultural canopy', *Boundary-Layer Meteorology* pp. 1–31.

Mo, R. (2013), 'On adding thermodynamic damping mechanisms to refine two classical models of katabatic winds', *J. Atmos. Sci.* **70**, 2325–2334.

Moroni, M., Giorgilli, M. and Cenedese, A. (2014), 'Experimental investigation of slope flows via image analysis techniques', *J. Atmos. Solar-Terrestrial Phys.* **108**, 17–33.

Oke, T. R., Mills, G., Christen, A. and Voogt, J. A. (2017), *Urban climates*, Cambridge: Cambridge University Press.

Oldroyd, H., Katul, G., Pardyjak, E. and Parlange, M. (2014), 'Momentum balance of katabatic flow on steep slopes covered with short vegetation', *Geophys. Res. Lett.* **41**, 4761–4768.

Papadopoulos, K., Helmis, C., Soilemes, A., Kalogiros, J., Papageorgas, P. and Asimakopoulos, D. (1997), 'The structure of katabatic flows down a simple slope', *Q. J. R. Meteorol. Soc.* **123**, 1581–1601.

Paw U, K. T., Brunet, Y., Collineau, S., Shaw, R. H., Maitani, T., Qiu, J. and Hipps, L. (1992), 'On coherent structures in turbulence above and within agricultural plant canopies', *Agricultural and Forest Meteorology* **61**(1), 55 – 68.

Poggi, D. and Katul, G. (2007), 'The ejection-sweep cycle over bare and forested gentle hills: a laboratory experiment', *Boundary-Layer Meteor.* **122**, 493–515.

Poggi, D. and Katul, G. G. (2008), 'Micro- and macro-dispersive fluxes in canopy flows', *Acta Geophysica* **56**(3), 778–799.

Poggi, D., Porporato, A., Ridolfi, L., Albertson, J. and Katul, G. (2004), 'The effect of vegetation density on canopy sub-layer turbulence', *Boundary-Layer Meteor.* **111**(3), 565–587.

Poulos, G. and Zhong, S. (2008), 'An observational history of small-scale katabatic winds in mid-latitudes', *Geography Compass* **2**(6), 1798–1821.

Pypker, T., Unsworth, M., Lamb, B., Allwine, E., Edburg, S., Sulzman, E., Mix, A. and Bond, B. (2007), 'Cold air drainage in a forested valley: Investigating the feasibility of monitoring ecosystem metabolism', *Agricult. Forest Meteorol.* **145**, 149–166.

Raupach, M. (1981), 'Conditional statistics of reynolds stress in rough-wall and smooth-wall turbulent boundary layers', *Journal of Fluid Mechanics* **108**, 363–382.

Raupach, M. R., Finnigan, J. J. and Brunet, Y. (1996), *Coherent Eddies and Turbulence in Vegetation Canopies: The Mixing-Layer Analogy*, Springer Netherlands, Dordrecht, pp. 351–382.

Rebman, C., Zeri, M., Lasslop, G., Mun, M., Kolle, O., Schulze, E. and Feigenwinter, C. (2010), 'Treatment and assessment of the CO2-exchange at a complex forest site in Thuringia, Germany', *Agric. For. Meteor.* **150**, 684–691.

Salmond, J., Oke, T. R., Grimmond, C., Roberts, S. and Offerle, B. (2005), 'Venting of heat and carbon dioxide from urban canyons at night', *Journal of Applied Meteorology* **44**(8), 1180–1194.

Shaw, R., Brunet, Y., Finnigan, J. and Raupach, M. (1995), 'A wind tunnel study of air flow in waving wheat: two-point velocity statistics', *Boundary-Layer Meteor.* **76**, 349–376.

Shaw, R., Tavangar, J. and Ward, D. (1983), 'Structure of the Reynolds Stress in a Canopy Layer', *J. Clim. Appl. Meteor.* **22**, 1922–1931.

Staebler, R. M. and Fitzjarrald, D. R. (2005), 'Measuring canopy structure and the kinematics of subcanopy flows in two forests', *J. Appl. Meteorol.* **44**, 161–179.

Stull, R. B. (1988), *An Introduction to Boundary Layer Meteorology*, Vol. 13, Springer Science Business Media.

Sturman, A., McGowan, H. and Spronken-Smith, R. (1999), 'Mesoscale and local scale climates', *Progress Phys. Geog.* **23**, 611–635.

Sun, H., Clark, T., Stull, R. and Black, T. (2006), 'Two-dimensional simulation of airflow and carbon dioxide transport over a forested mountain. part i: Interactions between thermally-forced circulations', *Agricult. Forest Meteorol.* **140**, 338–351.

Thomas, C. (2011), 'Variability of sub-canopy flow, temperature, and horizontal advection in moderately complex terrain', *Boundary-Layer Meteor.* **139**, 61–81.

Thomas, C. and Foken, T. (2007*a*), 'Flux contribution of coherent structures and its implications for the exchange of energy and matter in a tall spruce canopy', *Boundary-Layer Meteorology* **123**(2), 317–337.

Thomas, C. and Foken, T. (2007*b*), 'Organised motion in a tall spruce canopy: temporal scales, structure spacing and terrain effects', *Boundary-Layer Meteorology* **122**(1), 123–147.

Thomas, C., Kennedy, A., Selker, J., Moretti, A., Schroth, M., Smoot, A., Tufillaro, N. and Zeeman, M. (2012), 'High-resolution fibre-optic temperature sensing: A new tool to study the two-dimensional structure of atmospheric surface-layer flow', *Boundary-Layer Meteor.* **142**, 177–192.

Turnipseed, A., Anderson, D., Blanken, P., Baugh, W. and Monson, R. (2003), 'Airflows and turbulent flux measurements in mountainous terrain. part 1. canopy and local effects', *Agricul. Forest Meteorol.* **119**, 1–12.

Whiteman, C. D. (2000), *Mountain Meteorology*, Oxford University Press, Oxford, UK.

Wilson, N. R. and Shaw, R. H. (1977), 'A higher order closure model for canopy flow', *Journal of Applied Meteorology* **16**(11), 1197–1205.

Yi, C., Monson, R. K., Zhai, Z., Anderson, D. E., Lamb, B., Allwine, G., Turnipseed, A. A. and Burns, S. P. (2005), 'Modeling and measuring the nocturnal drainage flow in a high-elevation, subalpine forest with complex terrain', *J. Geophys. Res.* **110**.

Zardi, D. and Whiteman, C. D. (2013), *Mountain Weather Research and Forecasting: Recent Progress and Current Challenges*, Springer Netherlands, Dordrecht, chapter Diurnal Mountain Wind Systems, pp. 35–119.

Appendices

Appendix A: CSAT-3D Rotation Sensitivity and Error Analysis

Choice of slope rotation was partially informed by the slope measurement in the field, and the inclination angle of the streamlines at a 90° wind direction at all of the heights (Figure A1). It is expected that air will flow most parallel to the local terrain slope at the lowest point of measurement and at the top of the vegetation, where the vineyard rows mimic the sloping ground. Inclined wind angles at these locations ($z/h_c = 0.19$ and $z/h_c = 1.02$) agree well with the measured slope angle, and thus a value of 7° is used as the final rotation angle for the second rotation into the plane (see Section 2.4.1).

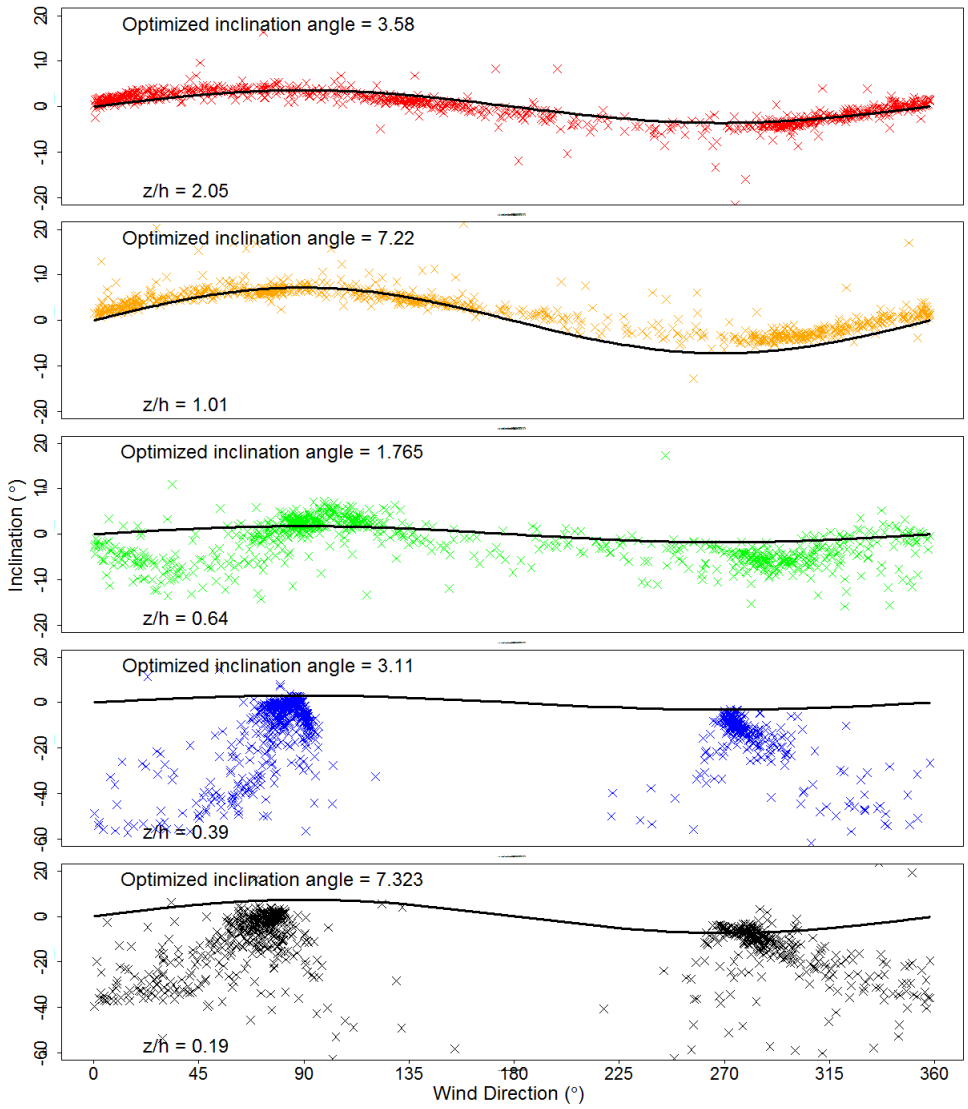

Figure A1: Inclination angles with varying wind direction with height.

The mean absolute error (MAE) in the case study fluxes associated with an error of $\pm 1^\circ$ in the slope angle rotation are are given by Table A1. MAE is calculated using Equation 5.

$$MAE = \frac{1}{n} \sum_{n=1}^{n} |y_i - x_i| \tag{A1}$$

where y_i is the predicted value - or that when a slope angle of 7° is used in the rotation, and x_i is the observed - or that when either a slope angle of 6° or 8° is used, and n is the number of samples. In this way, the MAE is representing the potential amount of flux that is incorrect in our reported values.

z/h	**uw**	**vw**	**wT**
2.06	0.0013	0.0008	0.0017
1.02	0.0008	0.0004	0.0011
0.647	0.0004	0.0002	0.0005
0.391	0.0003	0.0001	0.0003
0.195	0.0002	0.0001	0.0003

Table A1: Mean absolute error (MAE) for vertical momentum and heat fluxes associated with $\pm 1^\circ$ slope angle measurement errors. MAE is calculated from 211 5-minute case study time series.

z/h	6°			8°		
	uw	vw	uv	uw	vw	uv
2.06	0.42 %	0.06 %	0 %	0.4 %	0.04 %	0 %
1.02	0.12	0.76	0	0.12	0.75	0
0.647	0.34	0.08	0	0.33	0.07	0
0.391	0.58	0.11	0	0.58	0.1	0
0.195	0.88	0.36	0	0.84	0.32	0

Table A2: Percent contribution of fluxes (potentially) affected by over or under rotation (6° or 8°, respectively) to the total calculated flux.

The change in magnitude and the fact that there are incidences of a change in sign of the momentum fluxes based upon a difference of 1° in the measured slope angle affects the quadrant, and associated, analyses. Given, however, that when the slope angle uncertainty implicates a change in the sign of the momentum fluxes, the flux itself is very small (on the order of at most 0.5% of the mean flux), the use of a hyperbolic hole in all quadrant and associated analyses for momentum circumvents the issue of potential uncertainty induced momentum flux sign changes. As small fluxes will already be minimally represented in statistical first moments, such as the mean, they are not excluded. Figure A2 provides an analysis on where the majority of the instantaneous flux associated with a potential change in sign with slope angle uncertainty is contained. The figure shows that for increasing hole size, the amount of flux contributed by the potentially erroneous

flux decreases. It is of note that the y-axis gives the number of instances that the flux exceeds the hole size, and therefore, $H = 0$ in the plot provides the total number of potentially erroneous flux instances. Evidently, the use of a hole size, $H = 3$ for the vertical stresses and a hole size of $H = 1$ for the horizontal stresses sufficiently avoids the potential changes in sign being associated with the octant and quadrant analyses for momentum.

For the $u'w'$, the hole size is larger at $z/h_c = 0.64$ because the mean flux at this location is very small; the same issue occurs at $z/h_c = 1.02$ for the $v'w'$ flux. Despite this, the reported hole size of 3 for the vertical fluxes is still used - even at this hole size, a large amount of the possible flux error is avoided.

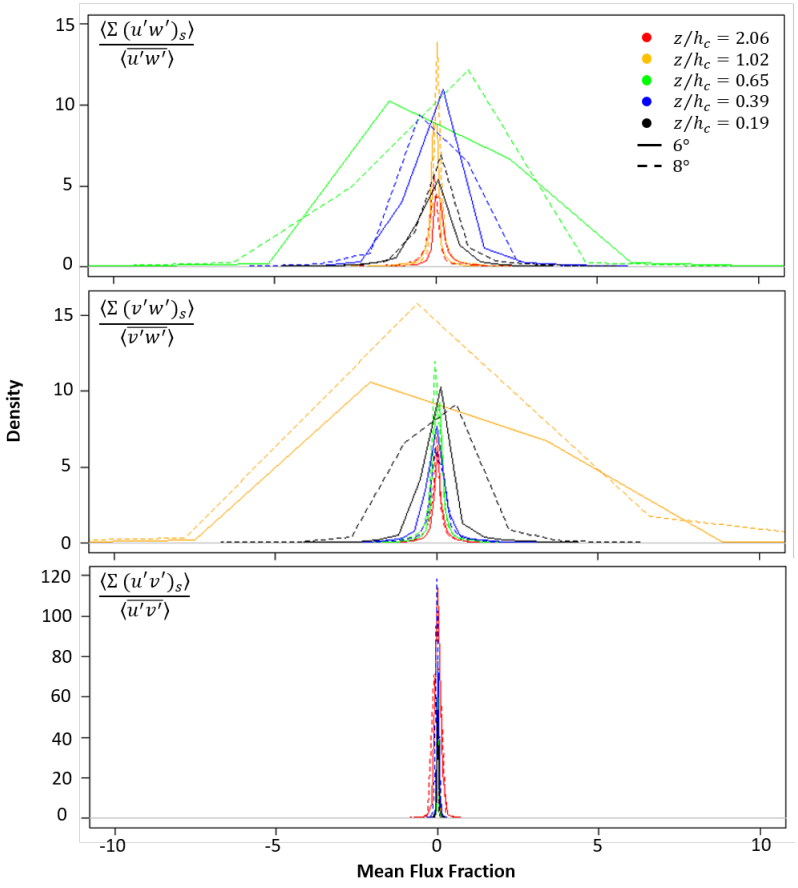

Figure A2: Density plot of contribution of flux associated with a sign change to the total flux. solid lines represents the contribution associated with an over rotation, and dashed lines represent the contribution associated with an under rotation. When the lines reach zero, there is no longer any contribution of the flux to the mean.

On average, correlations in any octant at or larger than $H = 3$ occur around 50% of the time, while those for $H = 1$ occur around 70% of the time (Table A3)

Hole Size	z/h_c				
	0.19	0.39	0.65	1.02	2.06
3	55.5%	56.1%	51.9%	27.4%	43.3%
1	77.3%	77.7%	75.0%	55.3%	69.2%

Table A3: Percentage of time that the flux is above the threshold hole size of 3 or 1

Appendix B: Thermocouple Corrections - Sample Calculation

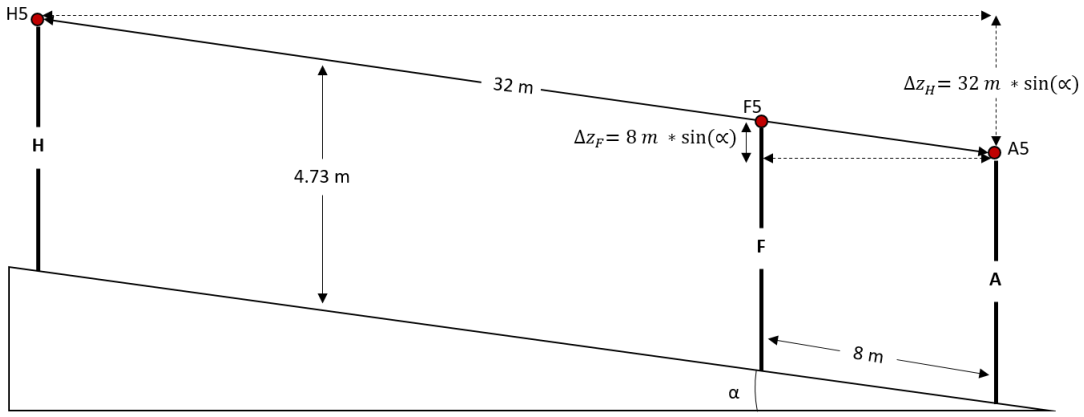

Figure A3: Sketch of problem set-up and variables used in example calculation of the temperature corrections for Mast F.

First, the background stratification is calculated using the average 5-minute temperature at $z = 4.73\ m$ for Masts A (at tower) and H (32 m up-slope):

$$\Gamma_{ref} = \frac{\overline{T_{H5}} - \overline{T_{A5}}}{\Delta z_H} \tag{A2}$$

Next, the correction to be applied to the averages of the TC on Mast F (8 m up-slope) is calculated:

$$T_{F,correct} = \overline{T_{F5}} - (\overline{T_{A5}} - \Gamma_{ref} * 8 * sin(\alpha)) \tag{A3}$$

The corrected mean temperature at the top of the Mast F array is only a function of the 5-minute calculated background stratification and the vertical distance, Δz_F

$$T_{F5,new} = \overline{T_{A5}} - \Gamma_{ref} * 8 * sin(\alpha) \tag{A4}$$

While the mean temperatures are the other 4 locations below the top TC are calculated by removing the correction, $T_{F,correct}$ from their respective time series:

$$T_{Fj,new} = T_{F4} - T_{F,correct} \tag{A5}$$

where j here represents indices $1 - 4$ (TC measurements at heights 0.45, 0.9, 1.49, and 2.34 m, respective).